HIGH-OPERATING-TEMPERATURE (HOT) INFRARED DETECTORS BASED ON ANTIMONIDE HETEROSTRUCTURES

Melih KORKMAZ

PhD Dissertation

Department of Physics

Supervisor: Prof. Dr. Uğur SERİNCAN

Eskişehir

Eskişehir Technical University

Institute of Graduate Programs

June 2022

This thesis has been supported by Eskişehir Technical University Scientific Research Projects under the project BAP-1706F388.

FINAL APPROVAL FOR THESIS

This thesis titled HIGH-OPERATING-TEMPERATURE (HOT) INFRARED DETECTORS BASED ON ANTIMONIDE HETEROSTRUCTURES has been prepared and submitted by Melih KORKMAZ in partial fulfillment of the requirements in "Eskişehir Technical University Directive on Graduate Education and Examination" for the Degree of PhD in Physics Department has been examined and approved on 15/06/2022.

Committee Members		**Title, Name and Surname**	**Signature**
Member	:	Assoc. Prof. Dr. Mustafa KULAKCI	
Member	:	Assoc. Prof. Dr. Erhan AYAS	
Member	:	Assoc. Prof. Dr. Serdar KOCAMAN	
Member	:	Assoc. Prof. Dr. Tunay TANSEL	
Member	:	Assoc. Prof. Dr. Tahir ÇOLAKOĞLU	

Prof. Dr. Murat TANIŞLI

Director of the Institute of Graduate Programs

15/06/2022

SUPERVISOR APPROVAL

PhD student Melih KORKMAZ, whom I supervise, has completed this thesis titled HIGH-OPERATING-TEMPERATURE (HOT) INFRARED DETECTORS BASED ON ANTIMONIDE HETEROSTRUCTURES. According to my inspections, the work is scientifically and ethically appropriate for the student to the thesis defense exam.

Supervisor

Prof. Dr. Uğur SERİNCAN

ABSTRACT

HIGH-OPERATING-TEMPERATURE (HOT) INFRARED DETECTORS BASED ON ANTIMONIDE HETEROSTRUCTURES

Melih KORKMAZ

Department of Physics

Eskişehir Technical University, Institute of Graduate Programs, June 2022

Supervisor: Prof. Dr. Uğur SERİNCAN

In this study, InAs/InAsSb based p-i-n and nBn detector structures were designed for mid-infrared region detection. The designed detector structures were grown on GaSb substrates by molecular beam epitaxy technique. By changing parameters such as growth rate, flux modulation and substrate vendor, crystal quality of the grown structures were monitored. The dark current and spectral responses of the detectors were evaluated by fabricating single pixel devices. In addition, recombination mechanisms and localized states in the absorber and barrier layers were investigated using the photoluminescence technique and the results of the experimental studies were presented.

With the radiometric approach, parameters affecting system performance such as well fill, dynamic range and bit losses were investigated for an InAs/InAsSb based imager at different scene temperatures. Detector parameters such as quantum efficiency, noise equivalent temperature differences and pixel non-uniformity were considered in the analysis.

Keywords: InAs/InAsSb superlattice, Molecular beam epitaxy, Infrared detectors.

ÖZET

ANTİMONİ ÇOKLUYAPI TABANLI YÜKSEK SICAKLIKTA ÇALIŞAN (HOT) KIZILÖTESİ DEDEKTÖRLER

Melih KORKMAZ

Fizik Anabilim Dalı

Eskişehir Teknik Üniversitesi, Lisansüstü Eğitim Enstitüsü, Haziran 2022

Danışman: Prof. Dr. Uğur SERİNCAN

Bu çalışmada, orta kızılötesi bölgesinde algılama yapmak amacıyla InAs/InAsSb süperörgü malzeme sisteminin kullanıldığı p-i-n ve nBn dedektör yapıları tasarlandı. Tasarlanan dedektör yapıları moleküler demet epitaksi tekniğiyle GaSb alttaş üzerine büyütüldü. Büyütme oranı, alttaş, akı modülasyonu gibi parametreler değiştirilerek kristal kalitesine olan etkileri incelendi. Üretilen dedektör yapılarının tek piksel aygıt fabrikasyonu yapılarak, karanlık akım ve spektral tepkileri incelendi. Ayrıca fotolüminesans tekniği kullanılarak soğurucu ve bariyer katmanlarındaki rekombinasyon mekanizmaları ve lokalize durumlar araştırıldı ve deneysel çalışmaların sonuçları sunulmuştur.

Radyometrik yaklaşım ile farklı sahne sıcaklığında bir InAs/InAsSb dedektör için kuyu doluluk miktarı, dinamik aralık ve bit kayıpları gibi performansa etki eden parametreler incelenmiştir. Yapılan analizlerde dedektöre ait kuantum verimi, gürültüye eşdeğer sıcaklık farkı ve piksel homojensizliği hesaplamalarda göz önünde bulundurulmuştur.

Anahtar Sözcükler: InAs/InAsSb süperörgü, Moleküler demet epitaksi, Kızılötesi dedektör.

ACKNOWLEDGEMENTS

First, I would like to thank my supervisor, Prof. Dr. Uğur Serincan, for his continuous support, guidance and providing me rich and independent research environment throughout my graduate study. I am grateful to be a member of the Nanoboyut Research Laboratory that allowed me to enter the world of infrared detector.

I would also thank to Assoc. Prof. Mustafa Kulakcı for his guidance, sharing his laboratory experiences, unique suggestions (There is power in simplicity!) and jokes.

I would like to thank Assoc. Prof. Bülent Aslan for his assistance and guidance in the early stages of my graduate study. I would also thank to him for sharing his very valuable experiences about infrared detector field.

I would like to my thesis committee members, Assoc. Prof. Serdar Kocaman, Assoc. Prof. Tunay Tansel, Assoc. Prof. Erhan Ayas and Assoc. Prof. Tahir Çolakoğlu for their suggestions.

I would like to thank Dr. Oray Orkun Cellek for him for sharing his experience in mid-infrared photoluminescence measurements. I would also thank to Muhammed Talha Korkmaz for his help during the radiometric calculations.

Special thanks to all the my Nanoboyut teammates, Burcu Arpapay, Bülent Arıkan, Güven Korkmaz, Hülya Kuru Mutlu, Hülya Atmacan, Ayşe Şevik, Samet Özdemir, Mehmet Erkuş, Eren Suyolcu, Seval Şahin, Berker Hüsam, Onur Şenel, Hazal Zaimler, Erdem Yıldırım, Ali Büyükpınar, Muhammed Aktaş, Ozan Korkan who gave the opportunity to collect many beautiful and missed memories over the past 10 years.

Finally, I would like to thank my father Hüseyin Korkmaz, my mother Necla Korkmaz, my brother Semih Korkmaz and my wife Seda Yıldız Korkmaz for their endless support, encouragement and love..

Melih KORKMAZ

15/06/2022

STATEMENT OF COMPLIANCE WITH ETHICAL PRINCIPLES AND RULES

I hereby truthfully declare that this thesis is an original work prepared by me; that I have behaved in accordance with the scientific ethical principles and rules throughout the stages of preparation, data collection, analysis and presentation of my work; that I have cited the sources of all the data and information that could be obtained within the scope of this study, and included these sources in the references section; and that this study has been scanned for plagiarism with "scientific plagiarism detection program" used by Eskişehir Technical University, and that "it does not have any plagiarism" whatsoever. I also declare that, if a case contrary to my declaration is detected in my work at any time, I hereby express my consent to all the ethical and legal consequences that are involved.

Melih KORKMAZ

CONTENTS

Page

APPENDIX

CURRICULUM VITAE

LIST OF TABLES

Page

LIST OF FIGURES

LIST OF IMAGES

Page

GLOSSARY OF SYMBOLS AND ABBREVIATIONS

As	:	Arsenic
AlSb	:	Aluminum Antimonide
BLIP	:	Background Limited Performance
DlaTGS	:	Deuterated L-alanine doped triglycene sulphate
eV	:	Electron Volt
FPA	:	Focal Plane Array
Ga	:	Gallium
GaAs	:	Gallium Arsenide
GaInSb	:	Gallium Indium Antimonide
GaSb	:	Gallium Antimonide
Ge	:	Germanium
HCl	:	Hydrochloric Acid
HDS	:	Heterostructure Design Studio
Hg	:	Mercury
Hz	:	Hertz
HgCdTe	:	Mercury Cadmium Telluride
HR-XRD	:	High Resolution X-Ray Diffraction
HOT	:	High Operating Temperature
In	:	Indium
InAs	:	Indium Arsenide
InGaAs	:	Indium Gallium Arsenide
InAsSb	:	Indium Arsenide Antimonide
K	:	Kelvin
LWIR	:	Long Wavelength Infrared
MBE	:	Molecular Beam Epitaxy
mK	:	milli Kelvin
ML	:	Mono Layer
MWIR	:	Mid Wavelength Infrared
MCT	:	Mercury Cadmium Telluride
NETD	:	Noise Equivalent Temperature Difference

P	:	Phosphorus
PC	:	Photoconductive
PbS	:	Lead Sulfide
PbSe	:	Lead Selenide
PL	:	Photoluminescence
ROIC	:	Read-out Integrated Circuit
Sb	:	Antimonide
SEM	:	Scanning Electron Microscope
Si	:	Silicon
SRH	:	Shockley-Read-Hall
SL	:	Superlattice
T2SL	:	Type II Superlattice
VLWIR	:	Very Long Wavelength Infrared
XRD	:	X-Ray Diffraction
ZnSe	:	Zinc Selenide
Å	:	Angstrom
Ω	:	Ohm
°C	:	Celsius
µm	:	Micrometer
$\lambda_{cut\text{-}on}$	:	Cut-on wavelength
$\lambda_{cut\text{-}off}$	:	Cut-off wavelength

1. INTRODUCTION

1.1. The Motivation

III-V group semiconductor infrared photodetectors are high performance detectors that can detect at multiband/multicolor and can generally be operated at high speeds. Since they often operate at liquid nitrogen temperatures, the required cooling system increases both the cost and the physical size of the existing imaging systems. This, therefore, increases the power consumption and added an extra volume to the platform to be used. The development of small size detecting system is possible by the production of infrared detectors operating at high temperatures. This can be achieved by designs having low dark current at elevated temperatures.

In the past 15 years, studies on type II superlattice (T2SL) material system showed that it is a strong candidate for the third-generation infrared photodetector technology. High operating temperature (HOT) ability of this material system had not been showed until barrier infrared detector design was proposed by Maimon and Wicks [1]. This kind of structures block the diffusion of the majority carriers from the contact layers and significantly decreased the dark current level compared with the standard pin diode. Barrier structure with n-type absorber can also be used to suppress surface leakage dark current (lack of passivation processes) [1]. Many groups have been demonstrated their novel barrier detector architecture such as nBn [2], XBn [3], pMp [4] and CBIRD [5] to aim of improving the signal/noise ratio and operating at high temperatures.

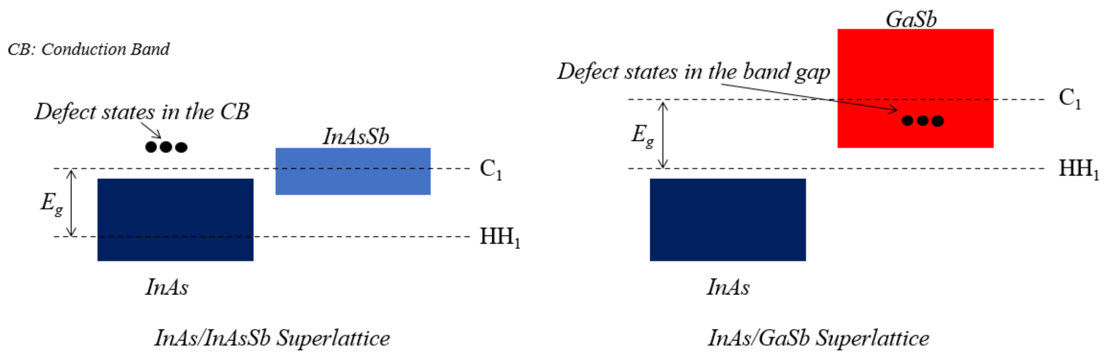

Figure 1.1. *Defect states in InAs/InAsSb superlattice and InAs/GaSb superlattice material [http-1].*

In spite of their ability to operate at high temperatures [6], multi-color operation [7-8], InAs/GaSb T2SL structures have not reached their ultimate potential [9]. As shown in Figure 1.1, native defects (especially in the GaSb layers [http-1]) in the superlattice period acts as recombination centers in the band gap and increase the intrinsic carrier concentration which are responsible for the limited minority carrier lifetimes (~40-100 ns) and diffusion lengths in SL materials [10,11]. In order to overcome these problems, many research groups have been tried to find a solution by using Ga-free material system such as InAsSb and InAs/InAsSb.

For nearly 40 years, $InAs/InAs_{1-x}Sb_x$ superlattices system has been considered as an alternative for the III-V based infrared detectors [12-19]. Carrier lifetime studies on this material system has been shown that Ga-free material systems have longer minority carrier lifetime than that of Ga-based superlattices' [20,21]. This enhancement can improve electrical performance of infrared detectors with diffusion-limited dark current. Considering that the HOT infrared detectors are limited by diffusion dark current, InAs/InAsSb materials system may be solution for the higher BLIP temperature. In order to increase the signal/noise ratio of the detector at high temperatures, absorption coefficient of the active layer material and diffusion length of the photo carriers must also be high. Preliminary theoretical studies on the absorption coefficient and diffusion length [22] of the Ga-free based material system have not been pessimistic. It has weaker absorption coefficient than that of Ga-based superlattice's and most importantly the low hole mobility in the growth direction would result in short diffusion length. These drawbacks would lead to reduced collection of the photo-carriers and also decreased quantum efficiency. However, latest published works on Ga-free based barrier structures have shown that this material system may have high quantum efficiency under LWIR [17] and MWIR/LWIR [18] dual band operation. Ting et all showed that under the certain conditions, hole conductivity effective masses along the growth direction can be smaller than the band-edge effective masses and large LWIR superlattice hole splittings that can lead to reduced scattering [23]. Therefore, above-mentioned two events offer to reach high quantum efficiency at LWIR region, in contrast to theoretical expectations.

1.2. The Outline

In this thesis it is aimed to grow and develop InAs/InAsSb T2SL based barrier infrared detectors for high operating temperature at mid infrared region. Within the scope of the thesis, detector design, epitaxial material growth, device fabrication and electro-optical characterizations were performed. In addition, the performance of an InAs/InAsSb T2SL based imaging system was evaluated using a radiometric approach.

In Chapter 1, a brief information about superlattice infrared detectors is given. In the next section, different detector technologies are explained and the development process of the T2SL detectors is summarized with examples. In Chapter 3, the experimental methods used in the thesis are mentioned. In Chapter 4, p-i-n and nBn detector structures are designed and characterization studies of the preliminary material growth for p-i-n diode are examined. In Chapter 5, material growth and characterization results of nBn detectors are shared. In Chapter 6, performance of the InAs/InAsSb superlattice based nBn MWIR infrared detector has been investigated by radiometric and electronic modeling in a near-realistic infrared imaging system. Finally, Chapter 7 presents the concluding remarks and future works.

2. SUPERLATTICE BASED INFRARED DETECTOR TECHNOLOGY

2.1. Infrared Detectors

An infrared detector is a device that reacts and detects infrared radiation. Infrared detectors are used in daily life in fields such as automotive, spectroscopy and medicine, as well as in astronomical observations and military applications where high technologies are used (Image 2.1). Since performance of the infrared imaging systems has critical role in efforts to gain superiority in the field of battlefield, defense applications have played a significant role in the development of infrared detectors. On the other hand, progress in advanced material fabrication techniques have allowed production of high-performance infrared detector with small sized and large pixel formatted and low power consumption.

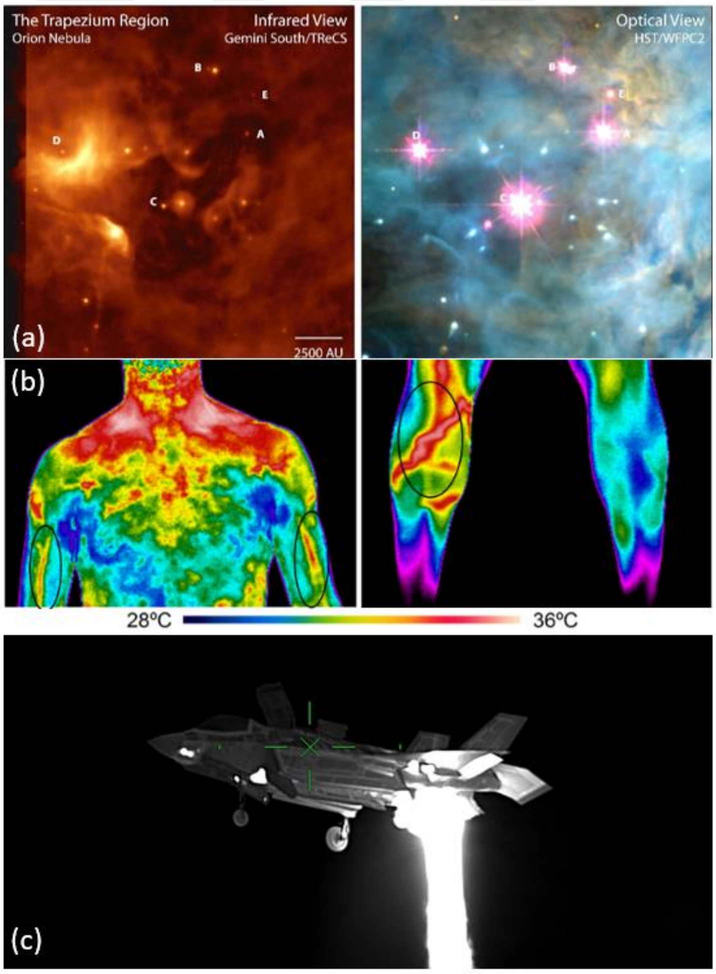

Image 2.1. *Applications of infrared imaging systems: (a) astronomical observations [24] (b) medical thermography [25], and (c) detection and tracking of the military targets [http-2].*

Depend on the detection mechanism, infrared detectors could be divided into two main categories as thermal detectors and photon detectors.

2.1.1. Thermal Detectors

The thermal detectors respond to absorbed infrared radiation by changing the temperature of the detector element. This temperature change causes measurable physical properties change such as resistance, voltage, capacitor, mechanical displacement etc. [26]. Golay cells (*mechanical displacement*), bolometers (*resistance*) and pyroelectric (*capacitor)* detectors and thermopiles (*voltage*) can be given as example of thermal detectors.

The early days of the thermal detectors were unusable for the imaging system. But with the development of microfabrication technique, thermal detectors (e.g. a-Si, VO_x microbolometers) can be produced as mass production with large image formats (1280×1024) and small pixel pitches (12 -17 µm, [27]). The fact that microbolometers can work without cryogenic cooling and have a low noise equivalent temperature difference (NETD) value (<30 mK, [http-3]) are the main reasons for their preference in terms of cost and performance. Image 2.2. is an example showing the technological level of today's uncooled thermal detectors.

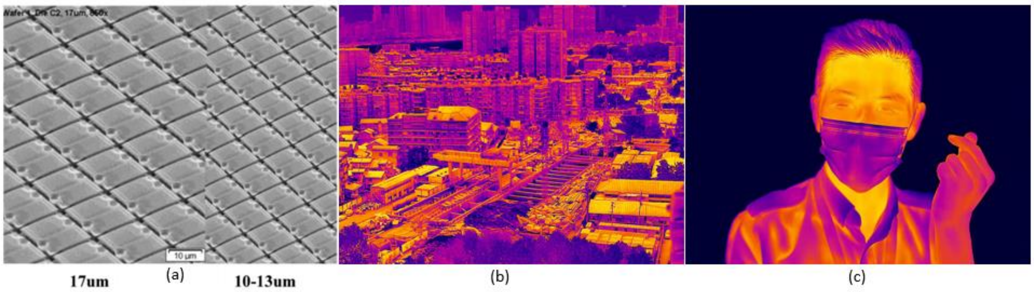

Image 2.2. *(a) Microbolometer structure with reduced pixel sizes [27] and (b), (c) images were taken from the 1280×1024-12 µm pixel size uncooled VO_x microbolometer infrared detector with < 30 mK [http-2].*

2.1.2. Photon Detectors

The photon detectors are based on semiconductor materials which absorb photons and generates photocarriers. The semiconductor material has energy gap which corresponds to forbidden energy difference between the valence band and the conduction band. If a photon has enough energy to excite a carrier at an energy state or energy band to the conduction band, the photon is absorbed and can be detected. However, if the photon has no energy to promote, the photon passes through the material. Since the photon absorption mechanism does not need to heat the entire detector element, photon detectors respond in a short time than the thermal detectors. So, photon detectors are preferred in applications where high-speed detection and imaging is required.

The photon detectors are divided into two groups: photoconductors and photovoltaics.

2.1.2.1. Photoconductive Detectors

The photoconductive (PC) detector responds to photons by changing the resistance or conductance [26] of the semiconductor. As shown in Figure 2.1, the photoexcitation occurs at band to band transitions (intrinsic, PbS, PbSe, HgCdTe) or between the impurity energy levels in the energy gap (extrinsic, Ge:Hg, Ge:In, Si:As, Si:P) [28]. The cut-off wavelength (λ_c) of the intrinsic PC is equal to the band gap of the semiconductor material. By applying the impurity doping process to the host material, it is possible to detect lower wavelengths as well (Si:P (λ_c = 29 μm), Ge:In (λ_c = 120 μm)) [26].

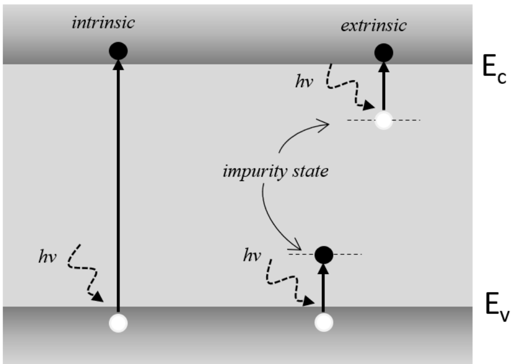

Figure 2.1. *Photoexcitation process via band to band (intrinsic) and between the impurity state and band (extrinsic) [28].*

When the incident radiation falls on the detector (Φ_q), photocarriers (electrons and holes) are generated and they swept-out to the contact layers by applying the external bias (V_B). For PC detectors, biasing circuit must be utilized to measure the magnitude of the output signal (V_o) (Figure 2.2) [26].

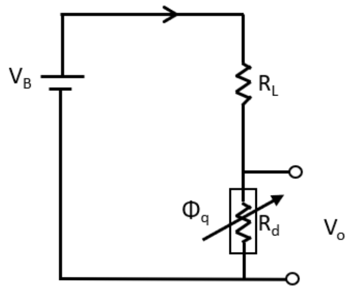

Figure 2.2. *Photoconductor biasing circuit: V_o : Output voltage, RL: load resistor, V_B: DC bias voltage and Φq: the photon flux incident on the PC detector. [26].*

2.1.2.2. Photovoltaic Detectors

Basically, photovoltaic detectors are made by continuous crystalline semiconductor with a p-type and a n-type regions. The photon generates electron and hole pair at the junction of the p-n materials and then they are swept out to the contact layers by internal electric-field. This structure, called the photodiode, produces voltage or current at the end of the photon absorption process (Figure 2.3). By inserting undoped (*i*) or low doped (π) regions in the junction (as in p-i-n diode structure), the amount of the output signal can be increased. Depend on the device design requirements, photodetectors could be as a form of p-on-n or n-on-p, mesa or planar structure and also bulk material or heterostructure (such as superlattice).

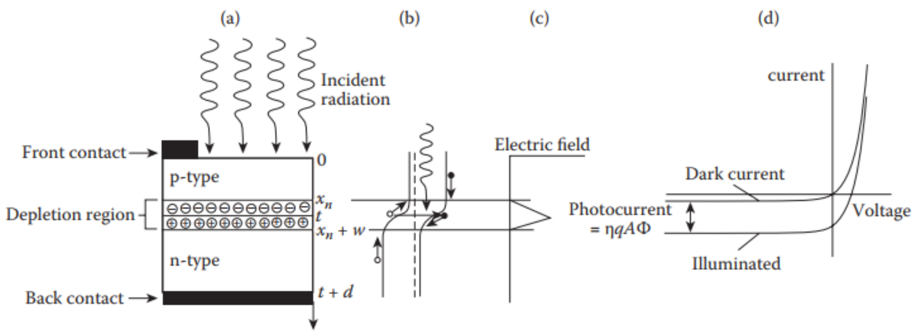

Figure 2.3. *(a) p-n junction structure, (b) band alignment, (c) electric-field distribution and (d) current-voltage characteristics of the diode under illuminated and dark condition [29].*

The Si, GaAs, Ge, InSb, InAsSb, InGaAs, HgCdTe semiconductor compounds can be given as an example of photodiode materials and their energy gaps are listed in Table 2.1. The band gap of the material depends on the temperature and its composition.

The pressure, temperature, electric-field and magnetic-field affect the band gap of the semiconductor structure [30].

Table 2.1. *Example of photovoltaic detector materials and their band gap energies at T=300 K.*

Material	Energy Band Gap (eV)
Si	1.12
GaAs	1.43
Ge	0.66
InSb	0.17
$InAs_{1-x}Sb_x$	$0.417 - 1.28\times10^{-4}T - 2.6\times10^{-7}T^2 - x(0.902 + 10^{-9}T^2) + 0.72x^2$
$Hg_{1-x}Cd_xTe$	$-0.302 + 1.93x - 0.81x^2 + 0.832x^3 + 5.35\times10^{-4}(1 - 2x)T$

2.2. Brief History of Type II Superlattice Detectors

A superlattice is a periodic structure that individual layer thicknesses are several nanometers. In a few nanometers thick superlattice structure, electron and hole wavefunctions overlap between the adjacent thin layers and form the conduction and valence miniband, respectively. The difference between conduction miniband and valence miniband corresponds to the band gap of the superlattice (Figure 2.4).

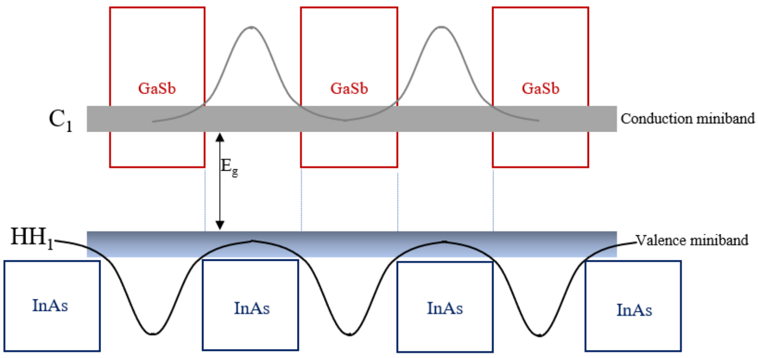

Figure 2.4. *Miniband structure created by the type II InAs/GaSb superlattice wave-functions.*

With the development of the crystal growth techniques such as molecular beam epitaxy (MBE, in 1960s) where material thickness can be controlled at a few monolayers, it has become possible to grow of superlattice structures. Both theoretical and experimental studies on III-V superlattice semiconductors were started at the 1970s [31-

33] and Leo Esaki's valuable studies on superlattices at that time formed the basis of the today's antimonide based superlattice structures.

The first infrared detector proposal was made by Smith and Mailhiot using the type-II InAs/GaInSb superlattice structure in 1987 [34]. They suggested that it would be possible to design a detector which was capable of sensing in the 4-25 µm infrared region, simply by changing the individual layer thicknesses and the ternary alloy composition. Also, it was emphasized that InAs/GaInSb superlattice material system is superior electrical properties due to much larger electron effective mass than that of the HgCdTe material system (for the 10 µm detection). Their study showed that the electron effective mass of the superlattice system was large enough to reduce tunneling currents and also small enough to give good electron mobilities and diffusion length for the high performance photodetection [34].

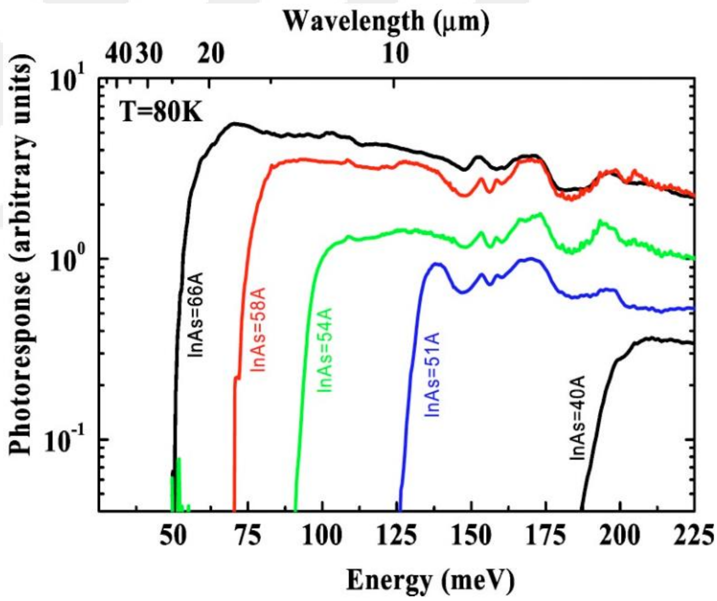

Figure 2.5. *Photoresponse spectrum: Effect of the change in InAs layer thickness for a fixed GaSb layer thickness (40 Å) [36].*

In the late 1990s, thanks to the production of the commercially available GaSb substrates, Sb-based Type-II superlattice materials began to be grown lattice matched to the GaSb substrates [35]. The GaSb substrates paved the way for the production of infrared detectors with fewer crystallographic defects and high performance. Considering the potential of the superlattice detectors to operate in a wide infrared spectrum range (Figure 2.5, [36]), studies on this material system were increased in many national research laboratories (Hughes Research Lab., Naval Research Lab., Los Alamos National Lab., Air Force Research Lab., Jet Propulsion Lab., Fraunhofer-Institute) and universities (Univ. of Illinois, Northwestern Univ., Univ. of New Mexico, Montpellier Univ. etc.). The superlattice detectors with p-i-n diode were experimentally shown to work in MWIR [37], LWIR [38] and VLWIR [39] regions. In 2004, a high performance InAs/GaInSb superlattice focal plane array (FPA) with 5.3 μm cutoff was demonstrated in Germany (AIM, Fraunhofer Institute) (Image 2.3, [40]).

Image 2.3. *An image belongs to 256x256 pixel format SL FPA (NETD: ~11 mK, F/2) [40].*

In 2006, researchers from the University of Rochester suggested a new detector structure named as nBn [1]. As shown in Figure 2.6 (a), a typical nBn detector structure consists of high band gap barrier layer, absorber and top/ bottom contact layers. The barrier layer blocks the majority carriers and allows the flow of the minority carriers to the contact layers. The most important contribution of the barrier is the suppression of the Shockley-Read-Hall (SRH) mechanism in the absorber layer by attracting most of the electric field in the structure with its large band gap. Since the SRH dark current is suppressed, the total dark current is lower than that of the p-n diode (Figure 2.6 (b)). This makes the nBn detector to have higher sensitivity compared to the p-n diode at the same operation temperature. In addition, its low dark current allows it to operate at higher temperatures (Figure 2.6 (b)).

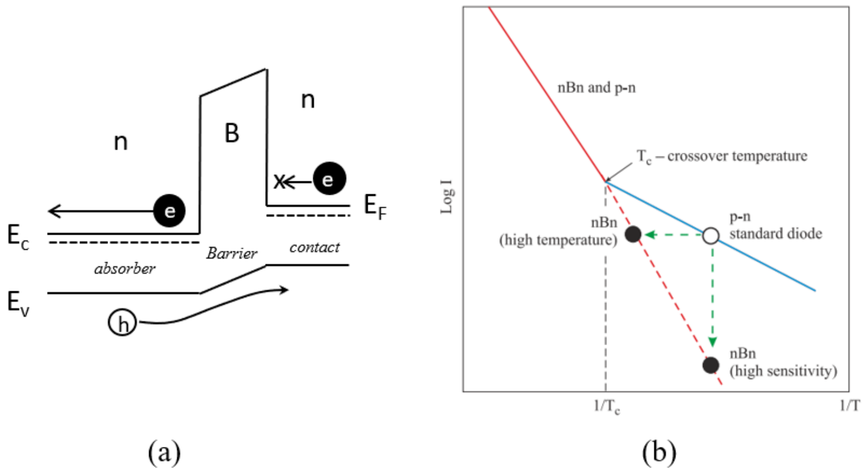

Figure 2.6. *(a) Typical band alignment of nBn detector structure (b) comparison of the dark current in p-n diode and in nBn detector [41].*

Although the nBn detector design was first proposed for the InAs and InAsSb bulk materials [1], it inspired many research teams to design new detector structures called barrier infrared detectors (BIRD). By using the successfully band-gap engineering with the 6.1 Å family (InAs, GaSb, AlSb) materials, new superlattice barrier layers (e.g. InAs/AlSb superlattice as a hole barrier, GaSb/AlSb as an electron barrier) compatible with the InAs/GaSb superlattice absorber layers were designed such as CBIRD [5], pMp [6], pBiBn [42], XBn[3] structures. The performance of the barrier infrared detectors at high operating temperatures has approached the values of MCT detectors. As shown in Figure 2.7, barrier detector performs close to the R_0A value of the MCT at high temperatures (>150 K) [43]. Thanks to the higher operating temperatures compared to the p-i-n diodes, the cooling need of the infrared detectors reduced. This paved the way for the production of cooled infrared detectors that are smaller in size, lighter and consumes less power.

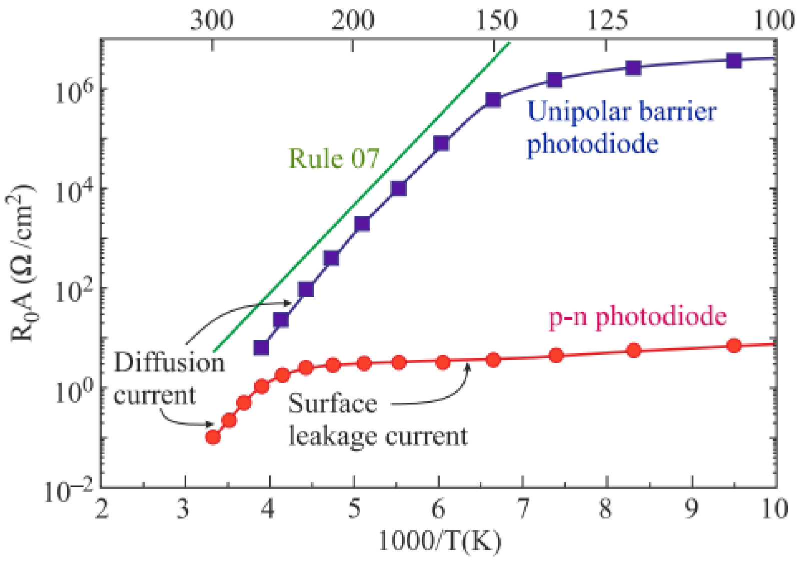

Figure 2.7. *Comparison of the R_0A value of the standard InAs p-n diode and barrier diode. Rule 07 line shows the temperature dependent R_0A value of the MCT detector at the same wavelength [43].*

The pMp detector structure designed by Center for Quantum Devices is one of the detectors that can be given as an example of HOT detectors operating in the MWIR region (Image 2.4). BLIP temperature and specific detectivity of the detector was 150 K and 1.5×10^{14} Jones (77 K), respectively [6].

Image 2.4. *Images from the pMp HOT MWIR detector at different operating temperatures[6].*

HRL Laboratories developed dual band superlattice based FPAs under the VISTA program (Image 2.5). NETD values for MWIR and LWIR bands were measured as 27.44 and 27.62 mK, respectively. HD-format (1280×720, 12 µm pixel pitch) detector was tested over 2000 thermal cycles and no degradation in the pixel operability and NETD values were observed [44]. This study is of great importance in terms of seeing that it is technologically possible to produce superlattice detectors in high pixel format with dual band operation.

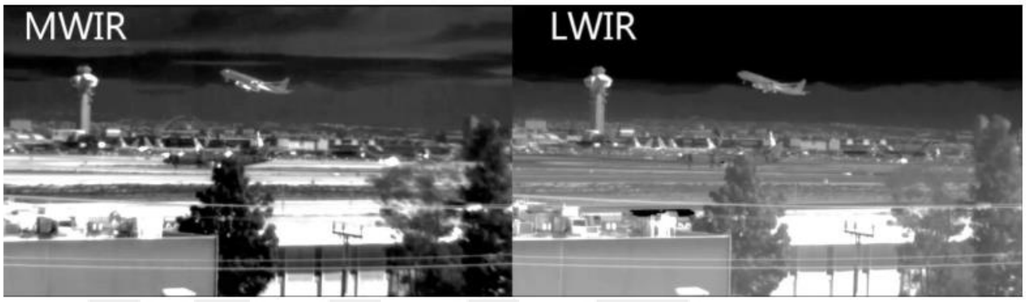

Image 2.5. *1280 × 720, 12 µm pixel pitch dual band superlattice FPA images [44].*

Image 2.6 shows the images (at 150 K) taken from the 1k × 2k, 5 µm pixel pitch MWIR detector developed by HRL Laboratories. Pixel operability and quantum efficiency (without anti-reflection coating) was higher than 99.9 % and 60%, respectively [45].

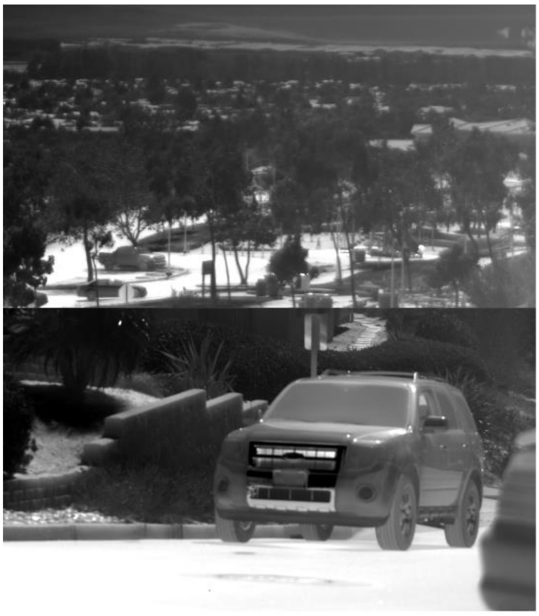

Image 2.6. *An image obtained at 150 K with 1k × 2k, 5 µm pixel pitch FPA [45].*

In spite of the InAs/GaSb T2SL detectors operates at high temperatures, this material system suffers from the native defects acting as recombination centers, especially in the GaSb layers. Native defects in superlattices increase the residual background carrier concentration and reduce minority carrier lifetimes to levels of 40-100 ns [10-11]. This is one the of the main obstacles for improving high temperature operating performance. In order to improve the electrical performance of barrier infrared detectors, it is necessary to reduce diffusion dark currents with higher minority carrier lifetime (τ). The diffusion dark current (hole diffusion from the n type absorber) due to minority carrier generated by the Auger 1 mechanism can be defined as

$$J_0 = q\frac{n_i^2}{N_D}\frac{d}{\tau} \tag{2.1}$$

where q is an electron charge, n_i is the intrinsic carrier density, N_D is the donor density, d is the absorber thickness and τ is the minority carrier lifetime [46]. InAs/InAsSb superlattice material system has attracted attention as an alternative for the InAs/GaSb material system due to its longer minority carrier lifetime. In time resolved PL experiments, minority carrier lifetimes of the MWIR and LWIR superlattices were measured to be ~10 µs [47] and 400 ns [48], respectively. The carrier lifetime obtained for the MWIR superlattice was close to the that of the MCT materials. This improvement has increased the studies on the barrier detector with InAs/InAsSb materials, especially in the MWIR region. Table 2.2 shows the performance results of the InAs/InAsSb based infrared detectors published in the literature.

Table 2.2. *Electro-optical performance results of the InAs/InAsSb superlattice detectors.*

Structure	λ_c [µm]	QE (%)	J_{dark} (A/cm^2)	D* ($cmHz^{0.5}/W$)	Ref.
nBn	10	54 (7.9µm)	4.4×10^{-4} (77 K)	2.8×10^{11}	[17]
nBn	5.1 9.5	45 (4µm) 40 (7µm)	1×10^{-7} (77 K) 5.7×10^{-4} (77 K)	8.2×10^{12} 1.64×10^{11}	[18]
nBn	5.37	52 (4.5 µm)	4.5×10^{-5}(150 K)	3.10^{11}(150 K)	[49]
pBn	4.4	47	1.16×10^{-5}(150 K)	$7.11x10^{11}$ (150 K)	[50]
nBn	4.8	35	1×10^{-10}(100 K) 5×10^{-6}(150 K)	-	[51]
nBn	4.8	60 (4.4 µm)	2×10^{-7}(130 K)	-	[52]

Image 2.7 is taken from the InAs/InAsSb based HOT superlattice detector developed by the Jet Propulsion Laboratory [49]. NETD values for 160 K and 170 K were measured as 18.7 and 26.6 mK, respectively. The pixel operability is 99.7% (99.6%) at 160 K (170 K). At 150 K, the quantum efficiency is ~52% (at 4.5 µm) and 4.5×10^{-5} A/cm^2.

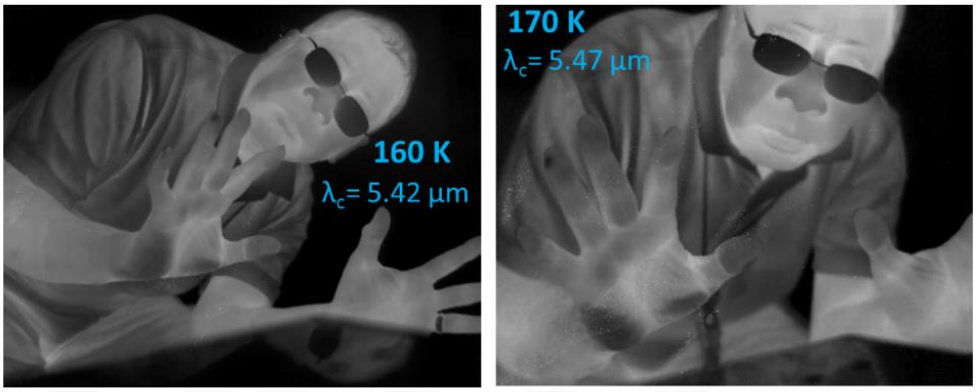

Image 2.7. *The image was taken from the MWIR InAs/InAsSb FPA (640×512, 24µm) [49].*

3. EXPERIMENTAL METHODS

In this chapter, experimental methods used in the production and characterization of detector structures grown within the scope of the thesis are explained.

3.1. Epitaxial Material Growth

The molecular beam epitaxy (MBE) is a material production technique that allows controlled crystal growth at the atomic level under high vacuum condition. This technique can be used in the production of bulk materials (HgCdTe, InSb), as well as the growth of low dimensional materials such as heterojuctions (quantum well and superlattices), quantum dots and nanowires.

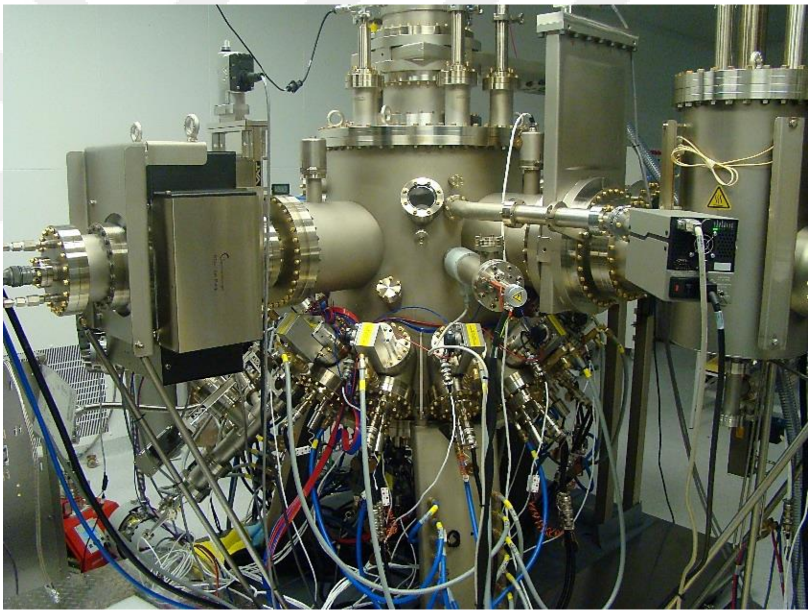

Image 3.1. *An image of Veeco Gen20MC molecular beam epitaxy system in Nanoboyut Research Laboratory.*

Image 3.1 shows the MBE system used in the growth of the InAs/InAsSb superlattice detector structures. In the Veeco Gen20MC system, dual filament SUMO cells are used for Gallium (Ga), Indium (In) materials and standard dual filament cell for Aluminum (Al) material. Valve controlled cracker effusion cells are used for Arsenic (As) and Antimony (Sb) materials. Silicon (Si) and Beryllium (Be) materials were used as dopant atoms by using the single filament effusion cell. Substrate temperatures were measured by an IRCON pyrometer calibrated against the GaSb (1×3)→(2×5) surface reconstruction transition temperature, which was observed at 418 °C under the antimony overpressure conditions.

3.2. Photoluminescence

Photoluminescence (PL) is a technique used to examine the electronic properties of materials. In this process, material is illuminated by a laser and the carriers are excited at their allowed energy levels as result of the absorption of the beam. Later, they return to the ground state by emitting a beam with lower energy than the radiant energy that excites them.

The PL is widely used in semiconductors to investigate properties such as band gap, defect and impurity states or allowable energy levels (quantum well and quantum dots) and material composition. Depend on the penetration depth of the laser beam, it is possible to obtain information from the different layers of semiconductor structure.

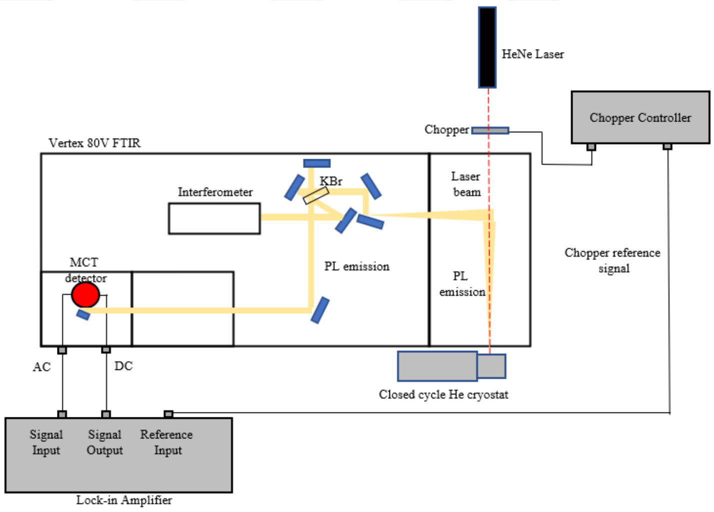

Figure 3.1. *Step-scan based PL measurement configuration used in experiments.*

Within the scope of the thesis studies, the PL technique was used in the determination of the band gap of the superlattice samples, investigation of the localization states and growth calibrations. During the mid-wavelength infrared PL measurements, step-scan based PL measurement was used to eliminate the thermal background and increase the signal to noise ratio (Figure 3.1). During measurements, samples were mounted into a closed cycle Helium cooled cryostat with ZnSe window and excited with 632 nm Helium–Neon laser (20 mW) at a frequency of 5103 Hz. Band-pass infrared filter was used to block the stray light of the excitation laser along the optical path where the PL signal was collected by liquid-nitrogen cooled MCT detector. Intensity based measurements were performed by using the beam attenuator.

3.3. X-Ray Diffraction

X-ray diffraction is a non-destructive characterization technique based on the diffraction of X-rays by materials. Thanks to this technique, it is possible to have information about the structural properties of the crystalline materials such as composition, thickness, crystal quality, roughness etc.

For the growth calibrations, determination of the period thickness and lattice mismatch of the InAs/InAsSb superlattices, Panalytical X'Pert Pro MRD system was used. High resolution X-ray diffraction rocking curve measurements were performed around GaSb (004) symmetry axis with 0.0005° precision.

3.4. Spectral Response

Spectral response measurements were made by using a Bruker Vertex 80V Fourier transform infrared spectrometer to learn the wavelength range in which the infrared detector operates (Figure 3.2).

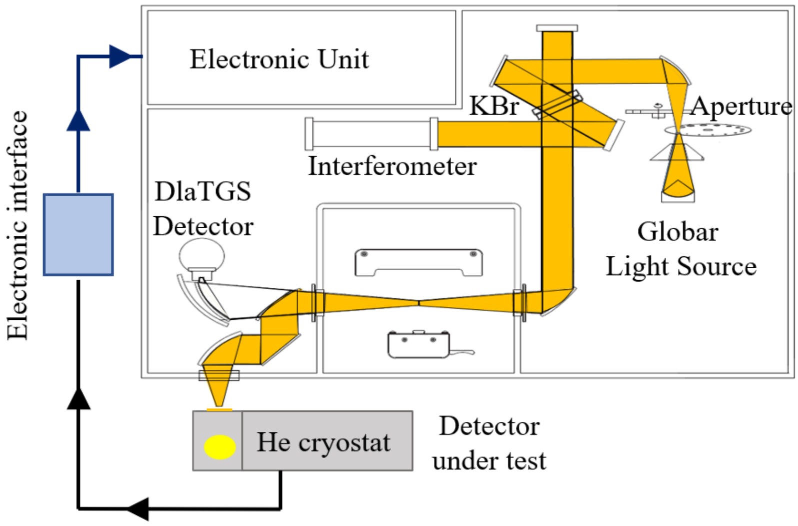

Figure 3.2. *Spectral response measurement setup.*

The raw spectrum of the detectors was corrected by using spectrally flat the DlaTGS detector's spectrum. As for the responsivity measurements and quantum efficiency calculations, a calibrated blackbody source (at 450 °C), lock-in amplifier (SRS-SR850), mechanical chopper, current pre-amplifier (SRS-SR570) and voltage source were used. Temperature dependent measurements were carried out by using closed-cycle He cooled cryostat.

4. EPITAXIAL GROWTH OF InAs/InAsSb SUPERLATTICE MWIR DETECTOR STRUCTURE ON GaSb SUBSTRATE

4.1. Material Design

4.1.1. Determination of Constituent Superlattice Thickness

InAs/InAsSb SL material system is commonly grown on commercially available GaSb substrates. InAs and $InAs_{1-x}Sb_x$ (x > 0.09) layers effect the net strain on the grown crystal as tensile and compressive strains, respectively. To control the net strain and crystal quality during the growth process, individual layer thicknesses and their compositions must be adjusted for strain balanced condition. Constituent SL layer thicknesses (t_{InAs} and t_{InAsSb}) and antimony (Sb) concentration (x_{Sb}) have been determined by using the Equation (4.1) [53] where a_{GaSb}, a_{InAs}, and a_{InSb} lattice constants are 6.0954, 6.0584 and 6.4794 Å, respectively. This equation gives the condition for the average lattice parameter of one period of the SL that is lattice match with the GaSb substrate. Figure 4.1 shows the variation of SL layer thicknesses as a function of Sb content for short-periods of strain-balanced $InAs/InAs_{1-x}Sb_x$ SLs.

$$t_{InAsSb} = \left(\frac{a_{GaSb} - a_{InAs}}{a_{InSb} - a_{InAs}}\right) \cdot \frac{\overbrace{(t_{InAs} + t_{InAsSb})}^{Period}}{x_{Sb}} \tag{4.1}$$

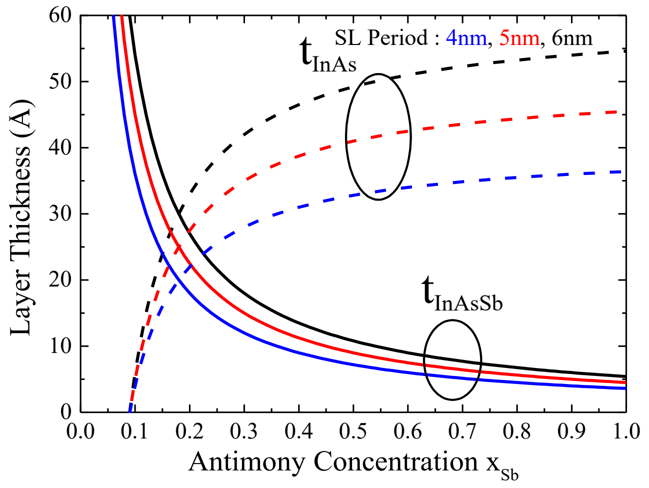

Figure 4.1. *Change of the layer thicknesses as a function of Sb concentration for short-periods of strain-balanced $InAs/InAs_{1-x}Sb_x$ SLs on GaSb substrate [53].*

4.1.2. Selection of the SL Components for Higher Optical Absorption

InAs/InAsSb type II SL system grown with correctly selected layer thicknesses provides strain-balanced condition, as discussed above. One of the important figure of merit of the infrared detectors is quantum efficiency. Absorption ability of the type II InAs/InAsSb SLs are very sensitive to the wave function overlap due to their indirect transition nature. To meet requirements for enhanced quantum efficiency, the layers should be selected for higher wavefunction overlap situation. However, Sb composition in the InAsSb material and SL period thickness limit the optical properties of SL. Figure 4.2 shows the calculated wavefunction overlap and cut-off wavelength for strain-balanced InAs/InAsSb SL for four different SL periods [1]. In MWIR region, to increase the wavefunction overlap for a certain bandgap, or cut-off wavelength, the period thickness should be thin with higher Sb contents in the $InAs_{1-x}Sb_x$ layer. For a constant period thickness, increasing Sb mole content in the InAsSb layers of the SL will increase the carrier confinement in the layers. As a result, overlap of the wavefunctions between the electron and hole state become weaker [54].

When designing these structures, the choice of the Sb composition is also critical issue for reducing the unintentional Sb incorporation to the InAs layers. SL layers are mostly grown at low growth rates (0.3-0.5 ML/s) and growth duration of a single period can take a minute. In this strain-balanced design, 5.1 nm period thickness and 30% Sb composition has been selected in order to enhance absorption (expected absorption coefficient is ~4046 cm^{-1} [54] for 70% overlap) and to minimize Sb incorporation to the InAs layers. After the preliminary work for absorption layer, conduction and valance band energy levels have been calculated by Heterostructure Design Studio (HDS).

For InAs/InAsSb based barrier detectors, ternary material AlAsSb [55], InAs/AlGa(As)Sb [56], InAs/AlAs/InAs/InAsSb [18] and InAs/AlAsSb/InAs/AlAsSb/InAs/InAsSb [57] superlattice structures were used in order to block majority carriers and allow the flow of minority carriers. However, barrier layers can only be used as an electron potential barrier due to the energy alignment of the absorber regions (for MWIR and LWIR detection).

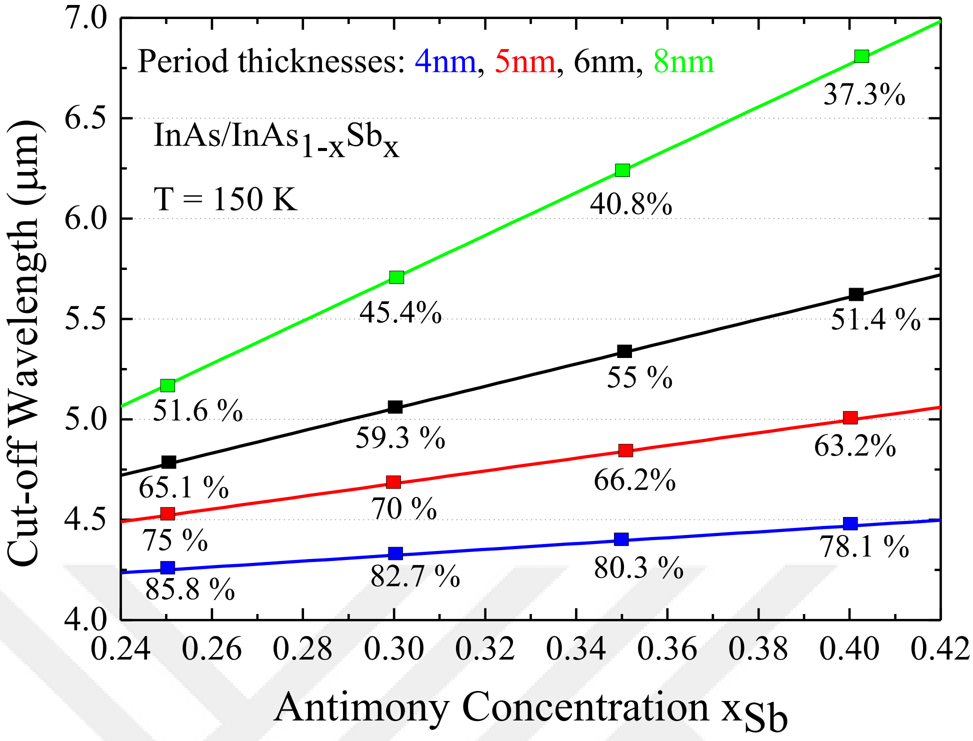

Figure 4.2. *Calculated cut-off wavelengths and wavefunction overlaps as a function of antimony concentration, covering the MWIR region at 150 K, for strain-balanced InAs/InAsSb SL for four different SL periods [53].*

In barrier superlattices where high band gap AlSb materials are used, position of the superlattice's conduction band and valance band can be adjusted by the thickness and composition of the AlSb and the InAsSb layers, respectively. The AlSb divide the InAs layer where the electrons are located and then increase the conduction band level. For a fixed InAs and InAsSb thicknesses, the effect of the AlSb material on InAs/InAsSb superlattice energy bandgap has shown in Figure 4.3. By inserting the two monolayers AlSb in the InAs layer, it is possible to increase the conduction band level up to 256 meV for this superlattice configuration. However, this process increases the lattice mismatch in the superlattice and thus the sample becomes almost impossible to be grown without defects. Therefore, lattice match or strain-balanced condition must be maintained to eliminate lattice imperfection along the grown crystal.

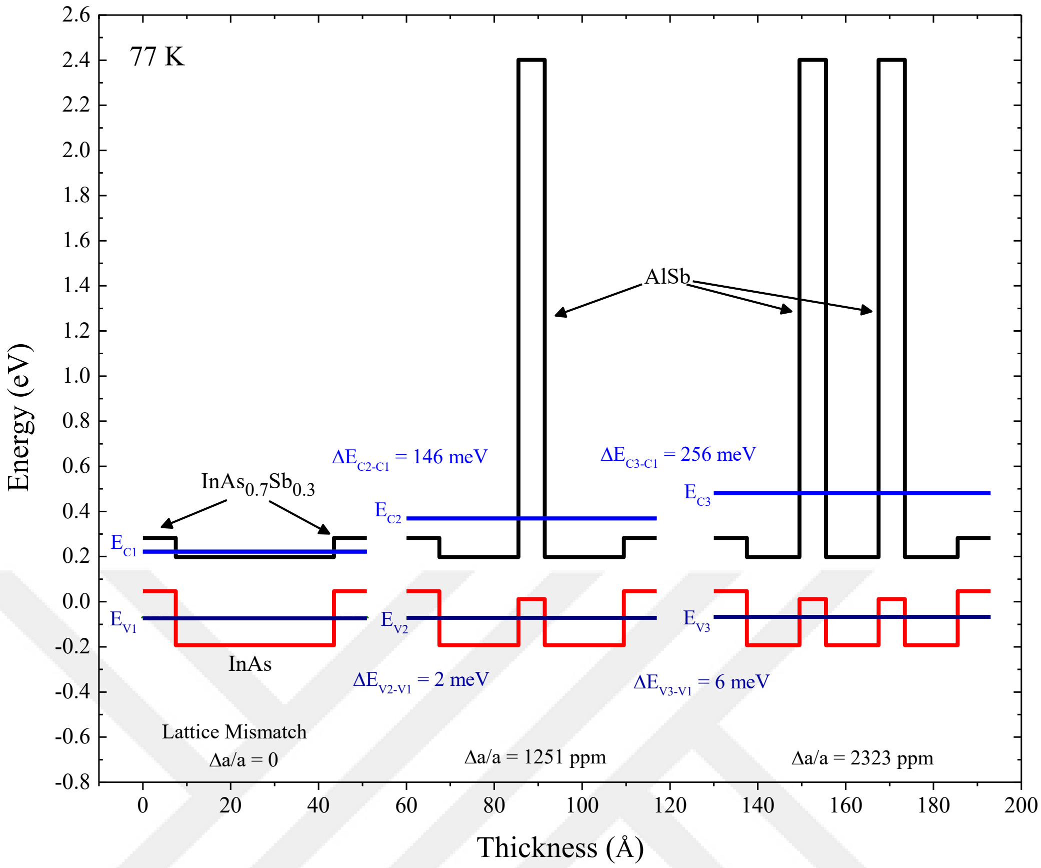

Figure 4.3. *The effect of the AlSb on lattice mismatch and energy levels for InAs/InAsSb superlattice.*

In the process of designing the barrier region, first the strain-balanced structure was determined by using Epitaxy program, then the band gap calculations were performed. To sustain zero valance band discontinuity between the epitaxial regions, InAsSb layer composition and thickness were kept the same as the absorber layer. AlSb was used as a high band gap material and its thickness was chosen so as not to exceed the critical thickness (2 ML). The optimum barrier layer structure was decided as a result of successive X-ray diffraction (XRD) simulations and band gap calculations. Strain-balanced condition has been obtained using six layered superlattice stack with two thin AlSb layers as shown in Figure 4.4 where the simulated XRD rocking curve was given. Period thickness of the barrier superlattice is 75 Å and the layer sequence is 15 Å InAs / 6Å AlSb / 18 Å InAs / 6 Å AlSb /15 Å InAs /15 Å $InAs_{0.7}Sb_{0.3}$. Once the barrier superlattice was determined, band gap calculation have been done.

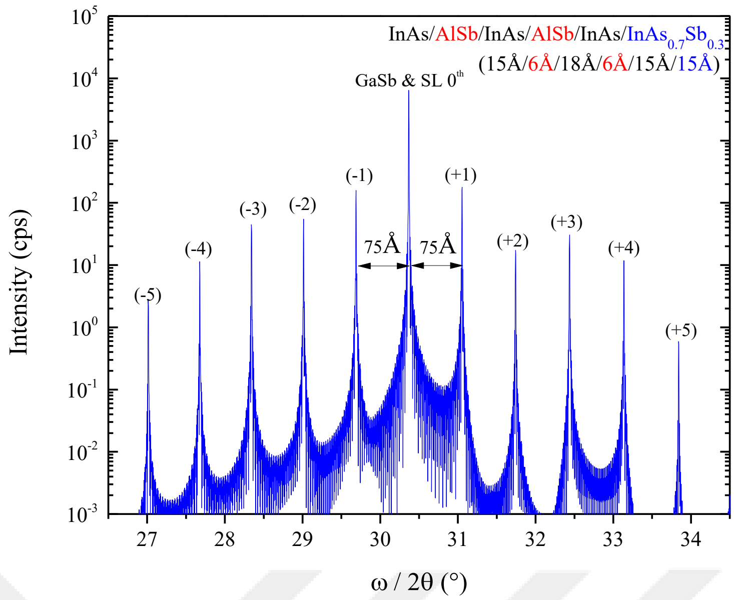

Figure 4.4. *X-Ray diffraction model of electron barrier superlattice.*

Result of the band gap calculation for the optimum barrier superlattice is shown in Figure 4.4. With the incorporation of AlSb layers to the superlattice, conduction energy level increased up by 213 meV at 77 K. The calculated band gap and its conduction band off-set between the absorber layer are about 514 and 212 meV, respectively at 77 K. The valence band discontinue is about 1 meV. Compared to the examples in the literature [18, 57], this barrier height is suitable for the nBn photodetector structure.

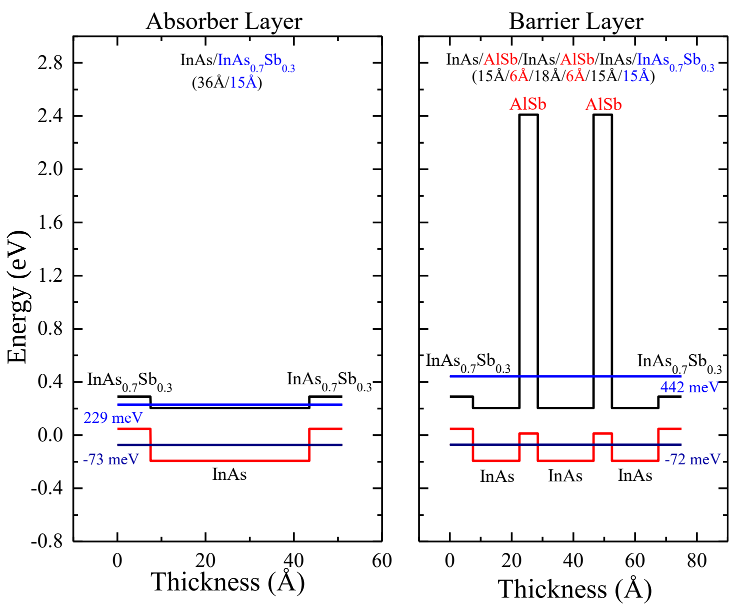

Figure 4.5. *The energy levels of the absorber and barrier superlattice regions at 77 K.*

4.2. Material Growth and Characterization

The barrier layer was restructured to meet operational requirements of the targeted infrared detector and reduce the calibration processes. Since both absorber and barrier layer have similar base materials (InAs and InAsSb), the calibration process started with growing the InAs/InAsSb superlattice (SL) samples.

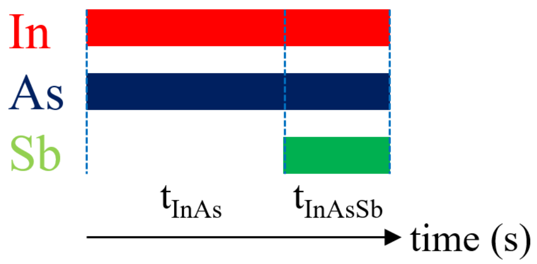

Figure 4.6. *Shutter sequence during the growth of InAs/InAsSb superlattice layers.*

All epitaxial growths were carried out by using a solid-source Veeco Gen20 molecular beam epitaxy (MBE) system equipped with valved arsenic (As) and antimony (Sb) cracker cells, together with gallium (Ga) and indium (In) dual filament effusion cells. Substrate temperatures were measured by an IRCON pyrometer calibrated against the GaSb (1×3)→(2×5) surface reconstruction transition temperature, which was observed at 418 °C under the antimony overpressure conditions. In order the evaluate crystal quality and detector performance, InAs/InAsSb superlattice samples were grown as a p-i-n structure. SL structures used in this study consists of the following layers: a 500 nm p+-GaSb (Be doped) bottom contact, a 220 period of InAs/InAsSb superlattice. The pin SL region, in particular, is composed of 60-periods p-type, 100-periods undoped and 60-periods n-type InAs/ InAsSb SL layers. Figure 4.6 shows the shutter sequence during the growth of the InAs/InAsSb superlattice layer. In and As flux were kept fix all of the growth duration and Sb shutter was opened for the InAsSb layers. Superlattice growths were performed at 450 °C.

For optoelectronic characterization, test diodes were fabricated using photolithography and citric acid-based solution. Top and bottom ohmic contacts (5nm Ti/150nm Au) were evaporated by e-beam deposition technique and SU-8 passivation was applied during the diode fabrication. Square shape test diodes with variable side lengths were used in the course of dark current and optoelectronic measurements. Spectral photoresponse and step-scan based PL measurements were carried out by using a Bruker Vertex 80 V Fourier transform infrared spectrometer. For PL measurements, samples were mounted into a closed cycle Helium cooled cryostat with ZnSe window and excited with 632 nm Helium–Neon laser (20 mW) at a frequency of 5103 Hz. Band-pass infrared filter was used in order to block the stray light of the excitation laser along the optical path where the PL signal was collected by liquid-nitrogen cooled MCT detector. As for responsivity measurements, SR570 low noise current preamplifier and calibrated blackbody source operating at 450 °C were used.

In this growth study substrate vendor and growth parameters were evaluated in two sets. Superlattice samples were grown on GaSb substrates supplied by Semiwafer (named as S-Series samples) and WaferTech (named as W-Series samples) company. Low and high growth rate Indium (In) were used for the S and W series samples, respectively.

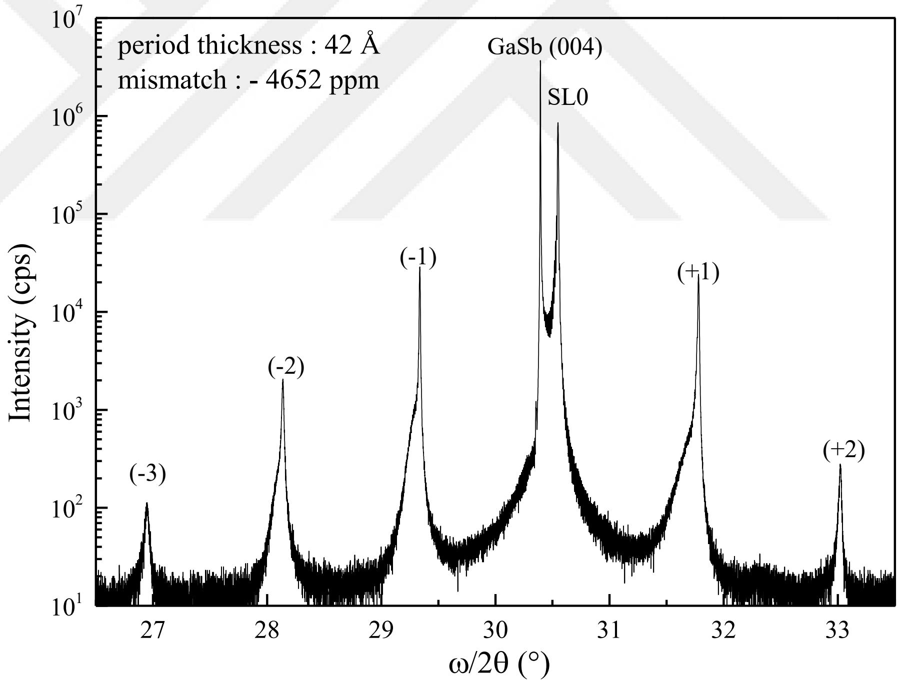

Figure 4.7. *Characteristic X-ray diffraction patterns obtained from first calibration SL sample grown to determine the low-Indium growth rate.*

Figure 4.7 shows the characteristic x-ray rocking curve diffraction patterns obtained from the first InAs/InAsSb superlattice calibration sample used to precisely find low In growth rate. Period thickness of the superlattice sample was found to be 51.5 Å by calculation from the distance between the satellite fringes. Later, growth rate of the In material was calculated from the dividing the total thickness of the one period of the superlattice by the total growth time of the one period of the superlattice. In the second superlattice sample, growth times for the individual layers were adapted to targeted thicknesses. In order to define the Sb composition in the second calibration sample, XRD simulation was performed by using Epitaxy program (Figure 4.8).

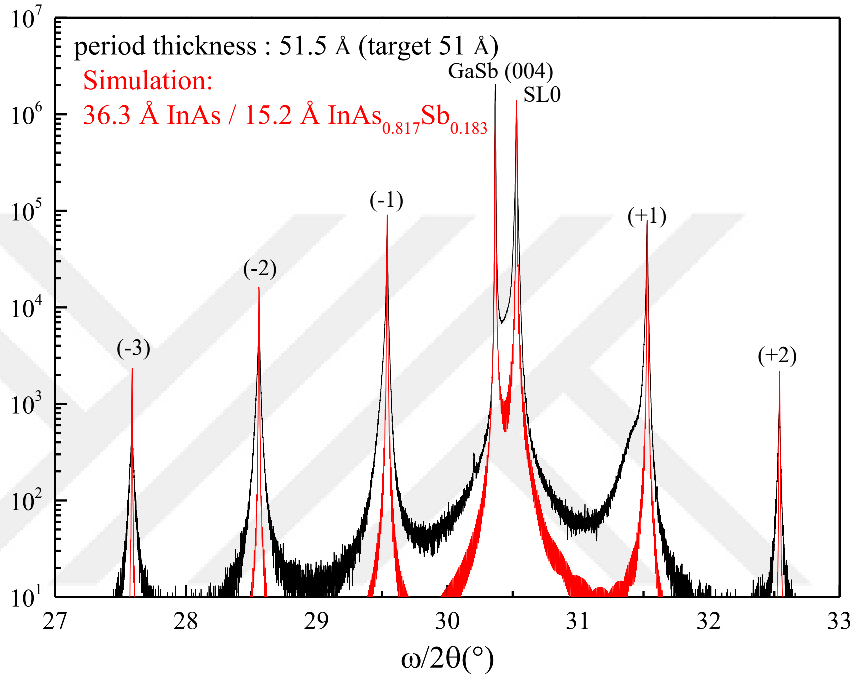

Figure 4.8. *Diffraction pattern and simulation curve belongs to second SL sample grown to find Sb content in the InAsSb layers.*

In the simulation, the period thickness of the superlattice was found to be 51.5 Å as close as the targeted value. However, Sb percent in the InAsSb layer was found to be (81.7%) higher than the value (70%) that provide the strain-balancing condition. After the preliminary calibration works were carried out, a new set sample was grown to meet the strain-balanced condition. In this batch, samples were grown on GaSb wafers supplied by Semiwafer company. Systematically changed in the lattice mismatch between the superlattice 0^{th} peak and GaSb (004) peak are shown in Figure 4.9(a). Targeted layer thicknesses, Sb composition and strain-balanced condition were met in the sample called "S4" (Figure 4.9(b)). In order to evaluate grown crystal/wafer quality and photodiode performances of first batch samples, defect inspection, photoluminescence (PL) measurements and devices fabrications were performed.

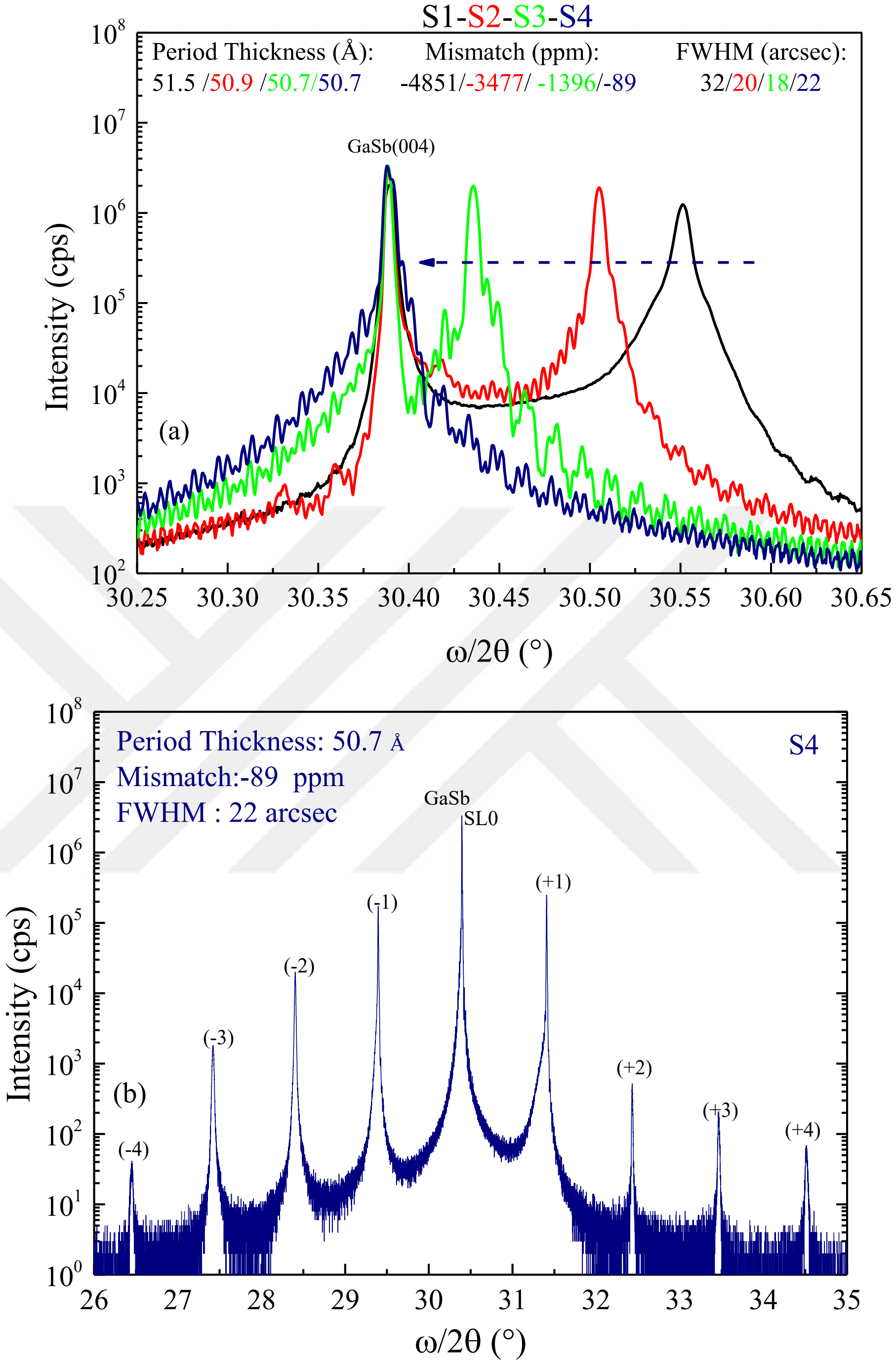

Figure 4.9. *Strain balancing study: graph (a) presenting the changing the lattice mismatch between the substrate and superlattice zero order peaks and (b) general view of the diffraction pattern of the strain-balanced superlattice sample.*

For the first batch samples, despite a few numbers of oval defects without cores were detected on the sample surface (Figure 4.10), PL and optical responses could not be observed. Growth-related crystal imperfections such as dislocations, point/oval hillock defects and spitting of the group III materials degrade the performance of the grown sample. Some of the macro defects extend to the sample surface (spitting cores) and their densities and morphologies can easily be evaluated by optical and scanning electron microscopes (SEM). However, most of the dislocations and oval defects cannot be easily observed in case of being covered under epitaxial layers.

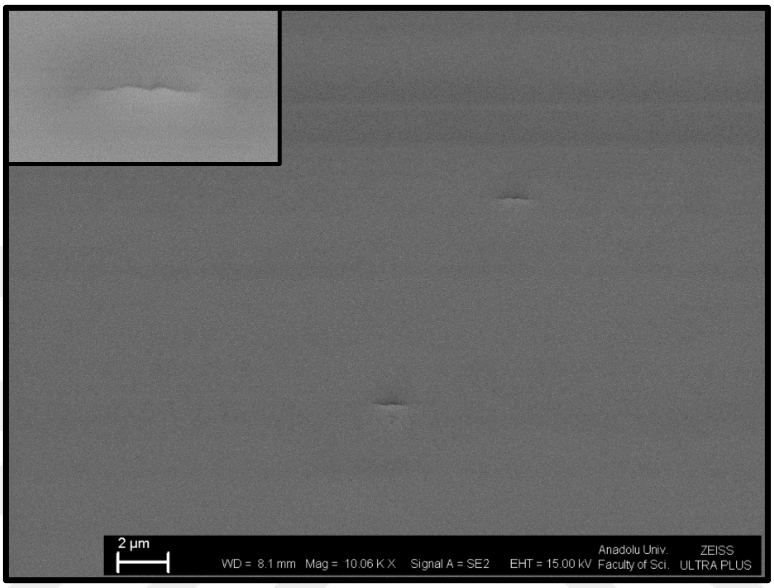

Figure 4.10. *SEM image of the oval defect formation on the surface of sample S4. Inset shows 60 kx magnification of the defect.*

In order to delineate crystal imperfections into the superlattice samples, defect selective etching process was performed. Samples were dipped into the HCl based selective solution and defect formations and their densities were imaged by using Nomarski microscope. As shown in Figure 4.11, highly mismatched samples (S1 and S2) have both oriented micro-defects and oval defects. Despite oriented micro-defects were not observed on top of the sample surface, they appeared in the later stages of the etching process. Note that during the growth of S1 and S2 indicated that samples were relaxed as dislocations due to highly mismatch between the superlattice and substrate. However, no relationship was observed between the oval defects and the mismatch. For the S series samples, it is believed that changed growth parameters to meet the strain balance condition and also residual native oxide from the GaSb substrate caused oval defects. Since crystal defects act as non-radiative recombination centers and shunt paths that degrade the detector performance, PL and optical response could not be observed from this set.

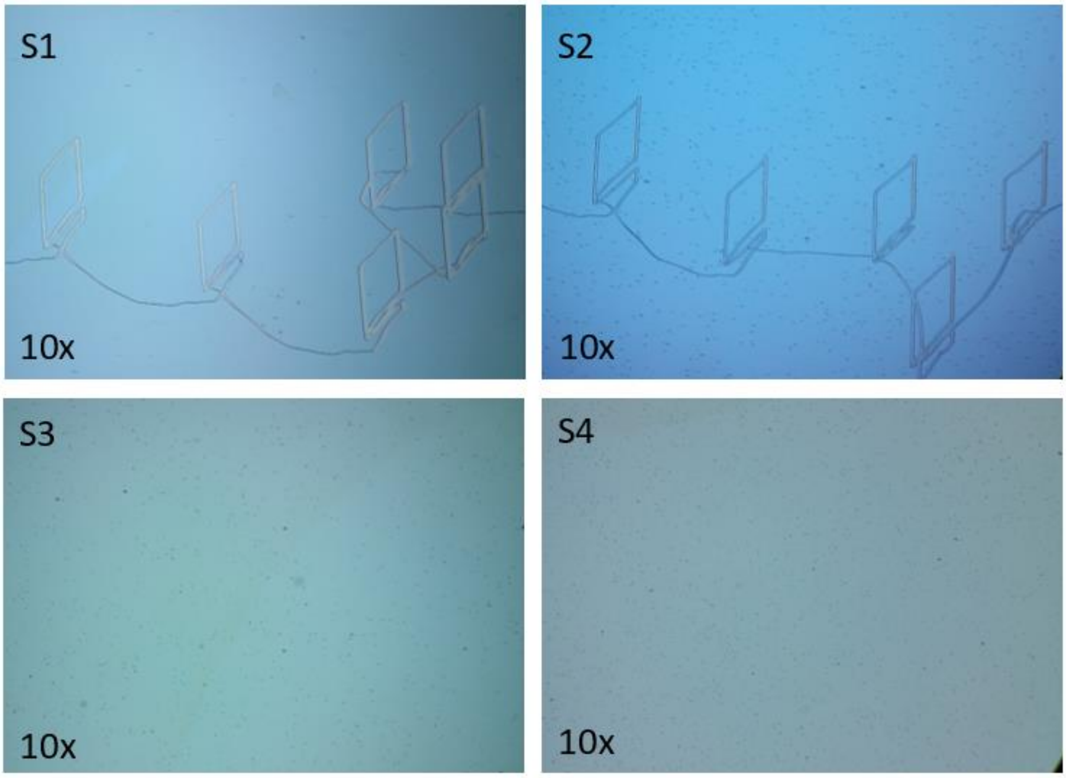

Figure 4.11. *Nomarski microscope images of the investigated samples after 4 minutes dipped into the defect selective solution.*

For the second batch (W-Series samples), flux calibrations were performed for the high In growth rate and then W1 named sample was grown to determine the Sb concentration in the InAs/InAsSb SL. Then subsequent sample growths were performed for both meeting the strain-balanced condition and improving the detector performance. Each new sample was grown after getting feedback from the investigated sample. Comparison of the PL spectrum of the W-series is shown in Figure 4.12. Among these samples, the best optical signal intensity was observed at W2. Though the first sample of this group (W1) ($\Delta a/a$ = 1217 ppm) has a PL signal but photo-response could not be obtained after the device fabrication. In order to observe the effect of the V/III ratio, W2 sample (-1405 ppm) was grown with higher V/III ratio than the W1 sample. This effect increased the luminescence signal about 3.5-fold and first photo-response was observed from the W2 SL sample during the material quality improvement stage (results of the optoelectronic measurements are given in detail below). Later, W3 sample (-545 ppm) was grown under higher Sb flux than the W2 sample to reduce lattice mismatch.

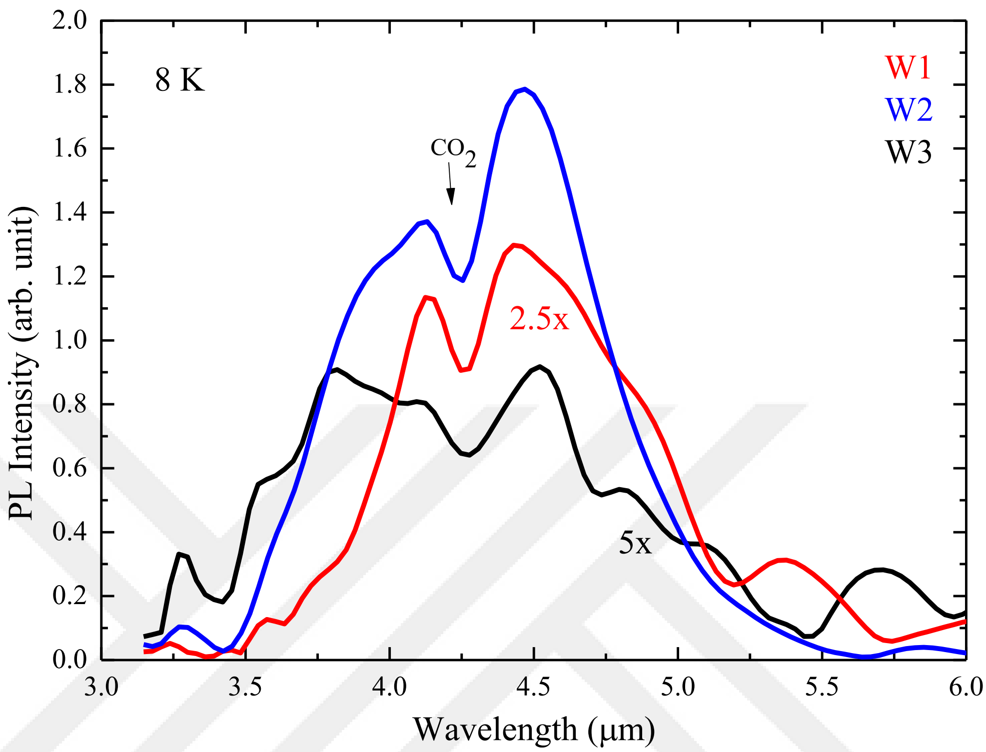

Figure 4.12. *Low temperature (8 K) step scan-based photoluminescence measurements of W-series samples. The measured signals belong to W1 and W3 samples were multiplied for easy comparison.*

Temperature-dependent spectral response measurements of the W2 and W3 samples are given in Figure 4.13. Cut-off wavelength ($\lambda_{\%100}$) for the W2 and W3 SL detectors at 80 K were found as 4.6 and 4.9 μm, respectively. The high Sb concentration lifts the valence band of the InAsSb layer and this causes red-shift in the band gap of the W3 SL sample. Both samples have a comparable photo-response signal level at corresponding temperatures. While voltage requirement of the W2 detector increases with the increase in the temperature, W3 detector reaches the highest level at photovoltaic mode at investigated temperatures (between the 80 and 160 K). As voltage was applied to the W3 sample (80-160 K), spectrum became noisier due to the fact that the dark current in the structure increased. At higher temperature (>160 K), W3 sample needed reverse bias to sustain the high optical response (not shown here). One possible reason of the voltage demand of the W2 detector may be related to low mobility photo-carriers that require an external reverse bias for more efficient sweeping towards the contacts. The highly mismatched lattice may lead to an increase in the residual carrier density at intrinsic region of the p-i-n diode and reduce the carrier mobility.

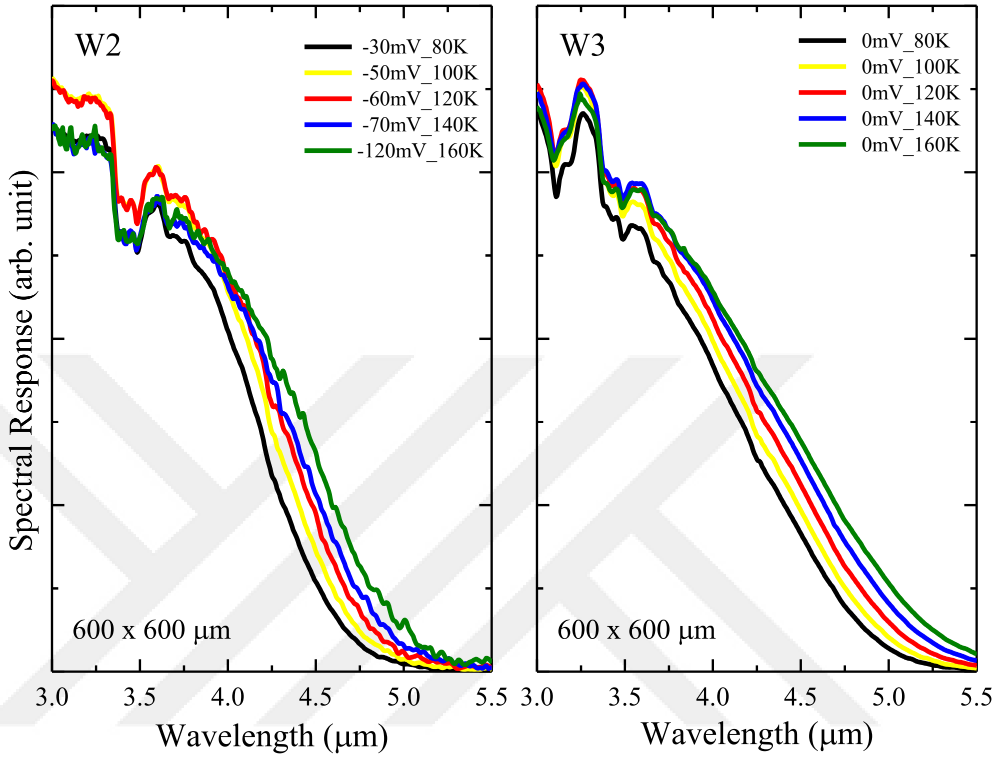

Figure 4.13. *Temperature dependent spectral response of W2 and W3 SL p-i-n structures. Given voltage values are indicated the maximum optical response obtained at related temperature.*

For further comparison of the both detectors' optical performance, responsivity measurements were performed by using calibrated blackbody. As shown in Figure 4.14, the responsivity of the detectors sensitive to the temperature changes under the photovoltaic mode. Photovoltaic-mode measurements also reflect voltage dependence of the detector performances. Although both samples have similar responsivity value (0.41 A/W @4 µm) at 80 K, samples show a different trend with the increase in the temperature. W3 sample reaches its maximum level at 0.51 A/W (@ 4 µm) at 160 K. On the other hand, W2 sample exhibits decreasing trend and it dropped down to 0.26 A/W (@4 µm) at 160 K. In order to better evaluate and compare optical performances, quantum efficiencies are shown in Figure 4.15. It can easily be seen that the difference between the quantum efficiency values of the samples increases towards higher operating temperatures. At 160 K, quantum efficiencies were calculated as 8.1 and

15.8% for W2 and W3, respectively. More detailed study with temperature dependent absorption measurements may explain the reason of the increase in the quantum efficiencies for the W3 sample.

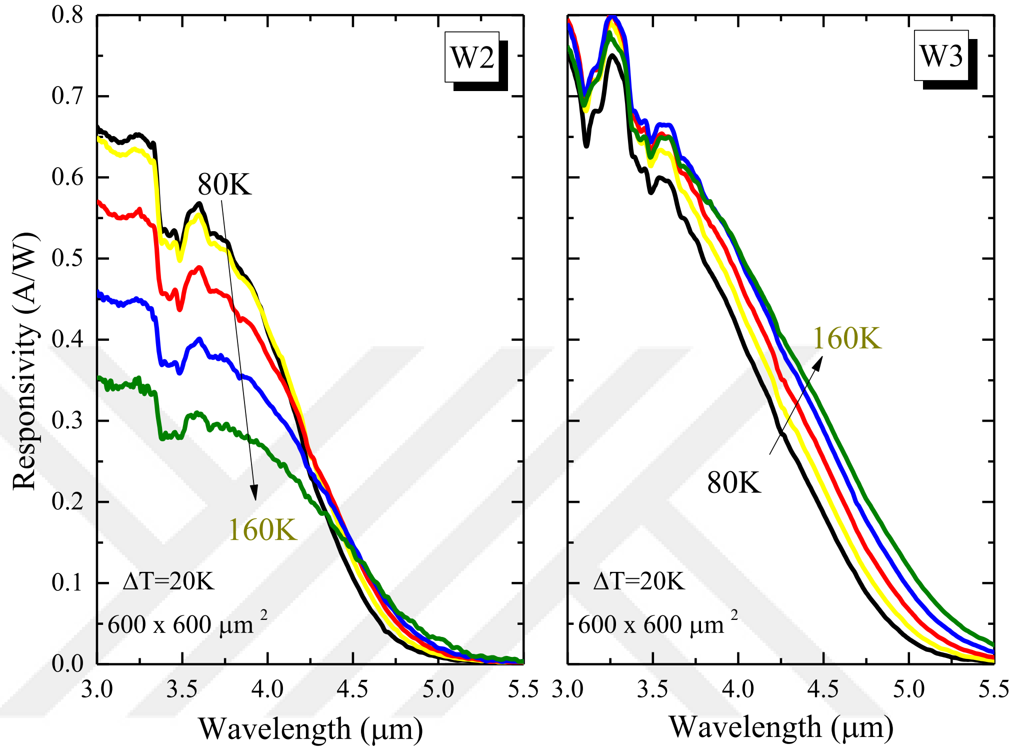

Figure 4.14 *Temperature-dependent responsivities of W2 and W3 SL samples under photo-voltaic mode.*

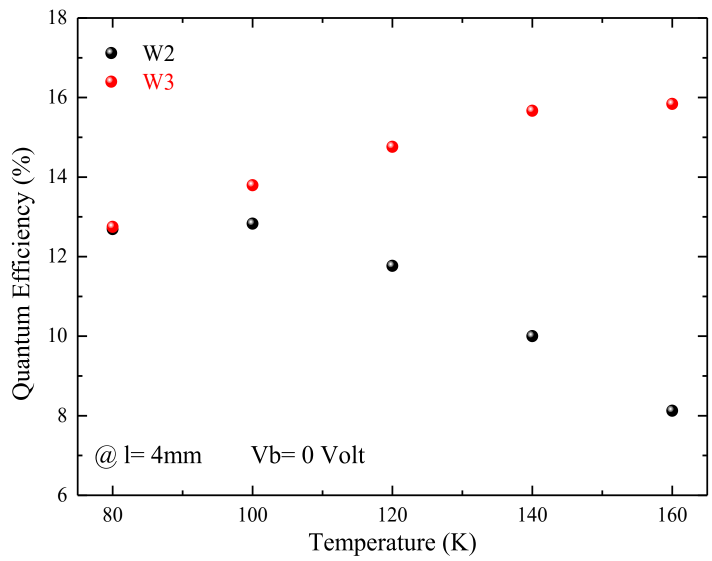

Figure 4.15 *Comparison of the quantum efficiency of both samples at temperatures between 80 and 160K.*

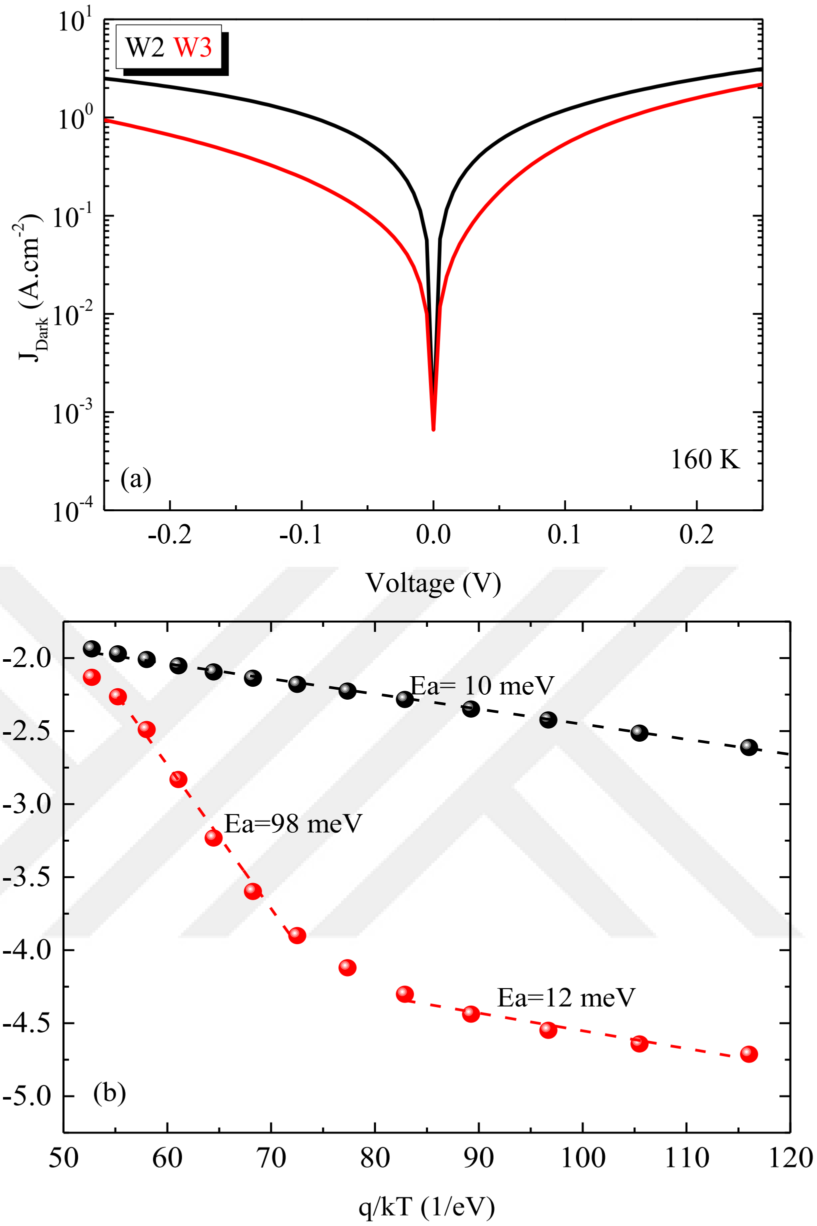

Figure 4.16. *(a) Dark current density at 160 K and (b) Arrhenius plot of the samples under 10 mV reverse bias.*

In Figure 4.16(a), dark current densities for the single pixel diodes for both samples at 160 K are presented. Dark current density values of the W2 and W3 samples were found to be 1.1×10^{-2} and 20×10^{-3} A.cm^{-2} under 10 mV reverse bias, respectively. In order to investigate the dominant current mechanism in the test diodes, Arrhenius plot of the dark current densities under 10 mV reverse bias were derived and shown in Figure 4.16 (b). For the high-temperature regime of the W3 sample, an activation energy of ~98 meV was extracted. This indicates that the defect levels exist near the center of the band gap (G-R) of the superlattice. Extracted low activation levels (10 and 8 meV) for the both samples can be related to surface contribution. Since the MWIR InAs/InAsSb SL has degenerate n-type surface states [58], contribution of the surface current to the total dark current may be more dominant. The difference in the current densities between the samples is mainly attributed to the comparably higher defect density in highly lattice mismatched W2 sample (Figure 4.16 (a)).

In summary, for the material development of the InAs/InAsSb based SL MWIR nBn photodetector, effects of the substrate vendor and growth rates on the crystal quality has been investigated by using test pin SL structure. Although the best sample (W3) has a thin absorber layer and still needs optimization of the growth parameters/fabrication process, it has comparable performance to the similar structures in the literature (Table 4.1).

Table 4.1. *Summary of the performance of the InAs/InAsSb MWIR SL photodetectors at 77 K.*

Structure	λ_c (µm)	J_{dark} (A/cm^2)	QE (%)	A.L. (µm)	Ref.
nBn	5.1	1×10^{-7}(100mV)	45 (@4 µm)	2	[18]
pin	5	1.1×10^{-1} (10mV)	39.7	2	[59]
pin	5.1	6.1×10^{-4}(300 mV)	23.3 (@2.8µm)	4.4	[60]
pin	5.4	2.1×10^{-4} (10mV)	20 (@4 µm)	1	[61]
pin	4.9	7.4×10^{-4} (0mV)	12.7(@4 µm)	0.5	This work

In order to investigate the effect of the excess group V flux on the superlattice, two sample (W4-W5) were grown by using InAs-Sb-InAsSb-As flux sequence as shown in Figure 4.17(b). During the two seconds, Sb and As flux were applied to the InAs→InAsSb and InAsSb→InAs layer transitions, respectively. Results of dark current and responsibility measurements of the new samples were compared with the reference W3 sample to evaluate the growth modification.

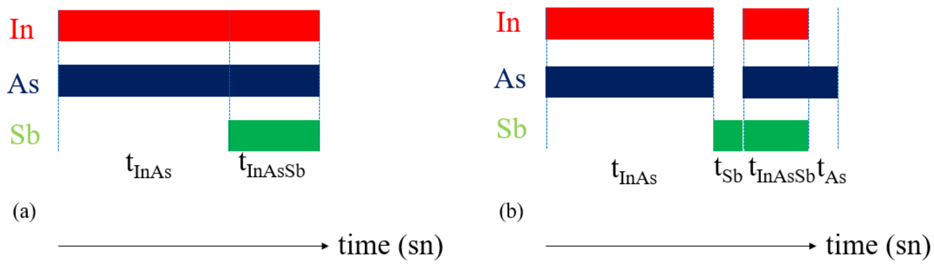

Figure 4.17. *Shutter sequence during the growth of InAs/InAsSb superlattice layers for (a) reference (W3) and (b) modified growth (W4-W5).*

In Figure 4.18(a), dark current densities for the samples at 80 K are presented. Dark current density values of the W3, W4 and W5 samples were found to be 5×10^{-3}, 1.8×10^{-3} and 7.6×10^{-3} A.cm^{-2} under 10 mV reverse bias, respectively. Even if all samples have high dark current densities, W4 sample has prominently lower dark current density than the reference W3 sample. When the optical performances are compared, samples have the close responsivity values in the similar spectrum (Figure 4.18 (b)).

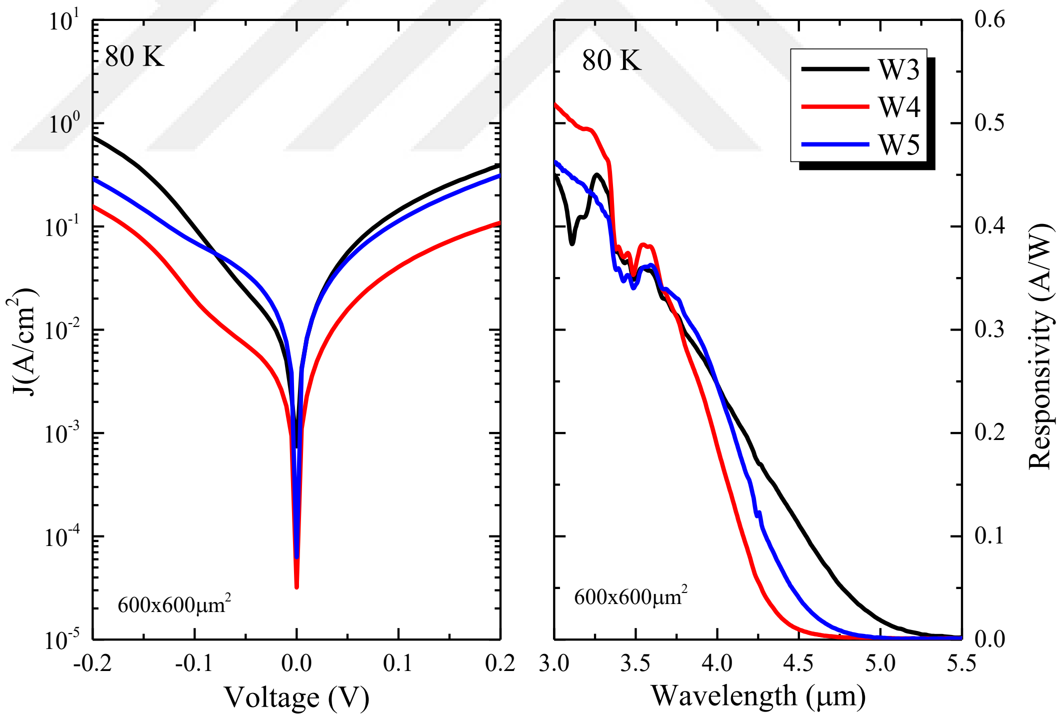

Figure 4.18. *(a) Dark current densities and (b) responsivities of the reference and test samples at 80 K.*

During the growth of the superlattice, As and Sb soak may increase the performance of the superlattice detectors. However, adding excess atoms between the individual layers of the superlattice makes difficult to adjust the cut-off wavelength and lattice mismatch.

The sample W4 was grown by modified growth recipe and it had better performance than the reference sample. However, the recipe is still needed to be optimized to reach a good crystal quality and desired detector performance. It should be noted that the feature observed at around 3.5 μm is due to the water related absorption (thin layer of ice on the diode’s surface).

5. EPITAXIAL GROWTH OF InAs/InAsSb BASED nBn MWIR DETECTOR STRUCTURE ON GaSb SUBSTRATE

5.1. Material Design

In the previous chapter, the experimental results of InAs/InAsSb SL samples grown as a pin diode were demonstrated (Figure 5.1(a)). After the preliminary calibrations for InAs/InAsSb SL structure, first test nBn detector structure was grown as shown in Figure 5.1 (b). Reference structure consists of 60-periods n-type (1×10^{18} cm^{-3}) top and bottom contact InAs/InAsSb SL layer. Absorber region of detector is composed of the 100-periods n-type (1×10^{16} cm^{-3}) InAs/InAsSb SL. Note that InAs/InAsSb SL layers in the sample has the same individual layers. InAs/AlSb/InAs/AlSb/InAs/InAsSb layer sequence were used for the wide band gap SL barrier region. Period thickness of the barrier SL region is 75 Å. The calculated band gap and its conduction band off-set between the absorber layer are about 514 and 212 meV, respectively.

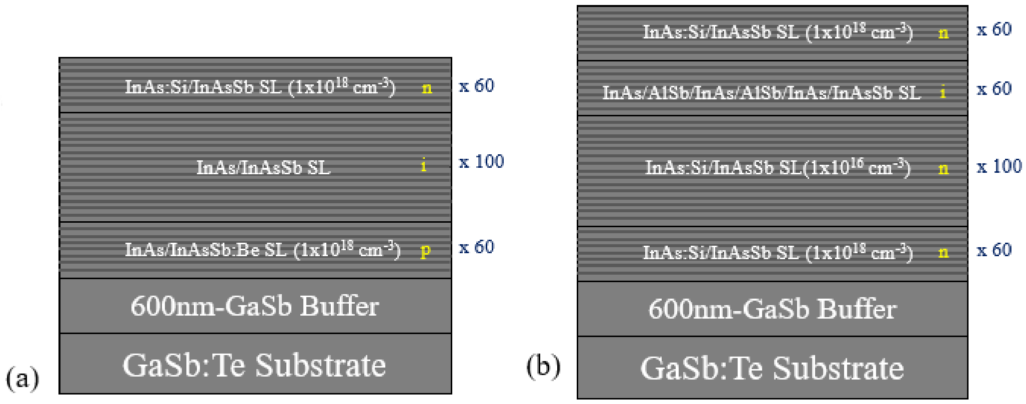

Figure 5.1. *Schematic drawings of the (a) pin and (b) nBn reference detector structures.*

5.2. Material Growth and Characterization

Figure 5.2 shows the characteristics high resolution X-ray diffraction (HR-XRD) patterns obtained from the nBn detector. The sample has two different diffraction periodicity belongs to absorber/contact regions and the electron barrier SL layers. Both SL region had designed to meet strain-balanced condition in the suggested nBn detector structure. For the absorber SL region (36 Å InAs / 15 Å $InAs_{0.7}Sb_{0.3}$), period thickness and the lattice mismatch are 50.9 Å and 374 ppm, respectively. This small amount of mismatch value (under the compressive-strain) indicates that the Sb composition in the

InAsSb ternary material is 1.2% higher than the desired value. For the barrier SL region (15 Å InAs / 6 Å AlSb / 18 Å InAs / 6 Å AlSb / 15 Å InAs / 15 Å $InAs_{0.7}Sb_{0.3}$), calculated period thickness (75.5 Å) is very close to the targeted value (75 Å) but there is a considerable tensile strain (-3285 ppm). AlSb material has two separate functions in the barrier SL: it used to increase the conduction band of the barrier SL region and its high lattice constant increases the average lattice constant of the SL to meet the strain-balance condition. The possible explanation for the tensile strain in the barrier SL could be AlAs-like interface zone may form at every InAs→AlSb (and also AlSb→InAs) layer transitions and therefore average lattice constant of the SL is reduced. In the InAs/AlSb SL crystal structure, they have no common anion or cation atom at the interface zone and there are two possible natural interfaces could exist as AlAs and InSb. Since the AlAs-like interface is more stable than the other possible InSb-like interface formation [65], AlAs-like interfaces could exist in our barrier SLs. The other possibility of the tensile strain in the barrier material may be related thin AlSb material turns to AlAsSb compound due to high As background in the chamber.

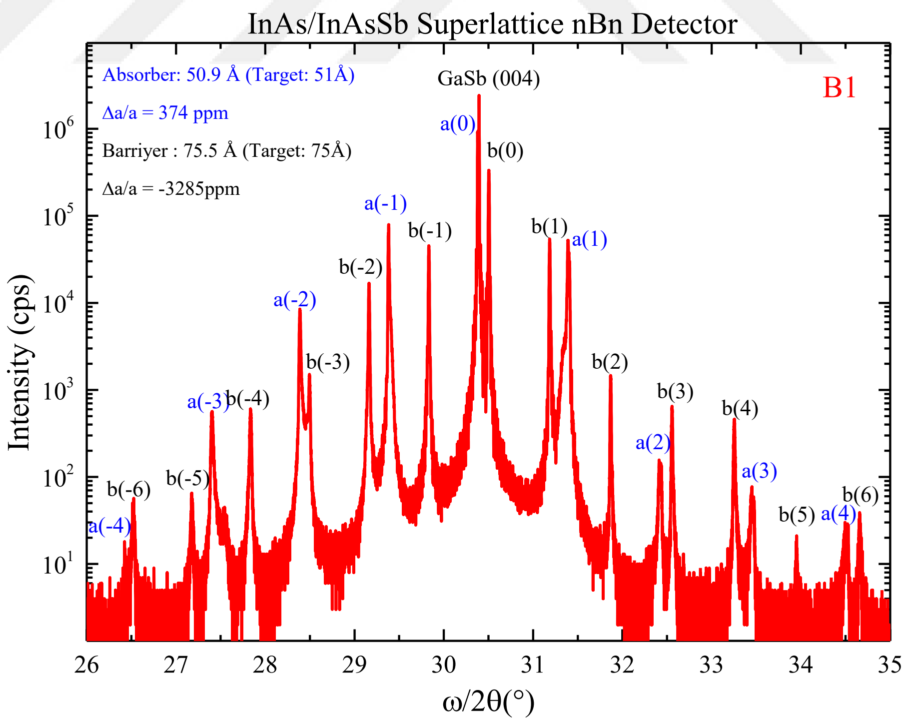

Figure 5.2. *HR-XRD scan of the nBn detector structure. The data shows the two distinct superlattice period: the absorber and the electron barrier.*

In our nBn detector structure, high band gap SL blocks the majority electrons and allows the photocarrier holes to reach the contact layer. In order to investigate the SL band structures in the grown sample, photoluminescence (PL) measurement was performed. As shown in Figure 5.3, two distinct band gap regions were observed in the grown detector structure. PL peak position for the barrier and the low-band gap material were found to be 2.64 µm (~470 meV) and 4.77 µm (~260 meV), respectively. Difference between the calculated and experimental values may indicate presence of the unwanted potential barrier or quantum well for photocarrier holes at the valence band. The effect of the difference will be discussed in the optoelectronic measurement section.

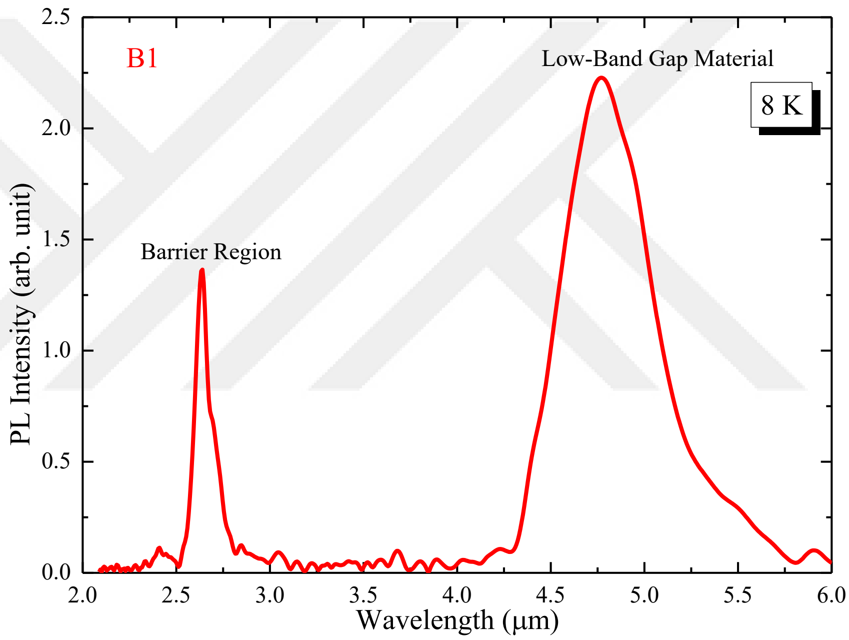

Figure 5.3. *Low temperature (8 K) photoluminescence spectrum for B1 named nBn sample.*

Since the high lattice mismatch, unwanted interface formation and changes in the desired material composition can affect the crystal quality as well as the band gap levels, every new material growth was performed according to the targeted material design and operate as a MWIR detector (Figure 5.4). In order to evaluate growth parameters and develop the desired nBn detector structure, four different detector structures were grown as shown in Table 5.1.

Table 5.1. *Changes in the detector structures during the material growth.*

Sample	Structure	Information about the grown sample
B1	nBn	Reference nBn structure
B2	nBn	(i) 20-periods p-type doped barrier layer, undoped top contact layer
B3	nBn	(i) 40-periods p-type doped barrier layer, undoped top contact layer (ii) 2 seconds As and Sb soaks for the layer transitions (iii) V/III ratio had been increased
W4	pin	(i) Reference p-i-n diode structure (ii) Same recipe as the B3 sample was applied for the InAs/InAsSb SL layers.

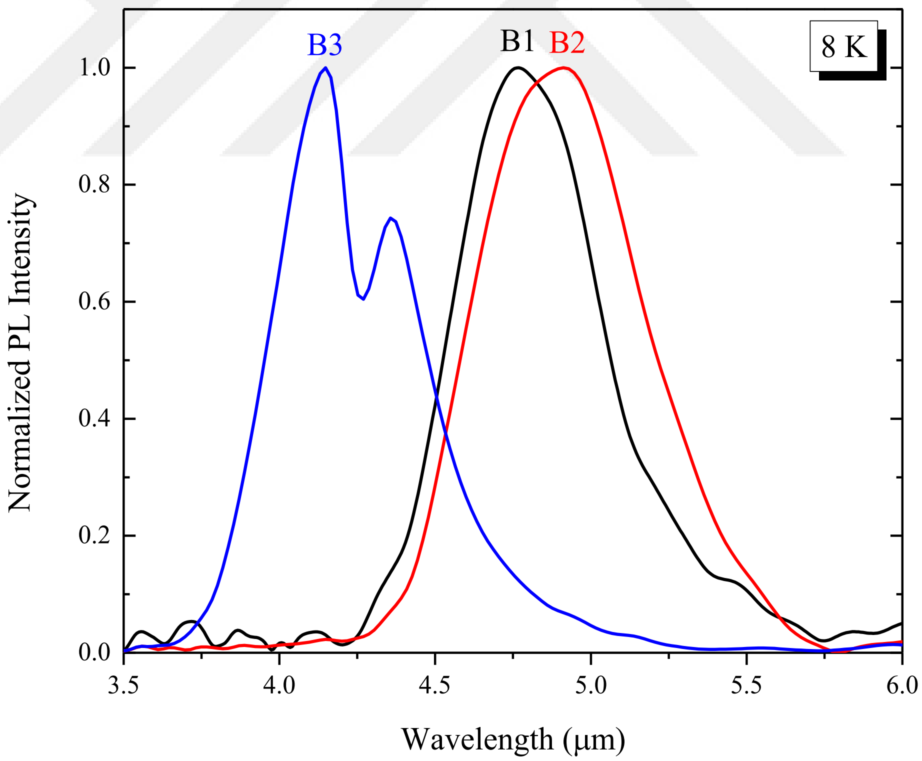

Figure 5.4. *Photoluminescence spectrum of the nBn detectors at MWIR regions.*

For the reference structure (named as B1), period of the SL barrier is 75 Å and calculated band gap is 514 meV at 77 K. Barrier layer and absorber region are same valence band level and calculated conduction band offset is 212 meV at 77 K. During the growth of the material, atoms could segregate the adjacent layers. This movements may degrade the targeted material composition and fluctuate layer thicknesses in the SL. As a result, band line-up at the valence band may misaligned and unwanted (i) quantum well or (ii) potential barrier may formed at the valence band as shown in Figure 5.5.

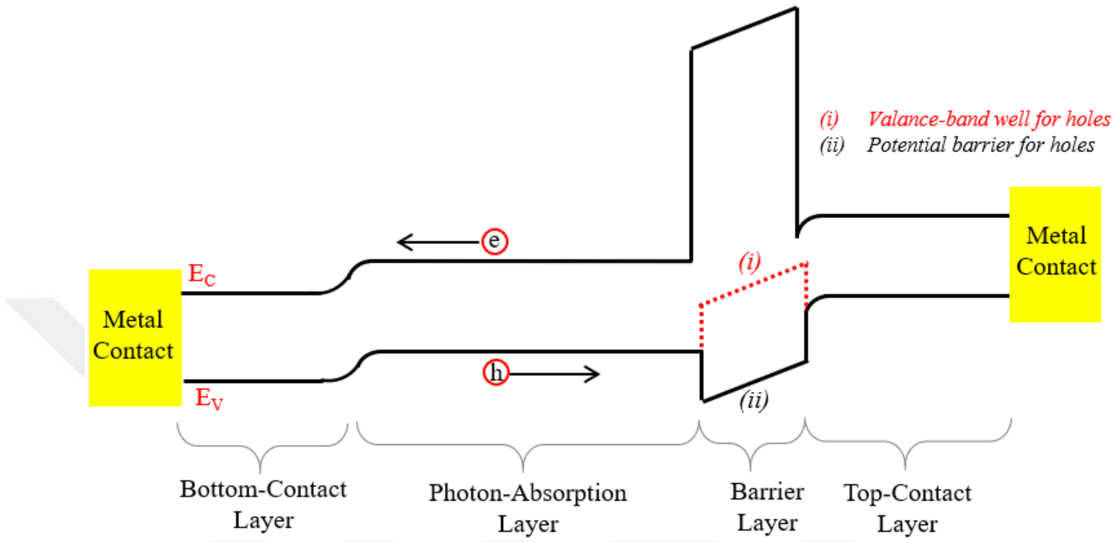

Figure 5.5. *Unwanted (i) quantum well and (ii) potential barrier formation at the valence band in the nBn detector structure.*

As listed in the Table 5.1, three nBn detector structure were grown. Spectral responses of the investigated detector structures are shown in Figure 5.6. Sample W3 (pin diode) is also shown in the same figure in order to compare optical response of the pin and nBn detector structures. In the previous chapter, it was shown that sample W3 could operate up to 160 K without external bias in the mid-wavelength infrared (MWIR) region. The first nBn sample (B1) has very weak response in the MWIR region and most of the optical signal comes from the barrier SL region which corresponds its fundamental transition energy levels. When the bias was applied to the sample B1, significant signal improvement in the MWIR region was not observed. In the voltage dependent experiments, detector reached the saturation limit and all the optical signal disappeared due to high dark current level. Main reasons of the low signal in the MWIR were attributed by high dark current level and possible unwanted potential barrier formation at valence band (Figure 5.5). Other growth runs (B2 and B3) were conducted in order to suppress the high dark current level and reduce potential barrier. For this purpose, V/III ratio was increased to evaluate the growth-related imperfections and barrier layer was doped with p-type dopant atom (Be) to reduce barrier at the valence band. To facilitate the access to the top contact layer for photo-carrier holes, the thickness of the barrier layer was reduced. However, in B2 and B3 samples, no MWIR signal were detected. The collected optical signal comes from the GaSb buffer layer (Figure 5.6). Since the aforementioned layers (buffer, barrier and absorber layers) have distinct band gap from each other, they can show themselves in the different regions at the spectrum. Comparing the signal levels of barrier detectors and pin diode, it was observed that pin diode has higher optical response. Hence, nBn detectors need higher gain to collect optical signal. When the bias applied to the nBn detectors in order to test whether the unwanted barrier formation and collect much more photocurrent, detectors reached the saturation level as in the sample B1. This high dark current level (2×10^{-4}A/cm^2, @80 K) also indicates that the barrier layer could not reduce the dark current level in the detector and the photocurrent may probably be overwhelmed by the high dark current.

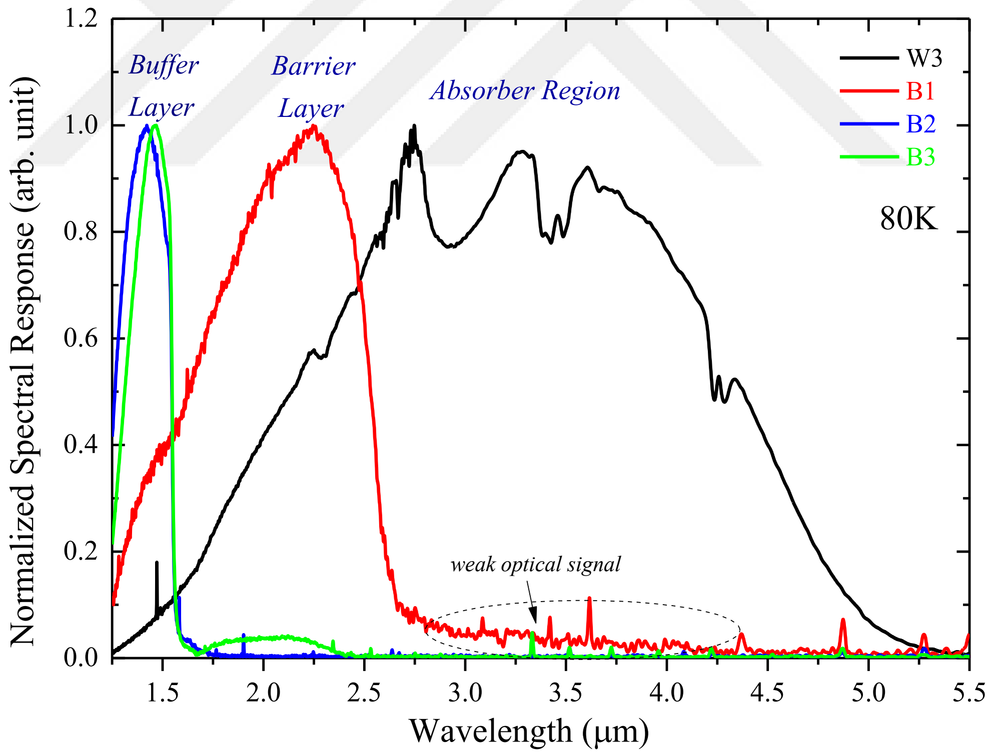

Figure 5.6. *Optical response of the nBn samples with W3 pin diode (80K).*

5.2. Photoluminescence Measurements for Superlattice Structure Analysis

In order to investigate the localized states in the SLs, temperature dependent photoluminescence measurements were conducted. The measurements were performed on B2 and B3 samples which had high luminescence signals and results of the measurements were shown in Figure 5.7 and Figure 5.8 respectively. For both samples, blue shift was observed at the low-energy side of the luminescence signal at temperature between 10-45 K. On the other hand, above 45 K, the tendency to the red-shift was observed.

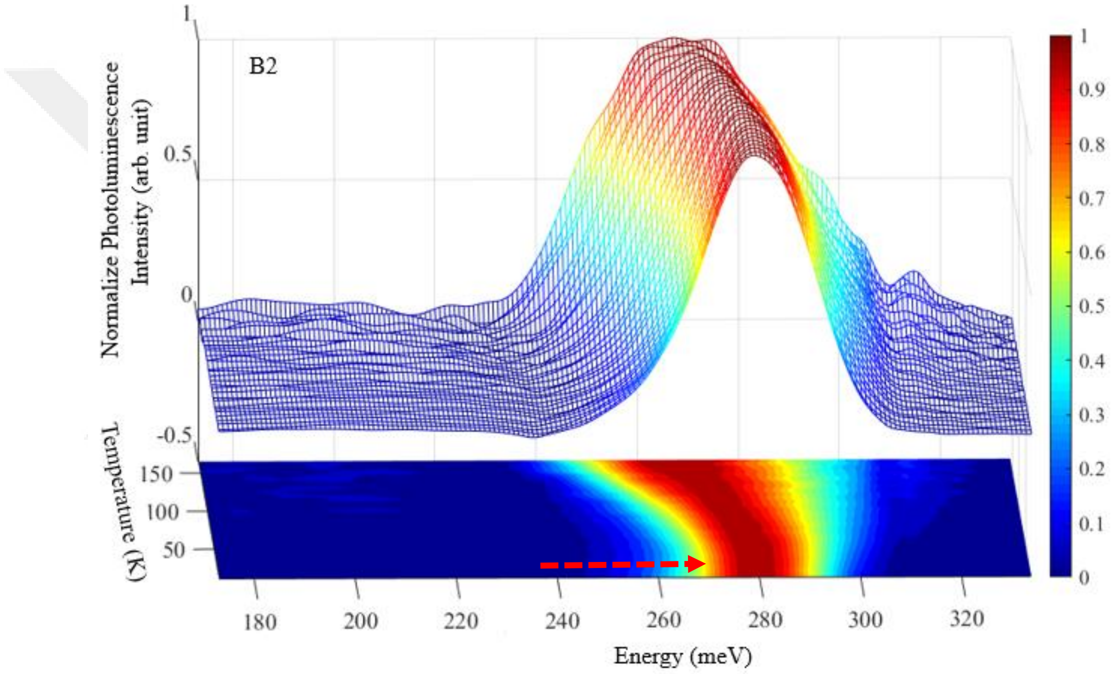

Figure 5.7. *Temperature dependent photoluminescence measurement of B2 nBn detector structures. The red arrow shows the blue-shift in the low energy side of the spectrum.*

In order to determine the peak movement of the samples, bi-Gaussian fit model was used. Since the shape of the luminescence spectrum of the B3 sample was distorted by CO_2 absorption, peak analysis could not be performed for this sample. The bi-Gaussian peak analysis of the B2 sample is presented in Figure 5.9. As seen in Figure 5.9, low energy side of the peak (w1 region corresponds to transitions between the low energy levels in the miniband) shows blue shift (10 K $<T<$ 45 K). This trend indicates that the SL miniband has localized states. The origin of the localized states is attributed layer thickness and alloy composition fluctuations in the SLs [63-64]. In our materials, difference in the expected band gap and mismatch values may point out the existence of the disordered layers in the SL.

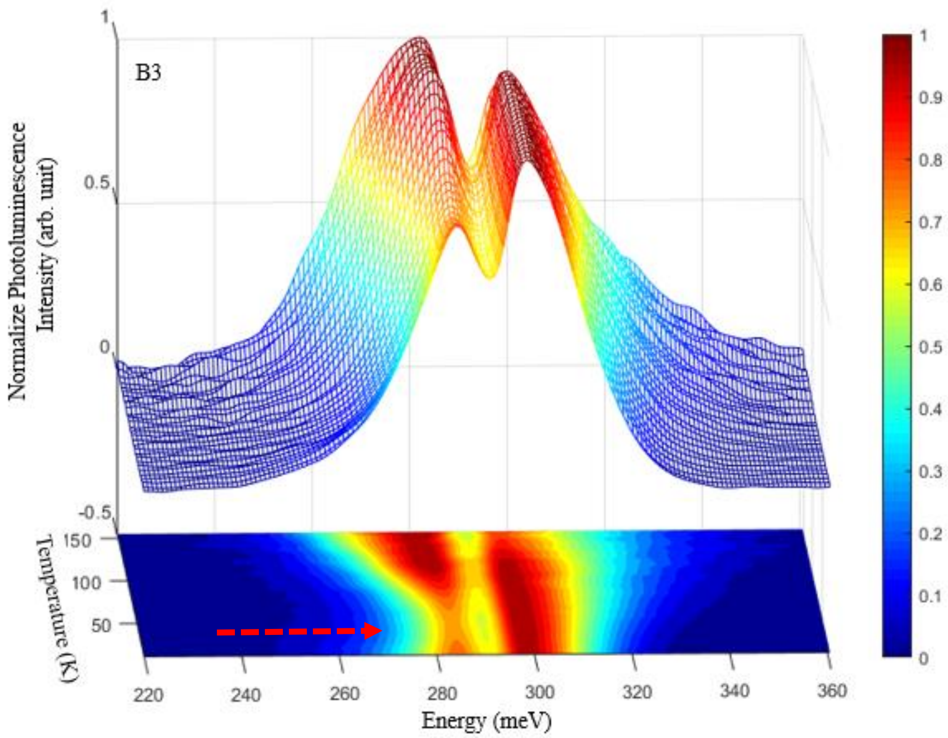

Figure 5.8. *Temperature dependent photoluminescence measurement of B3 nBn detector structures. The red arrow shows the blue-shift in the low energy side of the spectrum.*

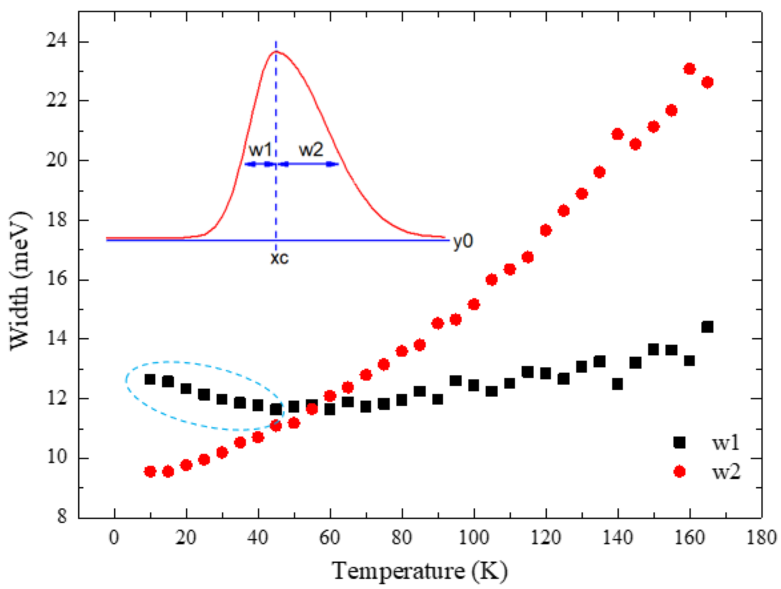

Figure 5.9. *The behavior of the low and high energy side of the photoluminescence peak of the B2 sample according to the increasing temperature.*

On the other hand, laser excitation power dependent measurements were performed to determine the recombination mechanism in the superlattice band gap. Experiments show the recombination at 20 K is due to impurity-related recombination processes. This may indicate why investigated InAs/InAsSb based nBn samples cannot collect the photocurrent efficiently.

In order to investigate the effect of growth-related fluctuations and determine the dominant recombination mechanism, excitation power dependent PL measurements were performed for a previously grown nBn sample (B1). Before the optical measurements, top contact layer of the sample was etched. Then the sample B1 nBn sample was mounted into a closed cycle Helium cooled cryostat with ZnSe window and excited with 632 nm Helium–Neon laser with 1.22 mm beam diameter at a frequency of 5103 Hz. Excitation power intensity was tuned by using a neutral density filter. The PL signal of the barrier and absorber region were recorded by liquid-nitrogen cooled MCT detector under step scan mode.

As shown in Figure 5.10, PL signals were collected for high band gap barrier region and low band gap absorber region at 10 K. The measured peak energy wavelengths of the barrier and absorber are 2.48 µm (~500 meV) and 5 µm (248 meV), respectively. In the design phase, barrier (15/6/18/6/15/15 Å InAs/AlSb/InAs/AlSb/InAs/$InAs_{0.7}Sb_{0.3}$) and absorber (36/15 Å InAs/$InAs_{0.7}Sb_{0.3}$) regions were designed to be 503 and 312 meV at 77 K. As stated earlier, the discrepancy between the calculations and experiments may indicate segregation between the neighbor atoms of the thin individual layers.

Separate PL measurements were carried out for barrier and absorber regions. The result of excitation power dependent PL experiments of the barrier region (absorber region) is shown in Figure 5.11 (Figure 5.12). In Figure 5.11(b) and Figure 5.12(b), integrated PL signal was fitted by using the power law $I = aL^n$, where I is the PL intensity, L is the laser excitation power density, a is the emission efficiency and the n indicates the radiative recombination mechanism. The exponent n ranges from the 1 to 2 for free or bound-exciton recombination and $n < 1$ for the impurity-related recombination processes [67-68].

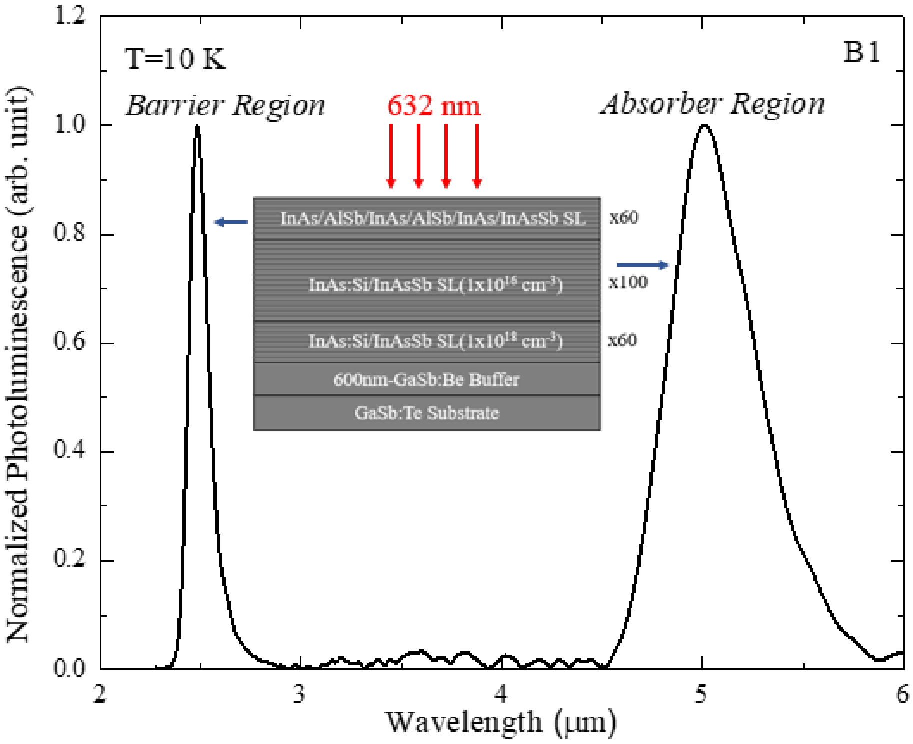

Figure 5.10. *Device structure of the B1 nBn sample and photoluminescence of barrier and absorber region.*

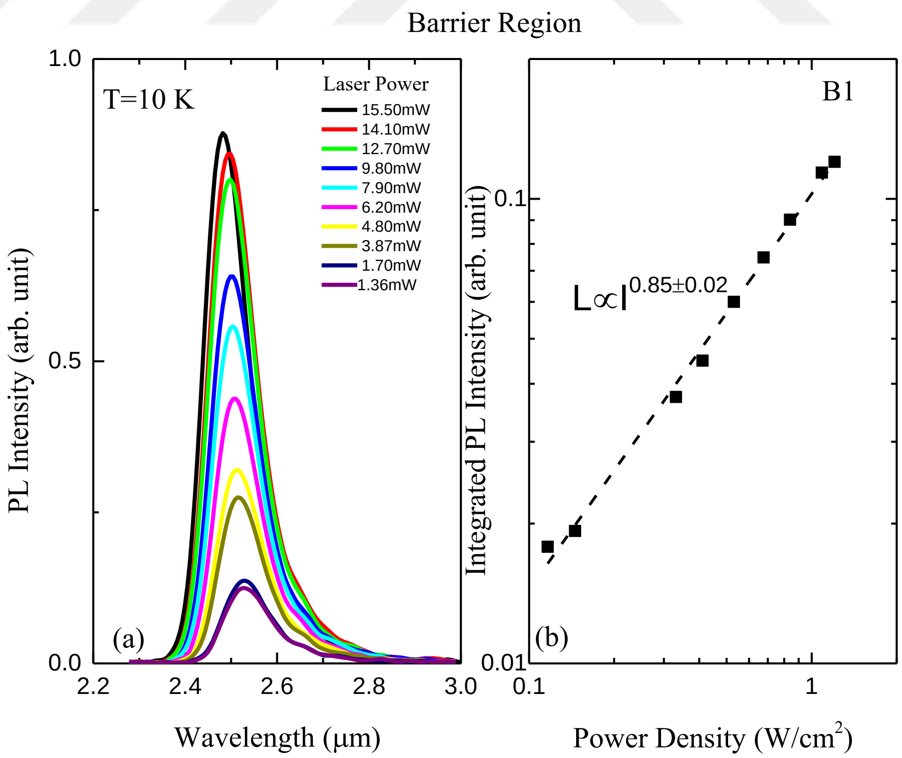

Figure 5.11. *(a) Excitation power dependent PL measurements of the barrier region and (b) integrated PL intensity as a function of laser power density.*

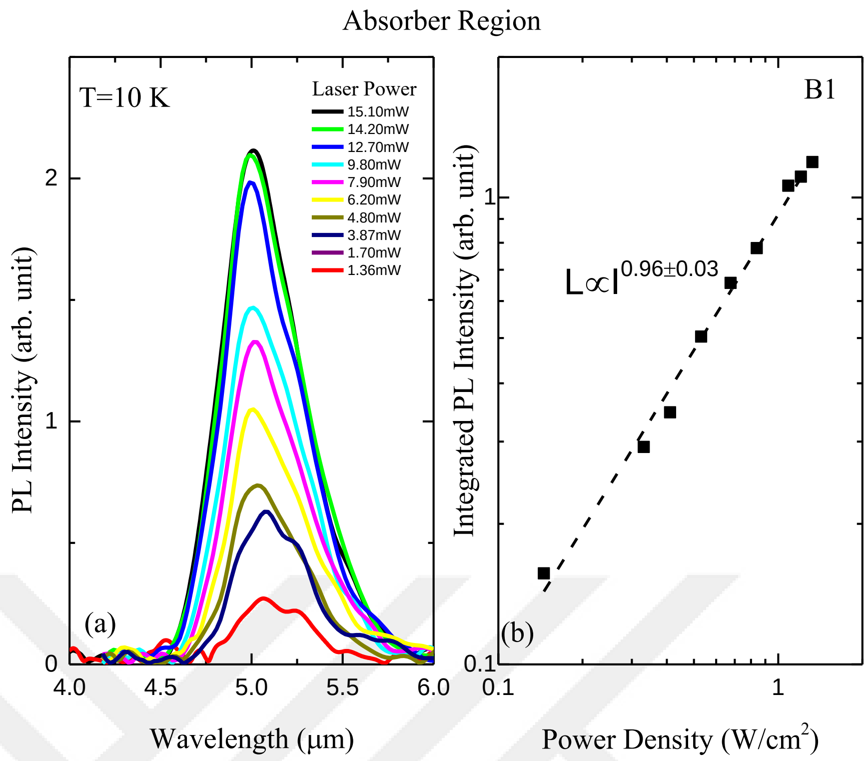

Figure 5.12. *(a) Excitation power dependent PL measurements of the absorber region and (b) integrated PL intensity as a function of laser power density.*

For the measurements at 10 K, the constant n was found as 0.85±0.02 for barrier region and 0.96±0.03 for absorber region. This indicates that the PL emission in both regions of the sample is under the impurity related recombination. The PL signal level of the barrier and absorber region were not high enough to allow temperature dependent measurements. Therefore, temperature dependent recombination characteristics of the sample was not investigated.

6. RADIOMETRIC EVALUATION OF InAs/InAsSb SUPERLATTICE BASED IMAGERS

6.1. Introduction

Performance of the InAs/InAsSb superlattice based nBn MWIR infrared detector has been investigated by radiometric and electronic modeling in a near-realistic infrared imaging system. In this work, the working environment (optical design) and field environment (atmosphere, temperature, range) of the imaging system were modeled. While performing the performance analysis, operating wavelength ($\lambda_{cut\ on}$, $\lambda_{cut\ off}$), quantum efficiency (η), pixel non-uniformity, noise equivalent temperature difference (NETD), integration time (τ_{int}) parameters of the detector were used. The effect of the pixel non-uniformity, NETD and quantum efficiency values on the imaging system were evaluated by analyzing the well fill, dynamics range and bit losses [66-67, http-4].

6.2. Infrared Detector Performance Mode: Well Fill Concept

In semiconductor based infrared imaging systems, the photon detected with focal plane array (FPA) is transformed into a digital signal by readout integrated circuit (ROIC). The ROIC consist of capacitors and create a signal by storing a certain number of electrons within a defined integration time.

The charge capacity of the ROIC of the infrared imaging camera used today is in the order of million electrons (Me). For example, for an imaging system with 14-bit output, it is given as a digital value between 0 and 16383 (2^{14}-1) depending on the value of detected optical signal. When the charge capacity or in other words well fill is completely filled (100%), the digital value taken from the imaging system is 16383. Depending on the incoming photon flux, the well fill is adjusted by changing the integration time and in this way, the ROIC is prevented from reaching saturation.

$$C_{1q\lambda} = 1.88365 \times 10^{27}, \qquad x = \frac{14387.8}{\lambda T}\,[\mu m.K]^{-1}$$

$$L = \int_{\lambda_{cut\,on}}^{\lambda_{cut\,off}} \frac{C_{1q\lambda}}{\pi\lambda^4(e^x - 1)}\,d\lambda \quad \left[\frac{photon}{s.m^2.Sr}\right] \tag{6.1}$$

$$Well\ Fill = 100\,.\frac{\varepsilon_{blackbody}\ A_d\ Fill\ Factor\ \Omega_{detector}\ \tau_{integration}\ T_{optic}\ \eta L}{Well\ Capacity} \tag{6.2}$$

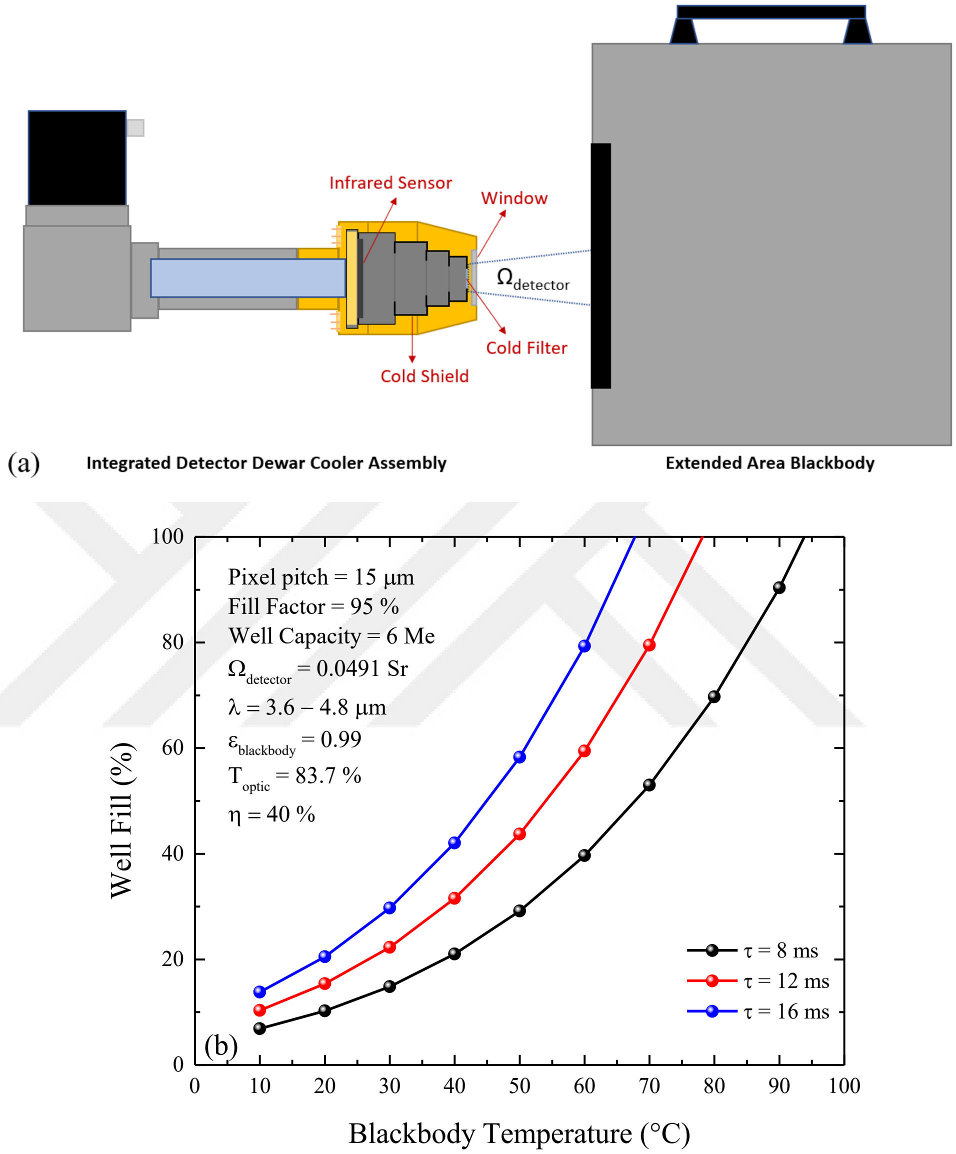

Figure 6.1. *(a) Schematic view of cooled infrared detector in front of the blackbody and (b) well fill percentage of the detector depends on the temperature and integration time.*

The above mentioned well fill concept can be explained with a simple analytical model. As shown in Figure 6.1(a), it can be tough that there is a detector placed in front of a blackbody source with an emissivity (ε) of 0.99. Depending on the temperature, the total incoming photon flux must be calculated for the wavelength range detected by the detector Equation (6.1) [68]. In this way, radiance can be determined by photon flux per unit source surface area, solid angle and second units. Detector parameters such as the pixel area (A_d), fill factor, solid angle ($\Omega_{detector}, Sr$), transmission of optical elements (cold filter and front window) and quantum efficiency determine how much photon can be converted as a photo carrier. Equation (6.2) is used to calculate total well fill of the detector depend on the integration time. Well capacity determines how much electrons can be stored in the ROIC capacitances. Figure 6.1 (b) shows well fill percentage of the detector depend on the blackbody temperature and integration time. Lower integration time increases the detectable temperature range.

By using this simple model, dynamic range of the infrared detector can be calculated for different integration times. However, optical system, atmosphere and figure of merits of the detector should be modeled for the performance evaluation of the real environment imager.

6.3. Infrared Detector Performance Model: Well Fill Calculations

When viewing a scene with infrared imaging system, unwanted heat sources deplete the charge capacity. Undesirable photon flux makes it difficult to distinguish the target on the scene. In order to correctly evaluate the performance of the infrared imaging system, possible signal attenuation effects should be considered in the performance model. For this purpose, effects coming from the optical components (cold shield, hot shield, cold filters, hot optics), scene, atmosphere, path and target were calculated separately and applied to the model [66-67, http-4].

The exitance (M) of a blackbody is expressed by Planck's equation depending on the temperature and wavelength. The amount of photons coming from each heat sources in the model were calculated with Equation (6.3).

$$M(T,\lambda) = \frac{c_{1q\lambda}}{\lambda^4(e^{\mathcal{E}1} - 1)} \left[\frac{q}{s.m^2.\mu m}\right] \tag{6.3}$$

$$c_{1q\lambda} = 1.88365\,x10^{27} \quad , \qquad \mathcal{E}1 = \frac{14387.8}{\lambda}\ [\mu m^{-1}] \tag{6.4}$$

The solid angle of each optical component in the imaging system affects the photon flux reaching the detector. Depending on the position of the optics in the system, the solid angle seen by each optical element was calculated by Equation (6.5).

$$\Omega_{ColdShield} = (\pi - (\pi.(1/(2.f_{\#ColdShield})^2)))$$
$$\Omega_{HotShield} = (\pi - (\pi.(1/(2.f_{\#Optics})^2))) - \Omega_{ColdShield}$$
$$\Omega_{Optics} = (\pi.(1/(2.f_{\#Optics})^2)) - \Omega_{CentralObs} \quad (6.5)$$
$$\Omega_{Filter} = (\pi.(1/(2.f_{\#Optics})^2))$$

Irradiance (E, $q/(s.m^2)$) values of hot optics, cold filter, hot and cold shield components were calculated as follows (Equation (6.6)-(6.9)). Using the solid angle (Ω, Sr), emissivity (ε), transmission (τ), temperature (*T*) values of each optical component, the irradiance values were calculated and used in the model.

$$E_{HotOptics}(T,\lambda) = \Omega_{Optics} \int_{\lambda_1}^{\lambda_2} (1 - \tau_{HotOptics}).\tau_{Filter}.\frac{M(T_{HotOptics},\lambda)}{\pi}.d\lambda \quad (6.6)$$

$$E_{Filter}(T,\lambda) = \Omega_{Filter} \int_{\lambda_1}^{\lambda_2} (1 - \tau_{Filter})\frac{M(T_{Filter},\lambda)}{\pi}.d\lambda \quad (6.7)$$

$$E_{HotShield}(T,\lambda) = \Omega_{HotShield}.\varepsilon_{HotShield} \int_{\lambda_1}^{\lambda_2} \tau_{Filter}.\frac{M(T_{HotShield},\lambda)}{\pi}.d\lambda \quad (6.8)$$

$$E_{ColdShield}(T,\lambda) = \Omega_{ColdShield}.\varepsilon_{ColdShield} \int_{\lambda_1}^{\lambda_2} \tau_{Filter}.\frac{M(T_{Coldhield},\lambda)}{\pi}.d\lambda \quad (6.9)$$

The irradiance value of the ambient, the path, the scene and the target were calculated separately by the following equations (Equation (6.10)-(6.13)). Except for the path, all mechanisms are directly affected by the transmission of the atmosphere (τ_{atmo}). Depending on the weather conditions, the transmission of the atmosphere decreases as the path length increases. As a result, the value of E_{path} irradiance increases as the path length increases, while contributions from the other components (ambient, scene, target (Dynamic)) to the total irradiance decrease. The path irradiance is a dominant mechanism that makes it difficult to distinguish infrared emissions of distant objects from the background radiation [66-67, http-4].

$$E_{Ambient}(T,\lambda) = \Omega_{Optics}.\varepsilon_{Ambient}. \quad (6.10)$$

$$\dots \int_{\lambda_1}^{\lambda_2} \tau_{Filter}.\tau_{Atmo}.\tau_{HotOptics} \frac{M(T_{Ambient},\lambda)}{\pi}.d\lambda$$

$$E_{Path}(T,\lambda) = \Omega_{Optics} \int_{\lambda_1}^{\lambda_2} \tau_{Filter}.(1-\tau_{Atmo}).\tau_{HotOptics} \frac{M(T_{Path},\lambda)}{\pi}.d\lambda \quad (6.11)$$

$$E_{Scene}(T,\lambda) = \Omega_{Optics}.\varepsilon_{Scene} \int_{\lambda_1}^{\lambda_2} \tau_{Filter}.\tau_{Atmo}.\tau_{HotOptics} \frac{M(T_{Scene},\lambda)}{\pi}.d\lambda \quad (6.12)$$

$$E_{Dynamic}(T,\lambda) = \Omega_{Optics}.\varepsilon_{target}.$$
$$\dots \int_{\lambda_1}^{\lambda_2} \tau_{Filter}.\tau_{Atmo}.\tau_{HotOptics} \frac{M(T_{Dynamic},\lambda)}{\pi}.d\lambda \quad (6.13)$$

In order to calculate how much charge each mechanism causes in the well capacity of the ROIC, the detector's quantum efficiency (η), integration time (Int_{time}), pixel area (A_d), well capacity (W_c) should be considered. By multiplying each radiation component by the gain constant (Gain), the well fill rates can be calculated by Equation (6.14). The detectable dynamic range of the target allowed by the system is expressed in terms of the unused dynamic range [66-67, http-4].

$$Gain = \left(100.\eta.\frac{A_d}{W_c}\right).Int_{time}$$
$$Wf_{HotOptics} = Gain\,.E_{HotOptics}$$
$$Wf_{HotShield} = Gain\,.E_{HotShield}$$
$$Wf_{Path} = Gain\,.E_{Path} \quad (6.14)$$
$$Wf_{Scene} = Gain\,.E_{Scene}$$
$$Wf_{Dynamic} = Gain\,.(E_{Dynamic} - E_{Scene})$$
$$Wf_{UnusedDynamicRange} = (Wf_{Dynamic})_{max} - (Wf_{Dynamic})_{min}$$

The total well fill contribution of each component is calculated with the following equation [66-67, http-4].

$$Wf_{Total} = Wf_{HotOptics} + Wf_{HotShield} + Wf_{Path} + Wf_{Scene} + Wf_{Dynamic\dots} + Wf_{UnusedDynamicRange} \quad (6.15)$$

The amount of the well fill that cannot be filled due to photon starvation is calculated by Equation (6.16).

$$Wf_{PhotonStarve} = 100 - Wf_{Total} \quad (6.16)$$

6.4. Infrared Detector Performance Model: Bit Losses

Although the infrared cameras used today give 14 bits output, the dynamic range that can be used decreases due to the losses caused by both focal plane array and electronic components. As a result, it causes performance losses in the imaging system. Pixel non-uniformity at the focal plane array is one of the sources of the bit losses [66].

Inhomogeneous ternary and quaternary compounds, segregation between the individual layers of the superlattice and quantum well structures, crystal defects, irregular sidewall passivation of the mesas could be the source of the non-uniformity in pixel response. For 640×512 format infrared detector, there are 327680 pixels in a focal pane array and it is difficult to achieve a high-level homogeneity in focal plane array with such a large number of pixels. Depending on the amount of the inhomogeneity, a dispersion occurs in the photo-response of the pixels. By applying the non-uniformity correction process [67], it is ensured that the pixels give similar values at the front of the same temperature. Even if the pixel values in the image is equalized, the integration time should be reduced in order to avoid saturation of highly responsive pixels. Therefore, total charge capacity of the ROIC cannot be used effectively and a decrease in the dynamic range occurs. Value of the pixel non-uniformity can be calculated by measuring the signal (voltage, digital value, responsivity etc) distribution of pixels at front of the uniform photon flux (such as extended blackbody).

Depending on the dispersion ratio, non-uniformity related bit lost (nuloss) and usable well capacity ($W_{f\ usable}$) can be calculated with Equation (6.17) and Equation (6.18). For example, if the nuloss is equal to 0.25, the bit loss is 0.42 bit. For the total well capacity is equal to 6 Me, usable well capacity is 4.5 Me [http-4].

$$nubitloss = \log(1 - nuloss)\ /log2 \quad (6.17)$$

$$W_{f\,usable} = W_f(1 - nuloss) \tag{6.18}$$

In case of insufficient amount of photons (photon starvation) at maximum limit of the integration time, charge capacity cannot be filled and in this case bit range cannot used efficiently (Equation (6.19)) [http-4].

$$\begin{aligned} \left|\frac{Wf_{Total}}{100} - 1\right| > 0.005\,, \qquad & Photonstarveloss = \frac{log\left(\frac{Wf_{Total}}{100}\right)}{log2} \\ \left|\frac{Wf_{Total}}{100} - 1\right| \leq 0.005\,, \qquad & 0 \end{aligned} \tag{6.19}$$

Non-target photon sources reduce the dynamic range. Bit loss caused by the hot optics, the scene and the path are calculated by Equation (6.20) and (6.21) [http-4].

$$E_{totalLocalfill} = E_{HotOptics} + E_{Path} + E_{Scene}\ [q/(s.m^2)] \tag{6.20}$$

$$wellfillbitloss = \log\left(1 - \left(\frac{Gain}{100}\right).\eta.\left(E_{totalLocalfill} + E_{Scene}\right)\right)/log2 \tag{6.21}$$

The remaining bit value ($Bits_{NoFill}$) (after the losses brought by non-uniformity, photon starvation, non-target photon sources and bits lost to the small target compared to dynamic range (*BitLostDyn*)) is expressed by the Equation (6.23). ADC_{bits} is the initial dynamic range of the system (14 bit) [http-4].

$$\begin{aligned} BitLostDyn = log\Big((Wf_{Dynamic} \\ - \left(Wf_{Dynamic}\right)_{min})/((Wf_{Dynamic})_{max} \\ - \left(Wf_{Dynamic}\right)_{min})\Big)\,/log2 \end{aligned} \tag{6.22}$$

$$\begin{aligned} Bits_{NoFill} = ADC_{bits} + wellfillbitloss + nubitloss \\ + \ Photonstarveloss + BitLostDyn \end{aligned} \tag{6.23}$$

There are bit losses ($Bits_{NETD}$) due to the detector's NETD value. The NETD value for a detector is a value that can vary depending on the photon flux falling on the detector and it can be calculated for each ambient temperature. The detailed calculation of the $NETD_{Effective}$ value of the system is shown in Appendix [http-4]. Bit loss value caused by NETD is calculated by App.11.

$$\frac{dM(T,\lambda)}{dT} = \frac{c_{1q\lambda} . \xi 2 . e^{\xi 2}}{T . \lambda^4 (e^{\xi 2} - 1)^2} \; \left[\frac{\mathrm{q}}{\mathrm{s.\,m^2.\,\mu m.\,K}}\right]$$

$$\xi 2 = \frac{14387.8}{\lambda . \mathrm{T}} \; [(\mu\mathrm{m.\,K})^{-1}] \quad (6.24)$$

$$\frac{dE_{Ambient}}{dT} = \Omega_{Optics} . \varepsilon_{Ambient} .$$

$$\ldots \int_{\lambda_1}^{\lambda_2} \tau_{Filter} . \tau_{HotOptics} \frac{dM(T_{Ambient}, \lambda)}{\pi . dT} . d\lambda \; \left[\frac{q}{s.\,m^2.\,K}\right] \quad (6.25)$$

$$wellfillNETD = thresholdtoNoise . NETD_{Effective} . \left(\frac{Gain}{100}\right) . \frac{dE_{Ambient}}{dT} \quad (6.26)$$

$$Bits_{NETD} = ADC_{bits} + log(wellfillNETD) \, / log2 \quad (6.27)$$

After the bit losses in the infrared imaging system, the usable dynamic range is $Bits_{Available}$ [http-4].

$$Bits_{Available} = Bits_{Nofill} - Bits_{NETD} \quad (6.28)$$

6.5. Performance Evaluation of InAs/InAsSb Superlattice Imager

In order to evaluate the performance limits of the InAs/InAsSb superlattice imaging system, pixel nonuniformity, NETD value and quantum efficiency of the detector have been changed systematically. The quantum efficiency (~50 %) and NETD value (10-20 mK) of the InAs/InAsSb FPA were reported by the researchers [55, 69]. In the analysis used in this report, three cases where the quantum efficiency ranged from 40 to 80% were examined. The value for the NETD has been changed between the 15 to 35 mK. There is no value reported in the literature for the pixel non-uniformity in the InAs/InAsSb superlattice FPAs. For this reason, analyzes were made with varying values in a wide range (5 to 35%). In the graphs of the analysis, the left axis shows the percent of the well fill and the right axis shows the bit losses and the available dynamic range.

6.5.1. Effect of Pixel Non-Uniformity on System Performance

The pixel non-uniformity could be related to ROIC electronic, homogeneity problems at the crystal or imperfections during fabrication process. First of all, depending on the percentage, usable charge capacity is affected by the non-uniformity (Figure 6.2-Figure 6.5). Figure 6.5 shows the effect of case of 35% non-uniformity values of the pixels. Although the ROIC has 6 Me charge capacity, the system can only use 3.9 Me of it. When the non-uniformity value increases, usable charge capacity decreases and highly responsive pixels approach saturation. Table 6.1 shows the effects of the bit loss mechanisms and available bit value depend on non-uniformity presentence. The system with the lowest non-uniformity value has more available bits and usable well capacity. Although the system with the lowest non-uniformity value has lowest non-uniformity related bit loss, this system experiences the highest photon starvation for the integration time used. Since the system with low non-uniformity does not approach the well capacity limit, photon starvation can be reduced, and the usable dynamic range can be increased by increasing the integration time. On the other hand, non-uniformity level also affects the NETD related bit loss due to its dependence of usable charge capacity.

Table 6.1. *Bit losses and available bit range in systems with different non-uniformity (@ 60 K Target temperature).*

Non-Uniformity (%)	Bits Available	Bits NETD	Bit No Fill	Non-Unifomity Bit Loss	Photon Starvation Bit Loss	Usable Well Capacity (Me)
5	10.6444	2.3716	13.0161	-0.0740	-0.6021	5.7
15	10.4430	2.5321	12.9751	-0.2344	-0.4417	5.1
25	10.2089	2.7126	12.9216	-0.4150	-0.2611	4.5
35	9.9293	2.9191	12.8484	-0.6214	-0.0546	3.9

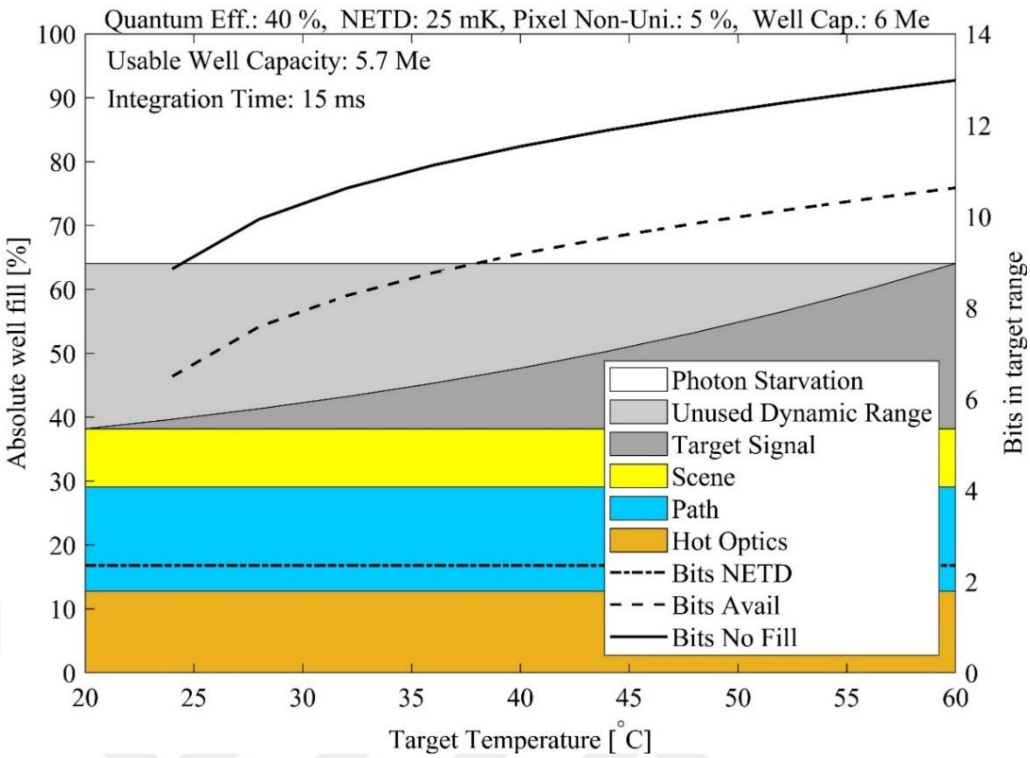

Figure 6.2. *Effect of 5% pixel non-uniformity on well fill and bit values.*

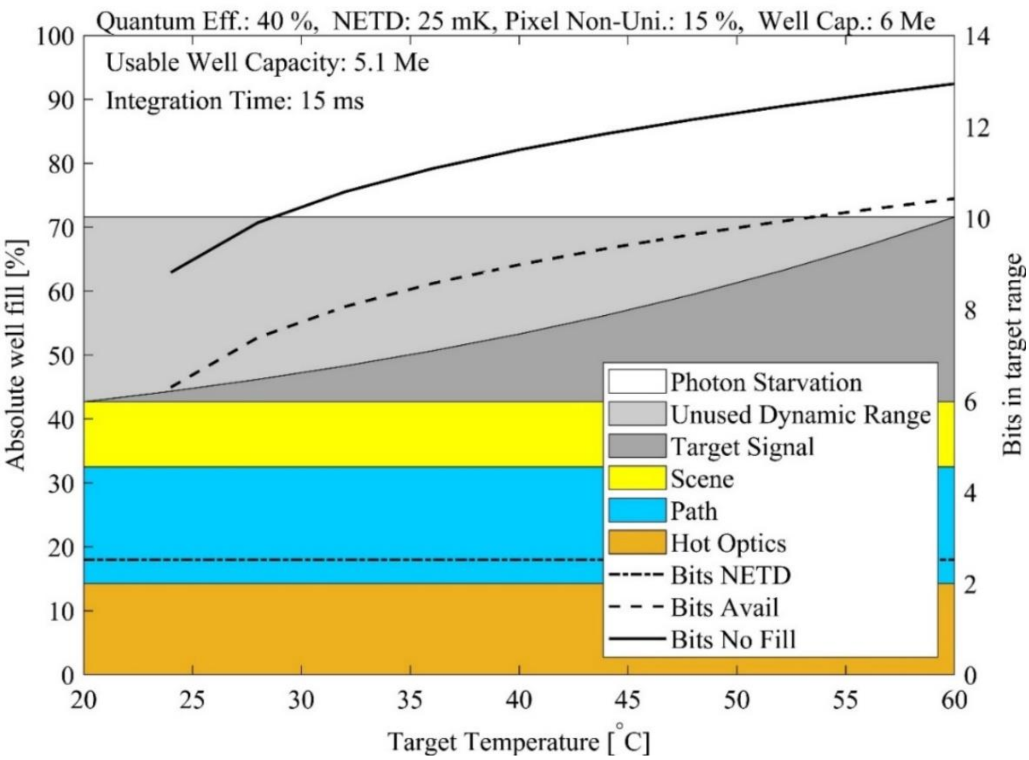

Figure 6.3. *Effect of 15% pixel non-uniformity on well fill and bit values.*

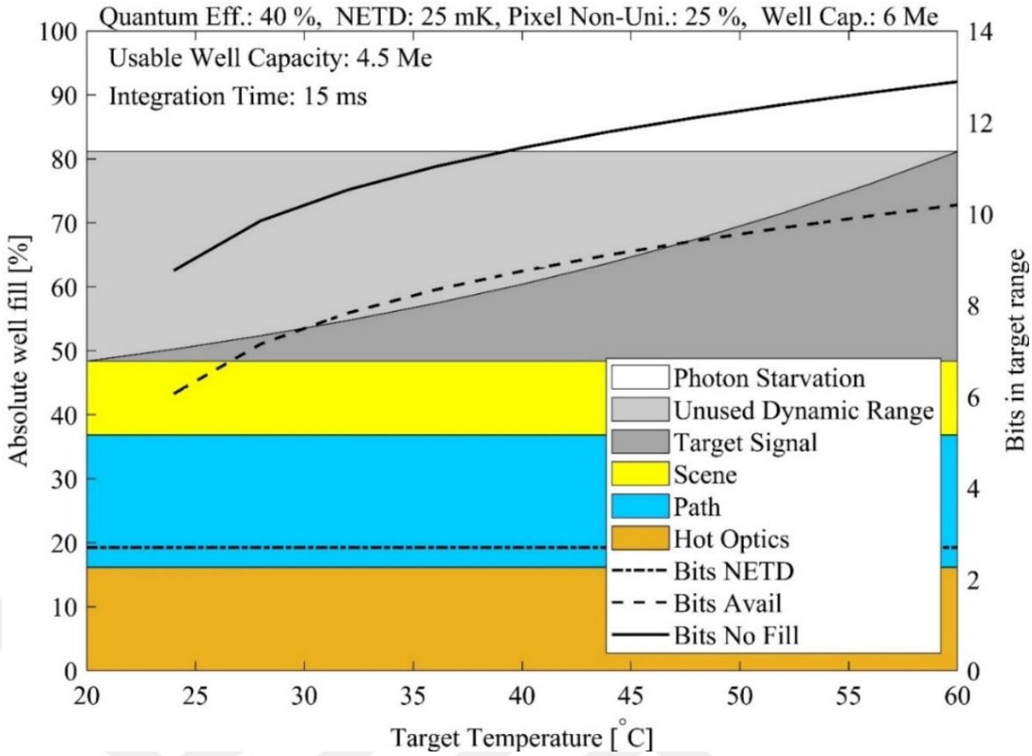

Figure 6.4. *Effect of 25% pixel non-uniformity on well fill and bit values.*

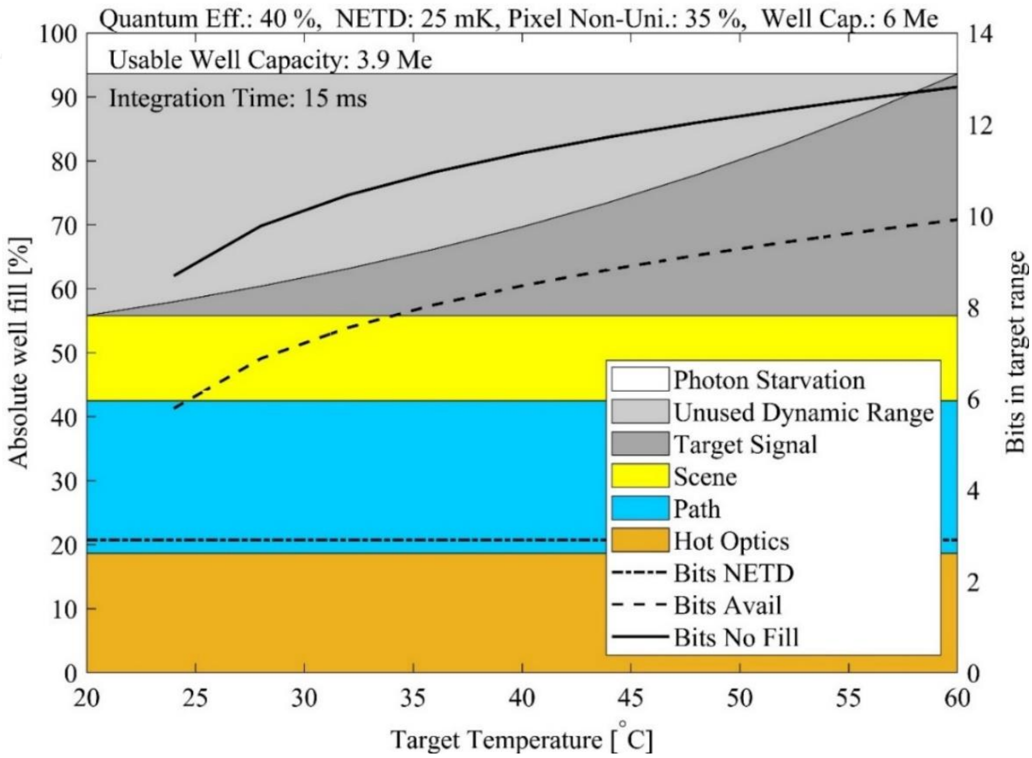

Figure 6.5. *Effect of 35% pixel non-uniformity on well fill and bit values.*

6.5.2. Effect of Quantum Efficiency on System Performance

The detector with high quantum efficiency is indispensable for the systems operating at high speeds. Although similar imaging performance is obtained by increasing the integration time at long ranges, it is difficult to reach high frame rates with low quantum efficiency detectors. In order to compare the low and high quantum efficiency cases, integration time has been changed to ensure the same well fill percent in the analysis. Effects of the quantum efficiency on bit losses and dynamic range are shown in Table 6.2. In the analysis, available dynamic range (Bits Avail) and bit losses (Bits NETD and Well fill bit loss) were found to be close to each other for the three different cases. Detector with low quantum efficiency (40%) has the highest available bit and lowest well fill bit loss. Since the well fill bit loss mechanism sensitive to the changes of the quantum efficiency value (Equation (6.21)), less bit loss occurs in detector with low quantum efficiency. As a result of the analysis (Figure 6.6-Figure 6.8), no significant loss was observed due to the quantum efficiency.

Table 6.2. Effect on quantum efficiency on available bit range and bit losses (@ 60 K Target temperature).

Quantum Efficiency (%)	Bits Available	Bits NETD	Bit No Fill	Well Fill Bit Loss
40	10.4430	2.5321	12.9751	-0.3486
60	10.2310	2.5321	12.7631	-0.5606
80	9.9824	2.5321	12.5145	-0.8093

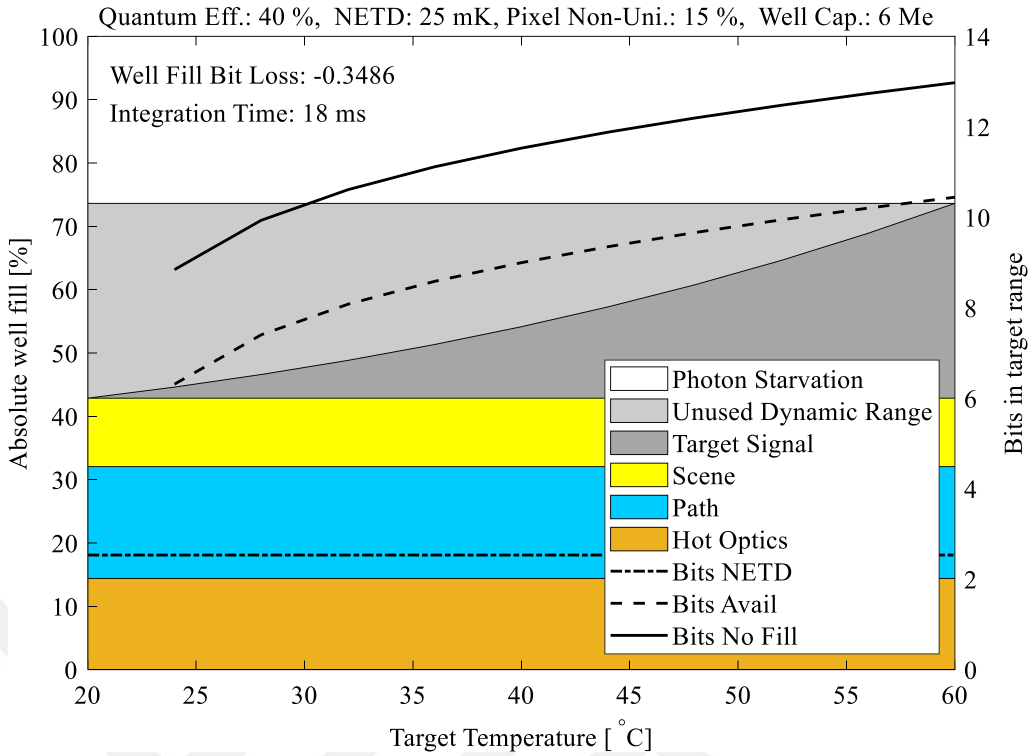

Figure 6.6. *Effect of 40% quantum efficiency value on available bits and well fill bit loss.*

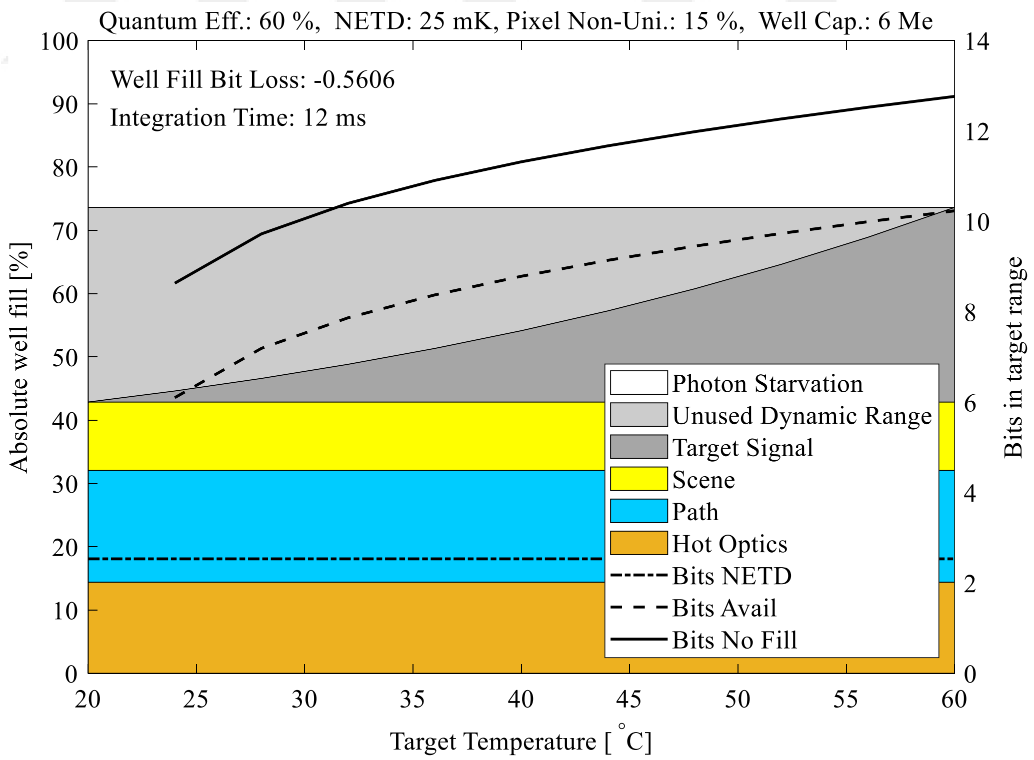

Figure 6.7. *Effect of 60% quantum efficiency value on available bits and well fill bit loss.*

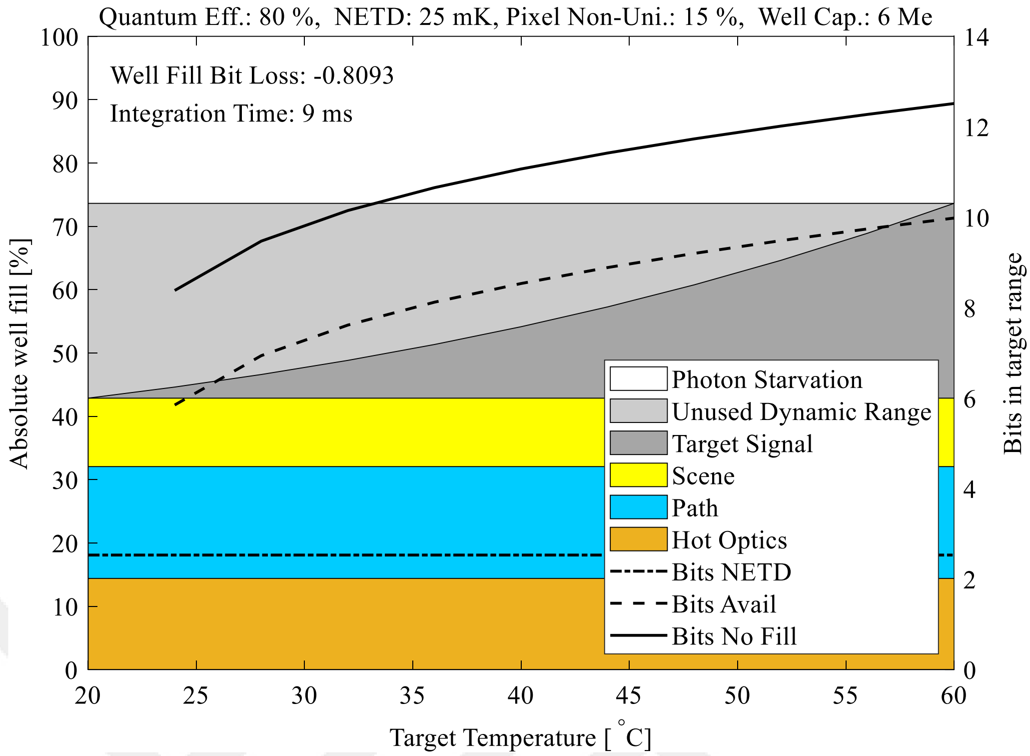

Figure 6.8. *Effect of 80% quantum efficiency value on available bits and well fill bit loss.*

6.5.3. Effect of Noise Equivalent Temperature Difference (NETD) on System Performance

NETD value is one of the most important figure of merits for the focal plane arrays. This value is basically calculated by dividing the standard deviation of the pixels by responsivity of the pixels. However, NETD value may vary, depending on the integration time used and amount of the well fill. The ambient scene (App.8), electronic components (App.9) and the system (App.10) affect the imaging systems NETD value. In this analysis, NETD value of the detector has been changed and effects on effective NETD value and bit losses have been investigated (Figure 6.9-Figure 6.11). Table 6.2 and Figure 6.9, Figure 6.10 and Figure 6.11 show the bit losses and available bit range in imaging system for different NETD values. For the NETD value of 15 and 35 mK, the NETD bit loss ranges approximately between the 2 bits and 3 bits. Increasing of the NETD value of the detector also increase the effective NETD value of the imaging system. As a result, both available dynamic bit range decreases and degrades performance of the noise equivalent temperature difference of the imaging system.

Table 6.3. *Bit losses and available bit range in imaging system for different NETD values (@ 60 K Target temperature).*

$NETD_{std}$ (mK)	**Bits Available**	**Bits NETD**	**Bit No Fill**	**$NETD_{Effective}$ (mK)**
15	11.0573	1.9178	12.9751	21.57
25	10.4430	2.5321	12.9751	33.02
35	9.9954	2.9797	12.9751	45.03

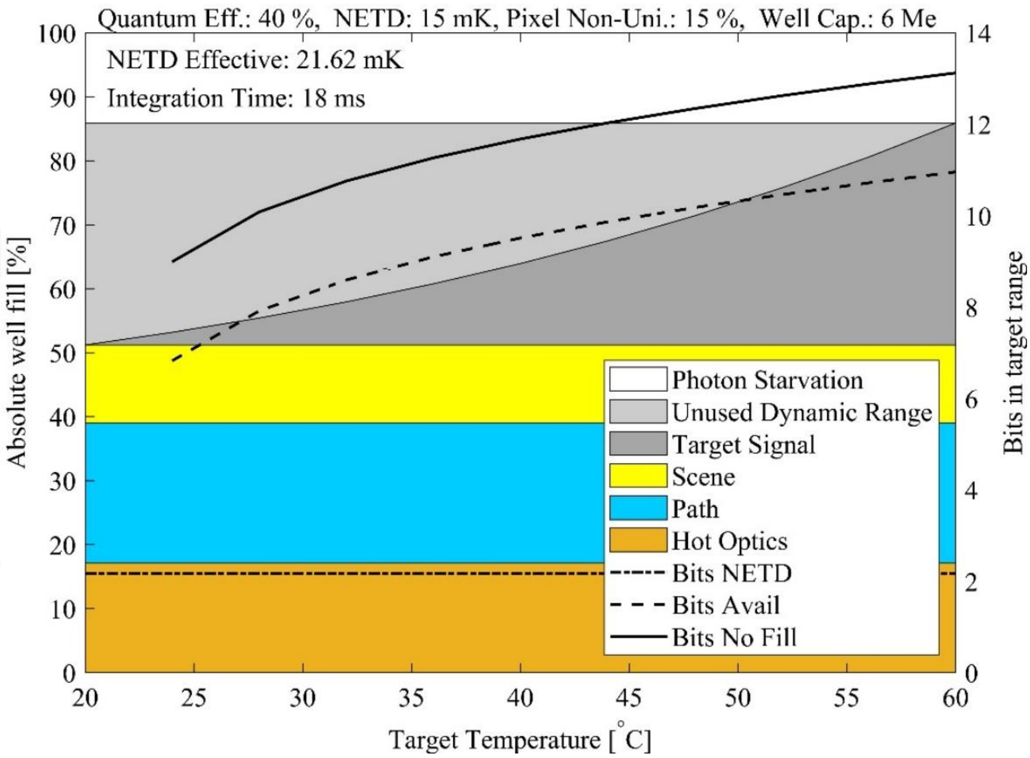

Figure 6.9. *Effect of system NETD value on available bit value and NETD bit loss.*

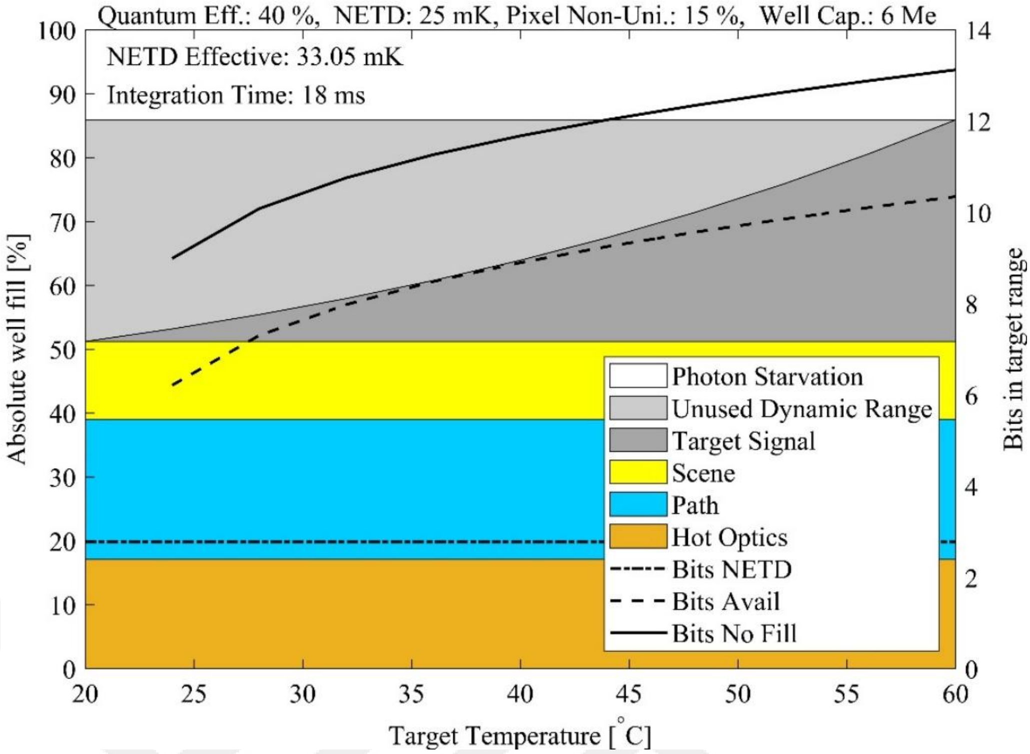

Figure 6.10. *Effect of system NETD value on available bit value and NETD bit loss.*

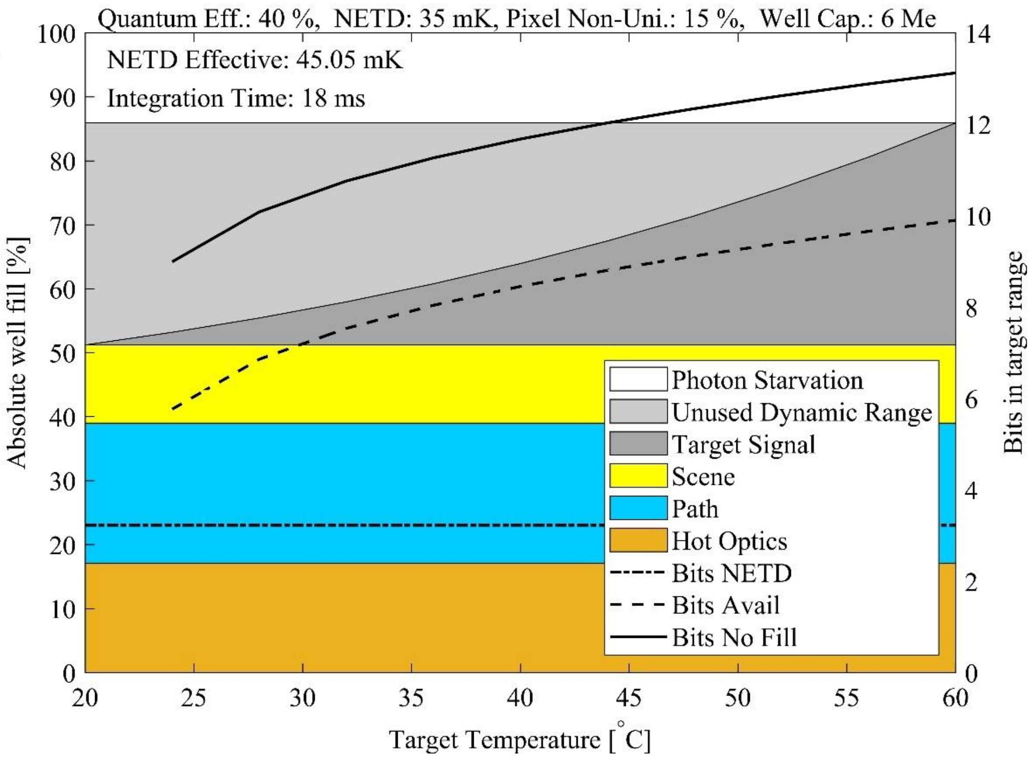

Figure 6.11. *Effect of system NETD value on available bit value and NETD bit loss.*

In this chapter, performance of the InAs/InAsSb superlattice based nBn MWIR infrared detector has been investigated by radiometric and electronic modeling. The effect of the pixel non-uniformity, NETD and quantum efficiency values on the imaging system were evaluated by analyzing the well fill, dynamics range and bit losses. The pixel non-uniformity considerably reduces to usable charge capacity. It also increases bit losses (Bits NETD, non-uniformity bit loss) and decreases the available dynamic bit range. NETD bit losses is a more dominant bit loss mechanism than other bit losses. It consumes approximately 3 bits in total dynamic range. It has been observed that the change in the quantum efficiency does not cause any significant loss in bit loss.

6.6. Infrared Detector Performance Model: Wavelength Dependent Parameters

In the previous radiometric model, the wavelength dependent parameters were atmosphere and cold filter. In the new model, spectral response of the InAs/InAsSb superlattice MWIR detector has been added (Figure 6.12). In this way, the photon detection character of the detector was defined depending on the wavelength. This effect added to the calculation of each radiometric quantity as in Equation (6.29) (Irradiance ($\mathrm{E}, \mathrm{q}/(\mathrm{s.m}^2)$)), solid angle ($\Omega$, Sr), emissivity ($\varepsilon$), transmission ($\tau$), temperature ($T$), detector spectral response ($SR_{detector}$)).

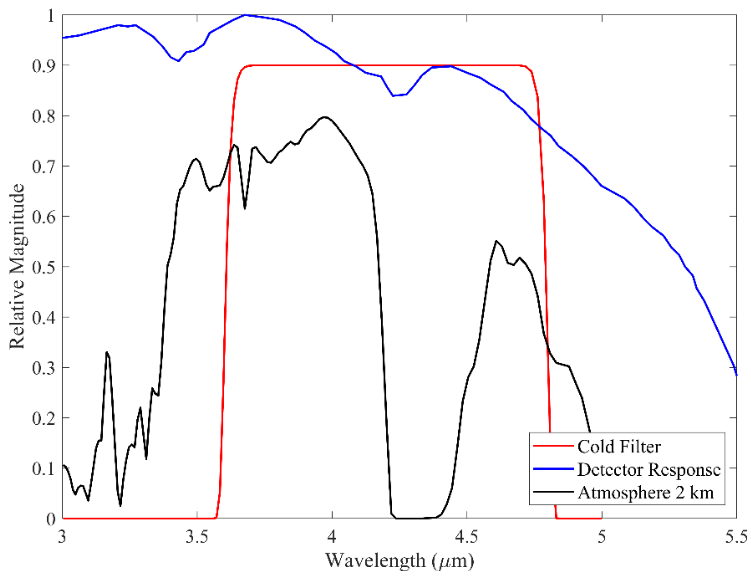

Figure 6.12. *Wavelength dependent parameters used in the radiometric model: atmosphere, detector spectral response and band-pass cold filter.*

$$E(T,\lambda) = \Omega_{Optics}.\varepsilon \int_{\lambda_1}^{\lambda_2} \tau_{Filter}.\tau_{Atmo}.\tau_{Optics}.SR_{detector} \frac{M(T,\lambda)}{\pi}.d\lambda \qquad (6.29)$$

6.7. Infrared Detector Performance Model: Effect of Atmospheric Transmittance and Path Radiance

The atmosphere has highly complex and dynamic character due to changeable density, temperature and pressure depend on the altitude. Also, the chemical composition of the atmosphere varies with the altitude and effects radiation transfer due to molecular absorption. All these factors could cause losses in the transmittance by affecting the propagation of the infrared light in the atmosphere (Figure 6.13). In the model, the corresponding atmospheric transmission was used for each range.

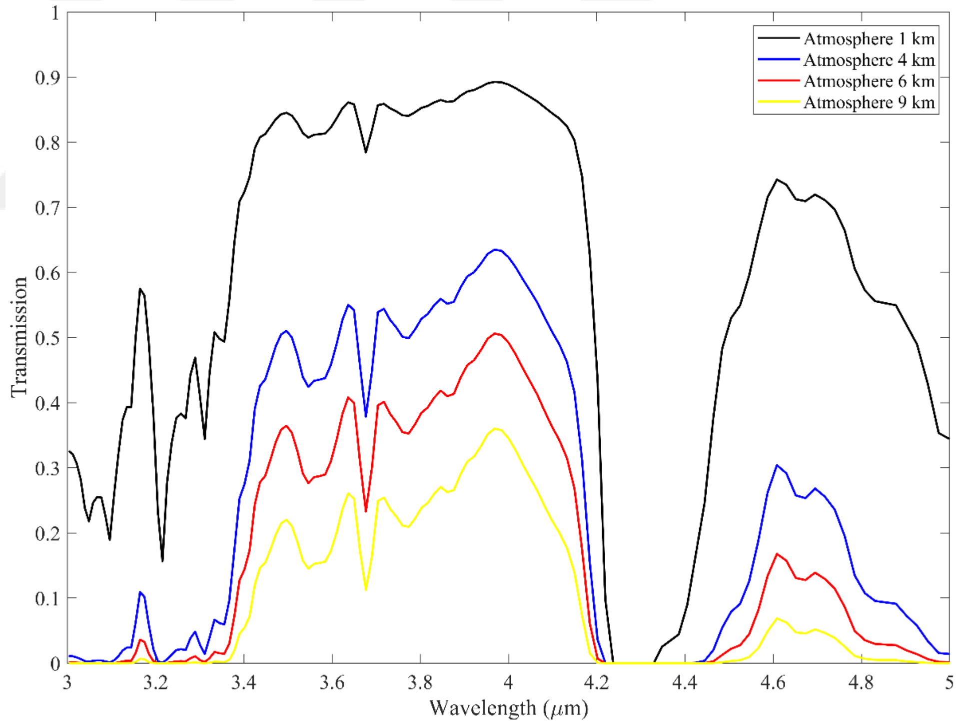

Figure 6.13. *Horizontal path transmission spectrum of the MODTRAN® Tropical 5 km Urban Visibility Tropical Atmosphere for different ranges.*

Depend on the altitude and path distance, atmospheric losses could be high and could consume all emitted radiations from the target. In addition, path radiates to the environment as much as the loss in the transmission. This phenomenon, which is expressed as path radiance, is quite dominant in environments where the transmittance is low and atmosphere temperature is high. The dependence of path irradiance on the transmission of the atmosphere and the temperature of the path is shown in Equation (6.30) [http-4].

$$E_{Path}(T,\lambda) = \Omega_{Optics}.$$

$$\dots \int_{\lambda_1}^{\lambda_2} \tau_{Filter}.(1-\tau_{Atmo}).\tau_{Optics}.SR_{detector} \frac{M(T_{Path},\lambda)}{\pi}.d\lambda \quad (6.30)$$

6.8. Effect of Scene Temperature on System Performance

Radiometric analyses model has been modified to range dependent performance evaluation of superlattice detector-based imaging system. The effect of the scene temperature and cold filter type were studied in detail. Analysis results of the imaging system have been shown depend on the target range (Figure 6.14-Figure 6.17). Table 6.4 shows electro-optical properties of the imaging system used in the analysis.

Table 6.4. *Electro-optical system properties for InAs/InAsSb based MWIR imager.*

Parameters	Value	Unit
Cold shield f number	4	-
Spectral range	3.6 – 4.8	µm
Detector pitch	15	µm
Maximum integration time	30	ms
NETD	30	mK
Well capacity	6	Me
Pixel non-uniformity	25%	-
Peak quantum efficiency	50%	-

The scene term was accepted as the environment in which the target is located. During analysis, difference between the scene temperature and the internal temperature of the imaging system was accepted as 20 °C. It was assumed that the user increased the system integration time up to the allowable value (30 ms) to capture the highest signal during the imaging. MODTRAN® Tropical 5 km Urban Visibility atmospheric model was used for the calculation.

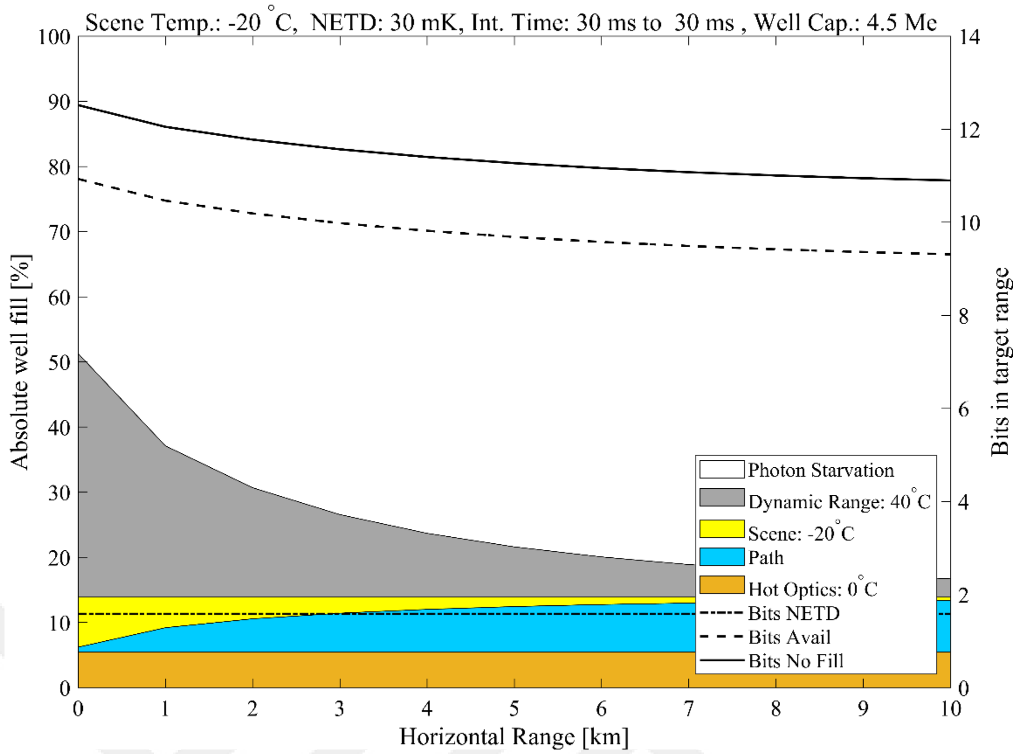

Figure 6.14. *Effect of scene temperature at -20 °C on well fill and bit values for infrared imager with band pass filter.*

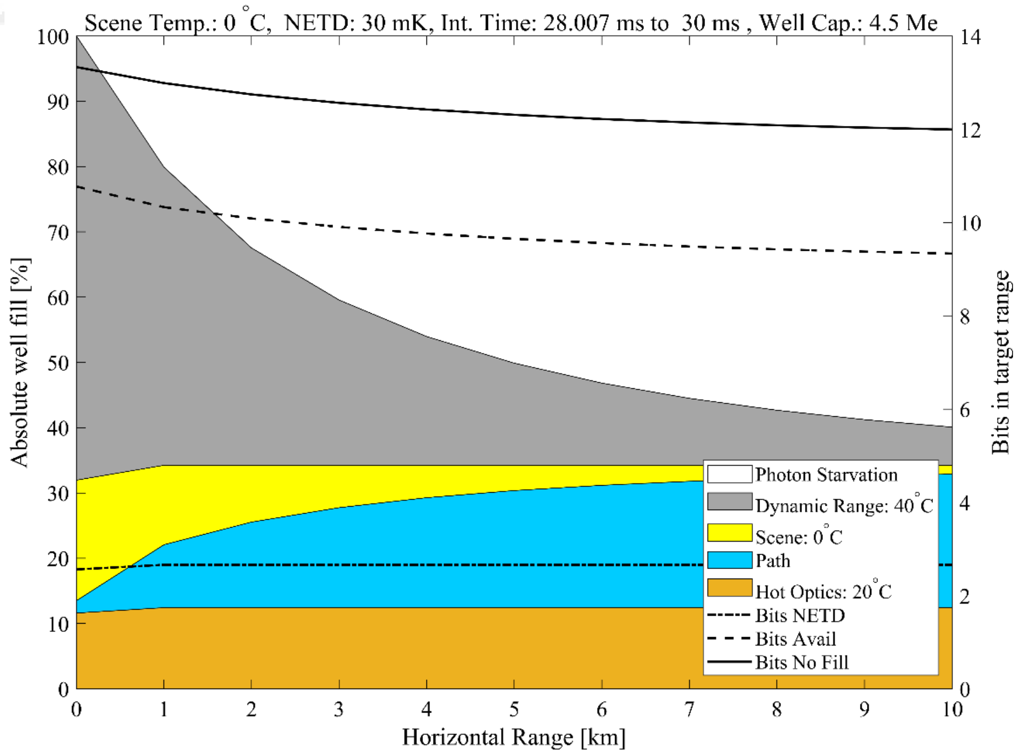

Figure 6.15. *Effect of scene temperature at 0 °C on well fill and bit values for infrared imager with band pass filter.*

Figure 6.14-Figure 6.17 shows the analysis results of the imaging system with band pass filter. In the graphs of the analysis, the left axis shows the percent of the well fill and the right axis shows the bit losses and the available dynamic range. Scene temperatures were changed between the -20 to +40 °C degrees. Radiometric calculations were made up to 10 km range. For the -20 and 0 °C scene temperatures, imaging system is integration time limited and suffers from the photon starvation. Bit losses increase up to 2.5 bit due to photon starvation (Table 6.5). It is clearly seen that most of the well capacity is filled by path radiance with the increase in the scene temperature and horizontal range. As the temperature increases, NETD related bit loss increase. NETD bit loss reached up to 3.68 bit for the 40 °C scene temperature. For -20 and +40 °C scene temperatures, difference between the effective system NETD value is around 4 mK (Table 6.5). Table 6.5 shows the results of the calculated parameters at 1, 4, 7 and 10 km.

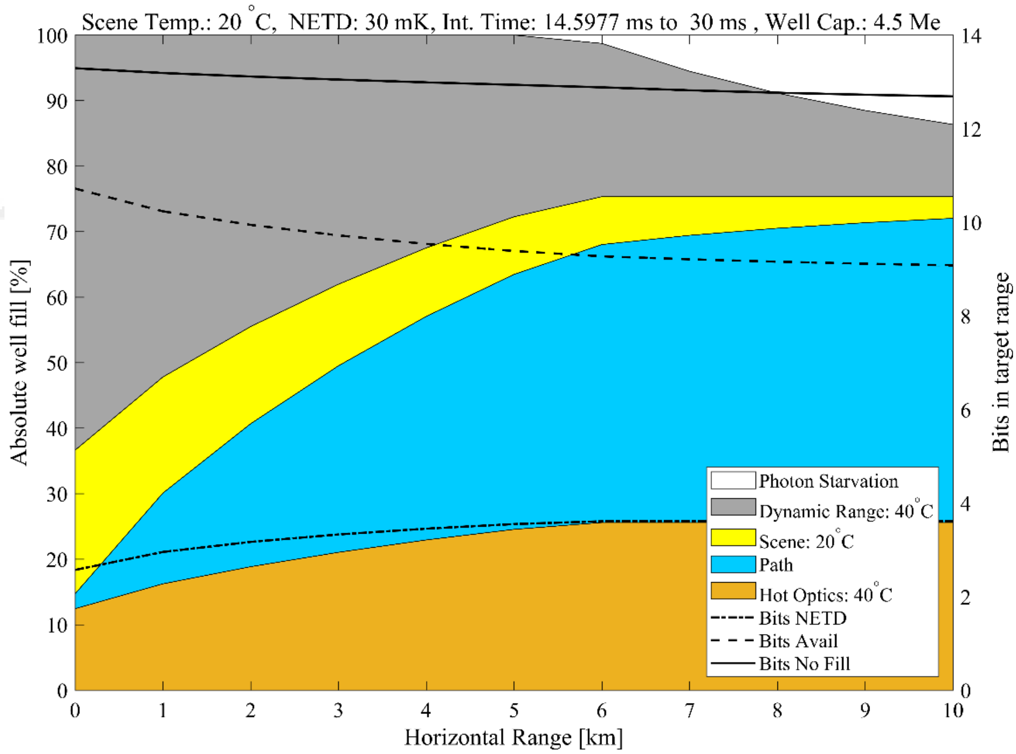

Figure 6.16. *Effect of scene temperature at 20 °C on well fill and bit values for infrared imager with band pass filter.*

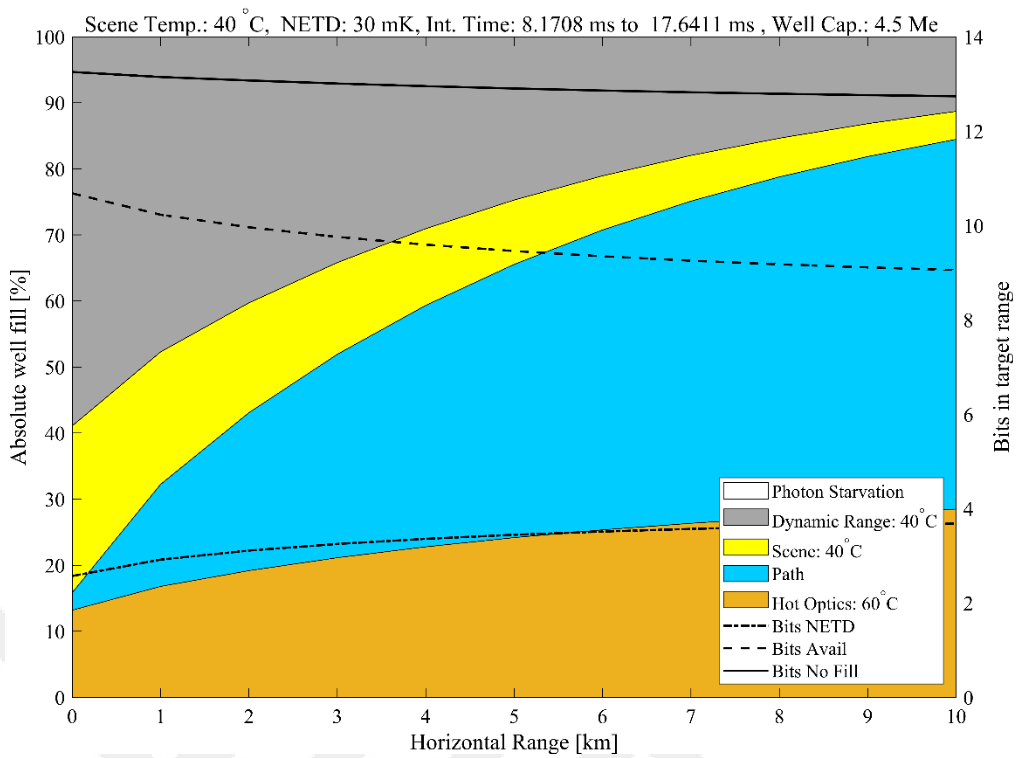

Figure 6.17. *Effect of scene temperature at 40 °C on well fill and bit values for infrared imager with band pass filter.*

Table 6.5. *Dynamic range, well fills and bit losts for InAs/InAsSb superlattice imaging system with band pass filter.*

Scene Temp. (°C)	Horizontal Range				Unit
	1	4	7	10	**km**
	Integration time vs Scene Temperature				
-20	30.0	30.0	30.0	30.0	ms
0	30.0	30.0	30.0	30.0	ms
20	19.03	26.88	30.0	30.0	ms
40	10.39	14.10	16.31	17.64	ms
	Well $Fill_{Path}$ vs Scene Temperature				
-20	3.75	6.57	7.53	7.94	%
0	9.64	16.84	19.34	46.43	%
20	13.85	34.12	43.83	46.43	%
40	15.45	36.55	48.77	55.98	%
	$NETD_{Effective}$ vs Scene Temperature				
-20	42.49	42.49	42.49	42.49	mK
0	40.00	40.00	40.00	40.00	mK
20	38.95	38.95	38.95	38.95	mK
40	38.40	38.40	38.40	38.40	mK
	$Bits_{NETD}$ vs Scene Temperature				
-20	1.58	1.58	1.58	1.58	Bits
0	2.66	2.66	2.66	2.66	Bits
20	2.95	3.45	3.61	3.61	Bits
40	2.91	3.35	3.56	3.68	Bits
	Well $Fill_{Dynamic}$ vs Scene Temperature				
-20	23.23	9.80	5.00	2.81	%
0	45.66	19.71	10.25	5.84	%
20	52.18	32.47	19.12	11.01	%
40	47.71	29.05	17.96	11.28	%
	Bits Available vs Scene Temperature				
-20	10.46	9.81	9.49	9.31	Bits
0	10.33	9.76	9.48	9.33	Bits
20	10.23	9.53	9.20	9.07	Bits
40	10.22	9.59	9.25	9.05	Bits
	Bit $Loss_{Photon\ Starvation}$ vs Scene Temperature				
-20	-1.42	-2.07	-2.40	-2.58	Bits
0	-0.32	-0.88	-1.16	-1.31	Bits
20	0	0	-0.08	-0.21	Bits
40	0	0	0	0	Bits

7. CONCLUSIONS AND FINAL REMARKS

InAs/InAsSb superlattice based barrier infrared detector structure has been designed to meet high temperature operation requirements in MWIR region. Energy band calculations have been performed for the InAs/InAsSb superlattice absorber layer and InAs/AlSb/InAs/AlSb/InAs/InAsSb superlattice barrier layer. The valence band discontinue is about 1 meV and conduction band offset is about 213 meV at 77 K. The expected absorption coefficient for the absorber layer is ~4046 cm^{-1}.

PL signal and spectral response were not observed in p-i-n diodes grown at 0.1 ML/s growth rate. In order to delineate crystal imperfections into the superlattice samples, defect selective etching process was performed. It was observed that all samples had oval defects. In addition, micro-cracks were observed in samples with high lattice mismatch. On the other hand, the samples grown on Wafertech wafers with ~0.4 ML/s growth rate showed spectral response up to 160 K. Responsivity (Quantum efficiency) value of the W3 sample reaches its maximum level at 0.51 A/W (15.8%) (@ 4 µm) at 160 K. It should be noted that the thickness of the absorber layer is approximately 500 nm. We predict that by increasing the absorber layer thickness, the samples will reach the quantum efficiency of superlattice detectors in its class. Temperature dependent dark current measurements show that defect levels exist near the center of the band gap (~98 meV) for W3 sample. Another extracted activation levels (10 and 8meV) for the W2 and W3 sample can be related to surface contribution or tunneling mechanism.

For the nBn InAs/InAsSb samples, although photoluminescence signals were observed in both the barrier and the absorber layer, spectral response could not be obtained in the MWIR region. In InAs/InAsSb superlattice structures, segregation of the Sb atoms is a known phenomenon. If this event cannot be controlled, this may result in unwanted potential barrier as well as the formation of defect centers. In order to investigate the localized states in the absorber superlattices, temperature dependent photoluminescence measurements were performed. For the samples B2 and B3, blue shift was observed at the low-energy side of the luminescence signal at temperature between the 10-45 K. On the other hand, above the 45 K, the tendency to the red-shift was observed. This trend indicates that the superlattice miniband has localized states due to the thickness and alloy composition fluctuations in the superlattices. Excitation power dependent PL measurements analysis indicated that both the absorber and the barrier, B1 sample is under the impurity related recombination. In future work, to improve the performance of the InAs/InAsSb based detectors, it is necessary to grow sets of samples in which the growth temperature, III-V ratio will be changed. Next, the most appropriate device process (etching, passivation) needs to be developed.

In radiometric studies, it can be said that FPA homogeneity is an important parameter that limits system performance, and it can be a critical performance criterion especially for the newly developed material systems such as InAs/InAsSb superlattices. In the scenes where the InAs/InAsSb detectors receive low photons, it is seen that as the distance increases, charge capacity cannot be filled and there is a photon starvation.

REFERENCES

[1] Maimon, S., & Wicks, G. W. (2006)., nBn detector, an infrared detector with reduced dark current and higher operating temperature, Applied Physics Letters, 89(15), 151109.

[2] Rodriguez, J. B., Plis, E., Bishop, G., Sharma, Y. D., Kim, H., Dawson, L. R., & Krishna, S. (2007). nBn structure based on InAs⁄ GaSb type-II strained layer superlattices. Applied Physics Letters, 91(4), 043514.

[3] Klipstein, P. (2008, April). " XBn" barrier photodetectors for high sensitivity and high operating temperature infrared sensors. In Infrared Technology and Applications XXXIV (Vol. 6940, p. 69402U). International Society for Optics and Photonics.

[4] Nguyen, B. M., Bogdanov, S., Pour, S. A., & Razeghi, M. (2009). Minority electron unipolar photodetectors based on type II InAs/GaSb/AlSb superlattices for very long wavelength infrared detection. Applied Physics Letters, 95(18), 183502.

[5] Ting, D. Z. Y., Hill, C. J., Soibel, A., Keo, S. A., Mumolo, J. M., Nguyen, J., & Gunapala, S. D. (2009). A high-performance long wavelength superlattice complementary barrier infrared detector. Applied Physics Letters, 95(2), 023508.

[6] Chen, G., Haddadi, A., Hoang, A. M., Chevallier, R., & Razeghi, M. (2015). Demonstration of type-II superlattice MWIR minority carrier unipolar imager for high operation temperature application. Optics Letters, 40(1), 45-47.

[7] Huang, E. K. W., Hoang, M. A., Chen, G., Ramezani-Darvish, S., Haddadi, A., & Razeghi, M. (2012). Highly selective two-color mid-wave and long-wave infrared detector hybrid based on Type-II superlattices. Optics Letters, 37(22), 4744-4746.

[8] Huang, J., Ma, W., Zhang, Y., Cao, Y., Huang, W., & Zhao, C. (2017). Two-color niBin type II superlattice infrared photodetector with external quantum efficiency larger than 100%. IEEE Electron Device Letters, 38(9), 1266-1269.

[9] Smith, D. L., & Mailhiot, C. (1987). Proposal for strained type II superlattice infrared detectors. Journal of Applied Physics, 62(6), 2545-2548.

[10] Svensson, S. P., Donetsky, D., Wang, D., Hier, H., Crowne, F. J., & Belenky, G. (2011). Growth of type II strained layer superlattice, bulk InAs and GaSb materials for minority lifetime characterization. Journal of Crystal Growth, 334(1), 103-107.

[11] Li, J. V., Chuang, S. L., Jackson, E. M., & Aifer, E. (2004). Minority carrier diffusion length and lifetime for electrons in a type-II InAs⁄ GaSb superlattice photodiode. Applied Physics Letters, 85(11), 1984-1986.

[12] Osbourn, G. C. (1984). InAsSb strained-layer superlattices for long wavelength detector applications. Journal of Vacuum Science & Technology B: Microelectronics Processing and Phenomena, 2(2), 176-178.

[13] Biefeld, R. M., Baucom, K. C., & Kurtz, S. R. (1994). The growth of InAs1-xSbx/InAs strained-layer superlattices by metalorganic chemical vapot deposition. Journal of Crystal Growth, 137(1-2), 231-234.

[14] Schuler-Sandy, T., Myers, S., Klein, B., Gautam, N., Ahirwar, P., Tian, Z. B., ... & Krishna, S. (2012). Gallium free type II InAs/InAsxSb1-x superlattice photodetectors. Applied Physics Letters, 101(7), 071111.

[15] Kim, H. S., Cellek, O. O., Lin, Z. Y., He, Z. Y., Zhao, X. H., Liu, S., ... & Zhang, Y. H. (2012). Long-wave infrared nBn photodetectors based on InAs/InAsSb type-II superlattices. Applied Physics Letters, 101(16), 161114.

[16] Hoang, A. M., Chen, G., Chevallier, R., Haddadi, A., & Razeghi, M. (2014). High performance photodiodes based on InAs/InAsSb type-II superlattices for very long wavelength infrared detection. Applied Physics Letters, 104(25), 251105.

[17] Haddadi, A., Chen, G., Chevallier, R., Hoang, A. M., & Razeghi, M. (2014). InAs/InAs1− xSbx type-II superlattices for high performance long wavelength infrared detection. Applied Physics Letters, 105(12), 121104.

[18] Haddadi, A., Chevallier, R., Chen, G., Hoang, A. M., & Razeghi, M. (2015). Bias-selectable dual-band mid-/long-wavelength infrared photodetectors based on InAs/InAs1− xSbx type-II superlattices. Applied Physics Letters, 106(1), 011104.

[19] Haddadi, A., Suo, X. V., Adhikary, S., Dianat, P., Chevallier, R., Hoang, A. M., & Razeghi, M. (2015). High-performance short-wavelength infrared photodetectors based on type-II InAs/InAs1-xSbx/AlAs1− xSbx superlattices. Applied Physics Letters, 107(14), 141104.

[20] Steenbergen, E. H., Connelly, B. C., Metcalfe, G. D., Shen, H., Wraback, M., Lubyshev, D., ... & Zhang, Y. H. (2011). Significantly improved minority carrier lifetime observed in a long-wavelength infrared III-V type-II superlattice comprised of InAs/InAsSb. Applied Physics Letters, 99(25), 251110.

[21] Olson, B. V., Shaner, E. A., Kim, J. K., Klem, J. F., Hawkins, S. D., Murray, L. M., ... & Boggess, T. F. (2012). Time-resolved optical measurements of minority carrier recombination in a mid-wave infrared InAsSb alloy and InAs/InAsSb superlattice. Applied Physics Letters, 101(9), 092109.

[22] Klipstein, P. C., Livneh, Y., Glozman, A., Grossman, S., Klin, O., Snapi, N., & Weiss, E. (2014). Modeling InAs/GaSb and InAs/InAsSb superlattice infrared detectors. Journal of Electronic Materials, 43(8), 2984-2990.

[23] Ting, D. Z., Soibel, A., & Gunapala, S. D. (2016). Hole effective masses and subband splitting in type-II superlattice infrared detectors. Applied Physics Letters, 108(18), 183504.

[24] Smith, N., Bally, J., Shuping, R. Y., Morris, M., & Kassis, M. (2005). Thermal dust emission from proplyds, unresolved disks, and shocks in the Orion Nebula. The Astronomical Journal, 130(4), 1763.

[25] Carpes, F. P., Mello-Carpes, P. B., Priego Quesada, J. I., Pérez-Soriano, P., Salvador Palmer, R., & Ortiz de Anda, R. M. C. (2018). Insights on the use of thermography in human physiology practical classes. Advances in Physiology Education, 42(3), 521-525.

[26] Dereniak, E. L., & Boreman, G. D. (1996). Infrared detectors and systems (Vol. 24). Wiley-Interscience.

[27] Lohrmann, D., Littleton, R. T., Reese, C. E., Murphy, D., & Vizgaitis, J. N. (2013). Uncooled long-wave infrared small pixel focal plane array and system challenges. Optical Engineering, 52(6), 061305.

[28] Sze, S. M., Ng, K. K. (2007). Physics of semiconductor devices. John Wiley & Sons.

[29] Rogalski, A. (2000). Infrared Detectors. CRC press.

[30] Pankove, J. I. (1975). Optical processes in semiconductors. Courier Corporation.

[31] Chang, L. L., Kawai, N., Sai-Halasz, G. A., Ludeke, R., & Esaki, L. (1979). Observation of semiconductor-semimetal transition in InAs-GaSb superlattices. Applied Physics Letters, 35(12), 939-942.

[32] Esaki, L. (1986). A bird's-eye view on the evolution of semiconductor superlattices and quantum wells. IEEE Journal of Quantum Electronics, 22(9), 1611-1624.

[33] Chang, L. L., & Esaki, L. (1980). Electronic properties of InAs□ GaSb superlattices. Surface Science, 98(1-3), 70-89.

[34] Smith, D. L., & Mailhiot, C. (1987). Proposal for strained type II superlattice infrared detectors. Journal of Applied Physics, 62(6), 2545-2548.

[35] Razeghi, M. (2010). Technology of Quantum Devices, New York, Springer.

[36] Wei, Y., & Razeghi, M. (2004). Modeling of type-II InAs/GaSb superlattices using an empirical tight-binding method and interface engineering. Physical Review B, 69(8), 085316.

[37] Walther, M., Schmitz, J., Rehm, R., Kopta, S., Fuchs, F., Fleißner, J., ... & Ziegler, J. (2005). Growth of InAs/GaSb short-period superlattices for high-resolution mid-wavelength infrared focal plane array detectors. Journal of Crystal Growth, 278(1-4), 156-161.

[38] Mohseni, H., & Razeghi, M. (2001). Long-wavelength type-II photodiodes operating at room temperature. IEEE Photonics Technology Letters, 13(5), 517-519.

[39] Nguyen, B. M., Hoffman, D., Wei, Y., Delaunay, P. Y., Hood, A., & Razeghi, M. (2007). Very high quantum efficiency in type-II In As⁄Ga Sb superlattice photodiode with cutoff of 12 μ m. Applied Physics Letters, 90(23), 231108.

[40] Cabanski, W. A., Eberhardt, K., Rode, W., Wendler, J. C., Ziegler, J., Fleissner, J., ... & Walther, M. (2004, August). Third-generation focal plane array IR detection modules and applications. In Infrared Technology and Applications XXX (Vol. 5406, pp. 184-192). International Society for Optics and Photonics.

[41] Martyniuk, P., Kopytko, M., & Rogalski, A. (2014). Barrier infrared detectors. Opto-Electronics Review, 22(2), 127-146.

[42] Gautam, N., Myers, S., Barve, A. V., Klein, B., Smith, E. P., Rhiger, D., ... & Krishna, S. (2013). Band engineered HOT midwave infrared detectors based on type-II InAs/GaSb strained layer superlattices. Infrared Physics & Technology, 59, 72-77.

[43] Martyniuk, P., Kopytko, M., & Rogalski, A. (2014). Barrier infrared detectors. Opto-Electronics Review, 22(2), 127-146.

[44] Delaunay, P. Y., Nosho, B. Z., Gurga, A. R., Terterian, S., & Rajavel, R. D. (2017, May). Advances in III-V based dual-band MWIR/LWIR FPAs at HRL. In Infrared Technology and Applications XLIII (Vol. 10177, p. 101770T). International Society for Optics and Photonics.

[45] Jenkins, J., Terterian, S., Tu, B., Strong, W., Roebuck, M., De Lyon, T. J., ... & Curzan, J. P. (2017, May). Fabrication of small pitch, high definition (HD) 1kx2k/5um MWIR focal-plane-arrays operating at high temperature (HOT). In Infrared Technology and Applications XLIII (Vol. 10177, pp. 350-356). SPIE.

[46] Rhiger, D. R. (2011). Performance comparison of long-wavelength infrared type II superlattice devices with HgCdTe. Journal of Electronic Materials, 40(8), 1815-1822.

[47] Aytac, Y., Olson, B. V., Kim, J. K., Shaner, E. A., Hawkins, S. D., Klem, J. F., ... & Boggess, T. F. (2014). Effects of layer thickness and alloy composition on carrier lifetimes in mid-wave infrared InAs/InAsSb superlattices. Applied Physics Letters, 105(2), 022107.

[48] Steenbergen, E. H., Connelly, B. C., Metcalfe, G. D., Shen, H., Wraback, M., Lubyshev, D., ... & Zhang, Y. H. (2011). Significantly improved minority carrier lifetime observed in a long-wavelength infrared III-V type-II superlattice comprised of InAs/InAsSb. Applied Physics Letters, 99(25), 251110.

[49] Ting, D. Z., Soibel, A., Khoshakhlagh, A., Rafol, S. B., Keo, S. A., Höglund, L., ... & Gunapala, S. D. (2018). Mid-wavelength high operating temperature barrier infrared detector and focal plane array. Applied Physics Letters, 113(2), 021101.

[50] Wu, D., Li, J., Dehzangi, A., & Razeghi, M. (2020). Mid-wavelength infrared high operating temperature pBn photodetectors based on type-II InAs/InAsSb superlattice. AIP Advances, 10(2), 025018.

[51] Soibel, A., Ting, D. Z., Rafol, S. B., Fisher, A. M., Keo, S. A., Khoshakhlagh, A., & Gunapala, S. D. (2019). Mid-wavelength infrared InAsSb/InAs nBn detectors and FPAs with very low dark current density. Applied Physics Letters, 114(16), 161103.

[52] Kim, Y. H., Lee, H. J., Kim, Y. C., Eom, J. H., Son, J. O., Jung, H. C., ... & Jung, H. (2021, April). HOT InAs/InAsSb nBn detector development for SWaP detector. In Infrared Technology and Applications XLVII (Vol. 11741, p. 117410Y). International Society for Optics and Photonics.

[53] Durlin, Q., Perez, J. P., Rossignol, R., Rodriguez, J. B., Cerutti, L., Delacourt, B., ... & Christol, P. (2017, January). InAs/InAsSb superlattice structure tailored for detection of the full midwave infrared spectral domain. In Quantum Sensing and Nano Electronics and Photonics Xiv (Vol. 10111, pp. 149-158). SPIE.

[54] Webster, P. T., Riordan, N. A., Liu, S., Steenbergen, E. H., Synowicki, R. A., Zhang, Y. H., & Johnson, S. R. (2015). Absorption properties of type-II InAs/InAsSb superlattices measured by spectroscopic ellipsometry. Applied Physics Letters, 106(6), 061907.

[55] Ting, D. Z., Rafol, B., Keo, S. A., Nguyen, J., Khoshakhlagh, A., Soibel, A., ... & Gunapala, S. D. (2018). InAs/InAsSb type-II superlattice mid-wavelength infrared focal plane array with significantly higher operating temperature than InSb. IEEE Photonics Journal, 10(6), 1-6.

[56] Kim, H. S., Cellek, O. O., Lin, Z. Y., He, Z. Y., Zhao, X. H., Liu, S., ... & Zhang, Y. H. (2012). Long-wave infrared nBn photodetectors based on InAs/InAsSb type-II superlattices. Applied Physics Letters, 101(16), 161114.

[57] Haddadi, A., Dehzangi, A., Adhikary, S., Chevallier, R., & Razeghi, M. (2017). Background–limited long wavelength infrared InAs/InAs1− xSbx type-II superlattice-based photodetectors operating at 110 K. APL Materials, 5(3), 035502.

[58] Sidor, D. E., Savich, G. R., & Wicks, G. W. (2016). Surface leakage mechanisms in III–V infrared barrier detectors. Journal of Electronic Materials, 45(9), 4663-4667.

[59] Schuler-Sandy, T., Klein, B., Casias, L., Mathews, S., Kadlec, C., Tian, Z., ... & Krishna, S. (2015). Growth of InAs–InAsSb SLS through the use of digital alloys. Journal of Crystal Growth, 425, 29-32.

[60] Hao, R., Ren, Y., Liu, S., Guo, J., Wang, G., Xu, Y., & Niu, Z. (2017). Fabrication and characterization of high lattice matched InAs/InAsSb superlattice infrared photodetector. Journal of Crystal Growth, 470, 33-36.

[61] Schuler-Sandy, T., Myers, S., Klein, B., Gautam, N., Ahirwar, P., Tian, Z. B., ... & Krishna, S. (2012). Gallium free type II InAs/InAsxSb1-x superlattice photodetectors. Applied Physics Letters, 101(7), 071111.

[62] Nicolaï, J., Warot-Fonrose, B., Gatel, C., Teissier, R., Baranov, A. N., Magen, C., & Ponchet, A. (2015). Formation of strained interfaces in AlSb/InAs multilayers grown by molecular beam epitaxy for quantum cascade lasers. Journal of Applied Physics, 118(3), 035305.

[63] Lin, Z. Y., Liu, S., Steenbergen, E. H., & Zhang, Y. H. (2015). Influence of carrier localization on minority carrier lifetime in InAs/InAsSb type-II superlattices. Applied Physics Letters, 107(20), 201107.

[64] Steenbergen, E. H., Massengale, J. A., Ariyawansa, G., & Zhang, Y. H. (2016). Evidence of carrier localization in photoluminescence spectroscopy studies of mid-wavelength infrared InAs/$InAs_{1-x}Sb_x$ type-II superlattices. Journal of Luminescence, 178, 451-456.

[65] Schmidt, T. L. K. Z., Lischka, K., & Zulehner, W. (1992). Excitation-power dependence of the near-band-edge photoluminescence of semiconductors. Physical Review B, 45(16), 8989.

[66] Willers, C. J., & Goss, T. M. (2017, February). MWIR sensor well fill: sources, effects and mitigation. In Fourth Conference on Sensors, MEMS, and Electro-Optic Systems (Vol. 10036, pp. 378-393). SPIE.

[67] Willers, C. J., Electro-Optical System Analysis and Design: A Radiometry Perspective, Vol. PM236, SPIE Press, Bellingham, WA (2013)

[68] A Study on Calibration Methods for Infrared Focal Plane Array Cameras, 2018 15th IEEE International Conference on Advanced Video and Signal Based Surveillance (AVSS).

[69] Ariyawansa, G., Duran, J., Reyner, C., & Scheihing, J. (2019). InAs/InAsSb strained-layer superlattice mid-wavelength infrared detector for high-temperature operation. Micromachines, 10(12), 806.

http-1: Zhang, Y.-H., (2017) Ga-Free InAs/InAsSb type-II superlattice: its past, present, and future, https://www.youtube.com/watch?v=yFSSCWuUkvw, (Access Date:15.06.2022).

http-2: https://www.youtube.com/watch?v=AzyH0M4C8TY, (Access Date: 15.06.2022)

http-3:https://www.gst-ir.net/products/uncooled-infrared-detectors/1280X1024 /gst1212m.html, (Access Date: 15.06.2022).

http-4: Computational Optical Radiometry Notebook 12h MWIR well fill https://github.com/NelisW/ComputationalRadiometry, (Access Date: 15.06.2022).

APPENDIX

The following equations were used to calculate different NETD components [66, http-4].

$$NETD_{BLIP\ std} = 2\sqrt{2}.h.c.f_{\#ColdShield}.\sqrt{\frac{100}{W_{f\ usable}.W_c}}.\frac{Eq_{Std\ back}}{M_{deriv\ stdm}} \quad \text{(App.1)}$$

$$Eq_{Std\ back} = \int_{\lambda_1}^{\lambda_2} \tau_{Filter}.(\pi - \Omega_{ColdShield})\frac{M(T_{NETD_{std}}, \lambda)}{\pi}.d\lambda \quad \text{(App.2)}$$

$$M_{deriv\ stdm} = \int_{\lambda_1}^{\lambda_2} \tau_{Filter}.\frac{dM(T_{NETD_{std}}, \lambda)}{\pi.dT}.d\lambda \quad \text{(App.3)}$$

$$ratio_{M_{deriv}} = \frac{M_{deriv\ stdm}}{M_{deriv\ fldm}}.(1 - CentralObs) \quad \text{(App.4)}$$

$$M_{deriv\ fldm} = \int_{\lambda_1}^{\lambda_2} \tau_{Filter}.\frac{dM(T_{Ambient}, \lambda)}{\pi.dT}.d\lambda \quad \text{(App.5)}$$

$$NETD_{degrade\ factor} = \frac{Eq_{Std\ back}}{M_{deriv\ stdm}}.{ratio_{M_{deriv}}}^2 \quad \text{(App.6)}$$

$$P2_{fracApp} = 1 - CentralObs \quad \text{(App.7)}$$

$$NETD_{BLIP\ Scene} = \sqrt{NETD_{degrade\ factor}.\frac{NETD_{BLIP\ std}}{P2_{fracApp}}} \quad \text{(App.8)}$$

$$NETD_{Elec} = \sqrt{{NETD_{std}}^2 - {NETD_{BLIP\ std}}^2} \quad \text{(App.9)}$$

$$NETD_{Sys} = k_{sys}.NETD_{sys} \quad \text{(App.10)}$$

$$NETD = \sqrt{{NETD_{BLIP\ Scene}}^2 + {NETD_{Elec}}^2 + {NETD_{Sys}}^2} \quad \text{(App.11)}$$

CURRICULUM VITAE

ORCID ID: 0000-0002-9051-4464

Name-Surname: Melih KORKMAZ

Foreign Language: English

Education:

2014-2022	**Ph.D.**
	Eskişehir Technical University, Turkey
	Department of Physics
2011-2014	**M.Sc.**
	Anadolu University, Turkey
	Department of Physics
2005-2010	**B.Sc.**
	Ankara University, Turkey
	Department of Physics Engineering

Profession:

10.2021-	ASELSAN-Micro Electronic Design Directorate
	System Engineer
02.2019-10.2021	TÜBİTAK
	Defence Industries Research and Development Institute
	Optical Systems Division
	Research Engineer
08.2011-02.2019	Eskişehir Technical University
	Nanoboyut Research Laboratory
	Researcher

Publications:

1. **Melih Korkmaz**, Melih Kaldirim, Bulent Arikan, Uğur Serincan, Bulent Aslan, *"Comparative evaluation of InAs/GaSb superlattices for mid infrared detection: p-i-n versus residual doping"* Semicond. Sci. Technol. 30 (2015) 085006.
2. Bulent Arikan, **Melih Korkmaz**, Bulent Aslan, Uğur Serincan *"Structural and optical characterization of InAs/GaSb type-II superlattices: Influence of the change in InAs and GaSb layer thicknesses for fixed InSb-like interfaces"* Thin Solid Films 589 (2015)813-816.
3. Bulent Aslan, **Melih Korkmaz**, "*Influence of the lattice mismatch on the lattice vibration modes for InAs/GaSb superlattices*" Appl. Surf. Sci. 362 (2016) 244.
4. **M. Korkmaz**, B. Arikan, Y. E. Suyolcu, B. Aslan, U. Serincan, "*Performance evaluation of InAs/GaSb superlattice photodetector grown on GaAs substrate using AlSb interfacial misfit array*" Semicond. Sci. Technol. 33 (2018) 035002.